UNIVERSITY OF CALIFORNIA,
IRVINE

Endoscopic Optical Coherence Tomography: New Applications and Quantification Techniques

DISSERTATION

submitted in partial satisfaction of the requirements
for the degree of

DOCTOR OF PHILOSOPHY

in Biomedical Engineering

by

Yusi Miao

Dissertation Committee:
Professor Zhongping Chen, Chair
Professor Matthew Brenner
Professor Bernard Choi

2020

DEDICATION

To

Mom, Dad, and Hoai

TABLE OF CONTENTS

LIST OF FIGURES

Page

LIST OF TABLES

Page

TABLE OF ABBREVIATIONS

3D	Three-dimensional
AOM	Acousto Optic Modulator
ARDS	Acute Respiratory Distress Syndrome
AV	Airway Volume
BL	Baseline
BPD	Balanced Photodetector
BW	Bandwidth
CBF	Ciliary Beating Frequency
CCD	Charged Coupled Device
CF	Cystic Fibrosis
CFD	Computational Fluid Dynamic
CMOS	Complementary Metal–oxide–semiconductor
CNN	Convolutional Neural Network
COPD	Chronic Obstructive Pulmonary Disease
CT	Computed Tomography
DP	Dynamic Programming
DSC	Dice Similarity Coefficient
FCN	Fully Convolutional Network
FD	Fourier Domain
GS-FID	Gas Chromatography-flame Ionization Detection
FOV	Filed-of-view
FTIR	Fourier Transform Infrared Spectroscopy
FWHM	Full Width Half Maximum
GRIN	Gradient Index
GSM	Genitourinary Syndrome of Menopause
IBDV	Intensity-based Doppler Variance
LCI	Low Coherence Interferometer
MEMS	Micro-Electro-Mechanical Systems
MIC	Methyl Isocyanate
MRI	Magnetic Resonance Imaging
MT	Mucus Thickness
MZI	Mach-Zehnder Interferometer

NA	Numerical Aperture
NURD	Nonuniform Distortion
OCDR	Optical Coherence Domain Reflectometer
OCE	Optical Coherence Elastography
OCT	Optical Coherence Tomography
OCTA	Optical Coherence Tomography Angiography
OPD	Optical Path Difference
PAV	Proximal Airway Volume
PC	Polarization Controller
PCD	Primary Cilia Dyskinesia
PFR	PaO2-to-FiO2 Ratio
PI	Post-injury
PIP	Peak Inspiratory Pressure
PM	Polarization Maintaining
PRD	Phase-resolved Doppler
PRDV	Phase-resolved Doppler Variance
PS	Polarization Sensitive
PSF,	Point Spread Function
PZT	Piezo-electric Transducer
QWP	Quarter Wave Plate
ROI	Region of Interest
SD	Spectral Domain
SEIM	Spectral-encoded Interferometric Microscopy
SII	Smoke Inhalation Injury
SNR	Signal-to-noise Ratio
SS	Swept-source
STFFT	Short-time Fourier Transformation
TD	Time-domain
VCSEL	Vertical-cavity Surface-emitting Laser
VET	Vaginal Epithelium Thickness

ACKNOWLEDGMENTS

I would like to express the deepest appreciation to my advisor, Professor Zhongping Chen. Dr. Chen offered me the opportunity and resources to continue my graduate work in the Ph.D. program. Dr. Chen has also guided my career path by sharing his knowledge and experience of working in academia when I was lost. Without his guidance and persistent help, I would not be the same person as I am today.

I would like to thank my committee members, Professor Matthew Brenner and Professor Bernard Choi for their insight and guidance throughout my graduate work. In particular, Dr. Brenner was always willing to take the time out of his busy schedule to provided constructive criticism and feedback for many of my presentations and manuscripts.

In addition, a great thanks to Professor Carl White and his research staff in the University of Colorado Denver, who introduced and supported me with the airway inhalation studies. I would like to thank Professor Yona Tadir, Dr. Felicia Lane, Dr. Afiba Arthur, Dr. Neha Talreja for providing the guidance and encouragement in the gynecology project.

I would also like to thank my colleagues in the Chen lab. Dr. Jiang Zhu, Dr. Tiancheng Huo, and Dr. Qiang Yang taught me the technical skills in the optics, data processing, and medical imaging during my training period. Thank you, Dr. Emon Heidari, Jason Chen, Dr. Yan Li, Dr. Youmin He, Dr. Rachel Qu, and many other lab members for your friendship and memorable time in the SPIE Photonics West conference. To Dr. Joseph Jing, I cannot thank you more for guiding me through my first year in the lab and continued to answer the technical questions even after you have moved to a new position. To Danny Chou, you are one of the few people that I know I can always get the right answer from if I encounter an unsolvable problem, whether it is related to research or life. Danny and Joe, you two had an enormous impact on me as a student, a researcher, and as a person.

I am also grateful for my girlfriend, Hoai Chon Nguyen, for constantly providing the mental support and feeding me so that I can focus on my research projects throughout my MS and PhD years. I am very lucky to have you in my life.

Finally, I would like to thank my family. Mom and dad, thank you for always believing in me and constantly showing the support morally as well as economically. Thank you for raising me and always care about my well-being. I love you.

CURRICULUM VITAE

Yusi Miao

Ph.D. in Biomedical Engineering, 2017 - 2020
University of California, Irvine, CA

M.S. in Biomedical Engineering, 2014 - 2017
University of California, Irvine, CA

B.S. in Applied Physics and Physico-Informatics, 2009 - 2013
Keio University, Tokyo, Japan

HONORS AND AWARDS

ASLMS Best of Session Award (2020)
ASLMS Educational Scholarship (2019&2020)
Samueli School of Engieering PhD Bridge Fellowship (2016)

LIST OF PUBLICATIONS

1. Moon, S*, **Miao, Y***, Chen, Z ,"Fiber-based polarization-sensitive optical coherence tomography of a minimalistic system configuration", Optics Letters (2019) ***Contributed equally**
2. **Miao, Y**, Choi, JH, Chou, LD, Desai, V, Roberts, TR, Beely, BM, Wendorff, DS, Espinoza, M, Sieck, K, Cancio, LC, Brenner, M, Batchinsky, AI, Chen, Z, "Automatic Proximal Airway Volume Segmentation Using Optical Coherence Tomography for Assessment of Inhalation Injury", Journal of Trauma and Acute Care Surgery (2019)
3. **Miao, Y**, Chen, Z, Li, SC, "Functional endoscopy techniques for tracking stem cell fate", Quantitative Imaging in Medicine and Surgery (2019)
4. **Miao, Y,** Brenner, M, Chen, Z, "Endoscopic Optical Coherence Tomography for Assessing Inhalation Airway Injury: A Technical Review", Otolaryngology (2019)
5. Li, Y*, Sudol, NT*, **Miao, Y***, Jing, JC, Zhu, J, Lane, F, Chen, Z, "1.7 micron optical coherence tomography for vaginal tissue characterization in vivo", Lasers in surgery and medicine (2019) ***Contributed equally**
6. **Miao, Y**, Jing, J, Desai, V, Mahon, S, Brenner, M, Veress, LA, White, CW, Chen, Z, " Automated 3D segmentation of Methyl isocyanate-exposed Rat Trachea using an ultra-thin, fully fiberoptic optical coherence endoscopic probe," Scientific Report (2018)
7. Yang, Q, **Miao, Y**, Huo, T, Li, Y, Heidari, E, Zhu, J, Chen, Z, "Deep imaging in highly scattering media by combining reflection matrix measurement with Bessel-like beam based optical coherence tomography," Applied Physics Letter (2018)
8. Zhu, J*, **Miao, Y***, Qi, L, Qu, Y, He, Y, Yang, Q, Chen, Z, "Longitudinal shear wave imaging for elasticity mapping using optical coherence elastography," Applied Physics Letter (2017) ***Contributed equally**

9. Yan, L, Jing, J, Qu, Y, **Miao, Y**, Zhang, B, Ma, T, Yu, M, Zhou, Q, Chen, Z, "Fully integrated optical coherence tomography, ultrasound, and indocyanine green-based fluoresence tri-modality system for intravascular imaging," Biomedical optics express (2017)
10. Qu, Y, Ma, T, He, Y, Yu, M, Zhu, J, **Miao, Y**, Dai, C, Patel, P, Shung, KK, Zhou, Q, Chen, Z, " Miniature probe for mapping mechanical properties of vascular lesions using acoustic radiation force optical coherence elastography," Scientific Report (2017)
11. Qu, Y, He, Y, Zhang, Y, Ma, T, Zhu, J, **Miao, Y**, Dai, C, Silverman, RH, Humayun, MS, Zhou, Q, Chen, Z, "Quantified elasticity mapping of retinal tissue using acoustic radiation force optical coherence elastography," Investigative Opthalmology & Visual Science (2017)
12. Yan, L, Jing, J, Qu, Y, **Miao, Y**, Zhang, B, Ma, T, Yu, M, Zhou, Q, Chen, Z, "Fully integrated optical coherence tomography, ultrasound, and indocyanine green-based fluoresence tri-modality system for intravascular imaging," Biomedical optics express (2017)
13. Porcaro, F, **Miao, Y,** Kota, R, Haun, JB, Polzonetti, G, Battocchio, C, Gratton, E, "Fluctuation Spectroscopy Analysis of Glucose Capped Gold Nanoparticles," Langmuir (2016)
14. Zhu, J, Qi, L, **Miao, Y,** Ma, T, Dai, C, Qu, Y, He, Y, Gao, Y, Zhou, Q, Chen, Z, "3D mapping of elastic modulus using shear wave optical micro-elastography," Scientific reports (2016)

HIGHLIGHTED CONFERENCE PRESENTATIONS

Miao, Y, Li, Y, Sudol, NT, , Jing, JC, Zhu, J, Lane, F, Chen, Z,"3D visualization of vaginal histopathology after fractional CO2 laser treatment using optical coherence tomographic endoscopy," SPIE Photonics West, San Francisco, CA, Oral Presentation (2019).

Miao, Y, Zhu, J, Li, Q, Qu, Y, He, Y, Gap, Y, Chen, Z, "Longitudinally polarized shear wave optical coherence elastography," SPIE Photonics West, San Francisco, CA, Oral Presentation (2017).

Miao, Y, Zhu, J, Qu, Y, Ma, T, Li, R, Du, Y, Huang, S, Shung, KK, Zhou, Q, Chen, Z, "Imaging shear wave propagation for elastic measurement using OCT Doppler variance method," SPIE Photonics West, San Francisco, CA, Oral Presentation (2016).

PATENTS

Chen, Z, Miao, Y, Li, Y, Tromberg,BJ, Tadir, Y, Optical biopsy applicators for treatment planning, monitoring, and image-guided therapy, Pending (20190200851A1)

ABSTRACT OF THE DISSERTATION

Endoscopic Optical Coherence Tomography:
New Applications and Quantification Techniques

By

Yusi Miao

Doctor of Biomedical Engineering

University of California, Irvine, 2020

Professor Zhongping Chen, Chair

Optical coherence tomography (OCT) is an emerging medical imaging technique that provides tissue cross-sectional images with micrometer resolution in near real-time using a nondestructive method. OCT holds great potential in endoscopic applications, such as airway monitoring, since the *in situ* and intra-operative monitoring of disease sites using a minimally imaging technique can lead to early diagnosis and treatments. In addition, such a minimally invasive imaging tool is capable of guiding biopsy and histology, reducing sampling error, and improving biopsy yield.

One limitation of current endoscopic OCT is the limited capability to accurately assess the early changes in the tissue microarchitecture and functionality in airway disorders and injuries. This thesis focuses on demonstrating the advancement in the quantitative analysis methods and functional imaging techniques that will lead to the enhanced visualization of early tissue composition and functional changes, thus improving disease prognosis. Towards this goal, two key technological advancements have been made. First, digital quantitive analysis techniques were demonstrated based on two image segmentation algorithms: graph

theory and deep learning. Importantly, this work evaluated the accuracy of computer-aided analysis compared to a human reader and demonstrated the robustness of the automated segmentation algorithm. Second, we proposed and demonstrated three novel functional imaging techniques to quantify mechanical properties, sub-micron cellular movement, and birefringence in the airway; those were based on i) dynamic airway compliance measurement using a high-speed micromotor OCT probe, ii) spectrally-encoded Doppler measurement using a high-resolution OCT system, and iii) polarized light illumination and detection using a fiber-based polarization-sensitive OCT system.

To demonstrate and evaluate the utility of those technological advancements in a clinical setting, we performed *ex vivo* tissue imaging, postmortem animal imaging, *in vivo* animal studies of toxic agents, and *in vivo* imaging of a human upper airway. The findings demonstrated that automated tissue detection and segmentation combined with functional imaging can significantly improve the understanding of early airway pathology and function in disease progression.

Finally, this research work also explored the new application of OCT in gynecology. Visual inspection and self-reported symptoms are currently used in clinical diagnosis to monitor the progression and treatment of menopausal patients. However, they lack the objectivity to accurately understand each patient's condition. OCT has been shown to provide quantitative tissue information and has been widely adopted in the field of dermatology. With further progress, OCT can be a new powerful tool in the field of pelvic medicine.

Chapter 1 – INTRODUCTION

1.1 Overview

Optical coherence tomography (OCT) is a developing medical imaging technique that has immense clinical potential as a mesoscopic imaging tool. It has a unique capability of being able to visualize tissue microstructure a few millimeters below the surface with 1 – 10 um spatial resolution in real-time. To date, the dominant application of OCT is in ophthalmology as it allows noninvasive and noncontact imaging of the anterior eye as well as retinal layer structures [1, 2]. More recently, advances in OCT technology enable it to be applied to a wide range of medical fields such as cardiology, dermatology, gastroenterology, and otolaryngology. Airway injury and disorders are especially active areas of research due to the importance of basic physiological function. The clinical utility of the technology, however, highly depends on the relevance of the measurement results to early-stage tissue alteration as well as how well disease progression can be predicted. This thesis explores new techniques for endoscopic airway imaging that significantly enhance the quantitative analysis and functional imaging of conventional OCT imaging. Specifically, this work developed technology to enable quantitative analysis in airway inhalation injury and visualization of the cellular activity and sub-micron tissue structure. Animal studies and clinical tests were performed to assess the feasibility of the translation of this technology for clinical application.

1.2 Airway Injuries and Disorders

1.2.1 Acute Airway Injuries

Despite the recent advancements in therapeutics and counteragents, mortality and morbidity from inhalation injury remain high [3, 4]. Inhalation of toxins often affects multiple airway sites at different times, making diagnosis and prediction of injuries challenging: it often results in a combination of 1) thermal damage in the upper airway, 2) chemical injury that affects both the upper and lower respiratory tract, and 3) systematic effects from toxins, such as CO, CN, and cyanide [5]. Heated air from fires can cause thermal injury to the upper airway which leads to swelling and edema of the tongue, epiglottis, and aryepiglottic folds [6]. If significant thermal damage is suspected, continuous monitoring is required to assess the need for ventilation. Chemical irritants can affect the airway at different levels depending on their chemical characteristics and water solubility with smaller particles and less water-soluble gases generally affecting the lower respiratory tract. Inhalation of chemical irritants often results in mucosa damage, leading to ciliastasis, epithelium denudation, sloughing, airway obstruction, and pulmonary edema [7, 8]. The number of substances that can cause severe lung damage continues to expand in both occupational and domestic settings. Besides direct and immediate effects, in many cases, inhalation injury is accompanied by inflammatory responses that can prolong the ventilation period and increase the risk of acute respiratory distress syndrome. Therefore, accurate diagnosis and continuous monitoring of affected airway tissue are crucial.

Methyl isocyanate (MIC) is an industrial byproduct. Accidental release of MIC in Bhopal, India, killed thousands of civilians which was considered one of the worst industrial disasters in history [9]. Inhalation of the gas causes airway edema and epithelium delamination, leading to substantial airway obstruction. The mechanism of MIC has been studied in mice [10] and rats [11],

but no effective rescue agents have been developed. Miao *et al.* first demonstrated that the degree of airway obstruction can be quantified in a rat exposed to MIC using a miniature OCT endoscope [12]. Combined with an automated segmentation technique based on graph theory, OCT provides capabilities for rapid assessment of airway structure, volume, site of maximum airway constriction, and aerodynamic characteristics.

Sulfured mustard is a vesicant, or blistering, agent and can cause significant tissue damage, leading to obstruction and edema. Hammer-Wilson *et al.* first demonstrated the potential use of an optical endoscopic method in detecting tissue damage due to exposure to 2-chloro-ethyl-ethyl-sulfide, known as half mustard, using a hamster cheek model [13]. OCT was able to detect morphological changes in the mucosa and muscular layer that were not visible on gross visual examination such as bronchoscopy. Kreuter *et al.* then reported the changes in the airway epithelium and mucosa *in vivo* in a ventilated rabbit exposed to half mustard [14]. The endoscopic OCT probe was placed at the distal portion of the trachea. The changes in the epithelium were apparent within a few minutes after exposure in OCT images, and signs of epithelium detachment and hemorrhage continued to develop over the next few hours.

Smoke inhalation injury is the leading cause of death in fire victims. In modern burn care, diagnosis of inhalation injury has been a particularly challenging yet an important problem. Inhalation injury complicates the burn and increases mortality and morbidity for up to 20% of burn patients [15]. Numerous studies have used endoscopic OCT in combination with a flexible bronchoscope to assess early changes in the tissue histopathology and predict the outcome [16–21]. Most of those studies focused on the quantification of mucosa and airway epithelial thickness after exposure to cold smoke. Brenner *et al.* reported that early tissue changes, such as hyperemia

and edema, observed during *in vivo* OCT imaging were lost during the histological preparation, indicating the importance of a non-invasive, intra-operative imaging technique [19].

1.3 Clinical Diagnosis of Airway

Currently, the clinical diagnosis and monitoring of airway inhalation injury rely on subjective clinical exams and bronchoscopic findings. However, only the superficial tissue can be seen using a bronchoscope, and the measurements from clinical exams are subjective. Computerized tomographic (CT) scanning has recently been proposed for quantitative airway injury assessment [4]. Three-dimensional reconstruction of the airway from a chest CT can provide information on airway narrowing [5]. However, the CT scan does not provide enough spatial resolution to identify early tissue damage, such as hyperemia, sloughing, necrosis, and inflammation, and thus, CT cannot provide an accurate assessment of inhalation injury by itself [6]. In addition, repeated CT measurement exposes the patient to the risks of ionizing radiation. Magnetic resonance imaging (MRI) has many of the same capabilities as CT without the drawback of ionizing radiation. However, neither MRI or CT have the spatial resolution to resolve micron-scale airway tissue structure. In addition, their cost and the complexity of the screening make them unsuitable as large-scale diagnostic platforms for airway injuries. Therefore, a medical imaging tool that can detect early signs of airway injuries as well as monitor the recovery process is required to improve patient outcomes.

1.4 Optical Coherence Tomography

OCT provides non-invasive and real-time visualization of biological tissue 1-3 mm beneath the surface with virtually histologic-level resolution. OCT has previously been used in ophthalmology, cardiology, and dermatology to improve patient outcomes. Recent advancements

in a high-speed swept-source laser allow volumetric scanning of tissue substructure in real-time during procedural settings [7]. Since the imaging part of OCT can be made with fiber optics, OCT can be made into a miniature rigid or flexible endoscopic probe to visualize internal organs that were previously hard to reach, similar to fiber optic bronchoscopy. Endoscopic OCT has started to be utilized in humans in clinical settings to visualize the respiratory tract [8–10] and gastrointestinal tract [11,12].

1.5 Endoscopic Optical Coherence Tomography

Several studies have used endoscopic OCT to study airway diseases and disorders [22–26]. Endoscopic OCT commonly employs fiber optic-based imaging techniques that can be combined with other imaging modalities, such as bronchoscopy, to examine internal organs. Tearny *et al.* reported the first application of an endoscopic OCT study in an *in vivo* rabbit trachea using a time-domain (TD) OCT system [27]. With the advancement of the high-speed sweeping laser, the imaging speed and sensitivity of endoscopic OCT has improved in recent years.

Endoscopic OCT has been used in numerous inhalation injury studies to assess tissue damage and predict outcome from toxic gas exposure [16, 19, 21, 28]. Epithelium and mucosa layer thickness are the main parameters that have been used to assess early tissue response to the inhaled substance. It was demonstrated that the mucosa thickness reflects the early changes in the tissue, and OCT has a capability to assess those subtle changes whereas traditional diagnosis requires longer observation time [16]. In addition to the mucosa thickness, OCT has been used to quantify airway volume [12]. The degree of airway obstruction and edema can be correlated with the airway volume. Furthermore, temporal changes in the airway volume can be utilized to estimate airway compliance which relates to the mechanical properties [29–31].

1.6 Statement of Work

The aims of this thesis work were as follows: 1) to develop a modular imaging system and probe that can perform endoscopic OCT imaging in a small animal as well as a human subject; 2) to evaluate the capabilities of an automated segmentation algorithm for extracting airway wall tissue information as well as anatomical structure in inhalation injuries; 3) to develop an extension of the OCT technique called polarization-sensitive OCT to investigate birefringence characteristics; 4) to develop a reliable method to investigate the local mechanical properties in the airway; 5) to explore a functional imaging method based on OCT to visualize the ciliary motion in the airway.

The written thesis is organized according to these aims. Chapter 2 presents the brief principle of OCT imaging and some of the design considerations for a clinical imaging system. In Chapter 3, I will discuss the two segmentation methods for the quantitative analysis of airway imaging data. Chapters 4 and 5 show how the endoscopic OCT technique combined with automated segmentation can evaluate severity and sites of the injuries using toxic inhalation models. Chapter 6 presents an integrated OCT and pressure transducer to compute airway compliance. Chapter 7 presents a new imaging method based on optical coherence microscopy (OCM) and a confocal microscope to detect ciliary beating motion. Chapter 8 introduces a simple method to convert conventional OCT into a polarization sensitive (PS) OCT imaging system to be able to detect birefringence. Chapter 9 shifts the focus to a new application of endoscopic OCT and discusses how OCT can be used in gynecology to guide laser therapy. Chapter 10 concludes the thesis by providing summary and future perspectives.

Chapter 2 – Optical Coherence Tomography Principles

2.1 Overview

This chapter discusses the basic principle of traditional time-domain OCT and modernized Fourier-domain OCT. We will discuss mathematical theory as well as other key parameters in OCT such as spatial resolution, sensitivity, and imaging range. Finally, Doppler OCT will be discussed as a functional extension of OCT imaging.

2.2 Introduction

In some medical applications, such as ophthalmology and cardiology, OCT has become a powerful diagnostic tool to detect and monitor diseases. OCT imaging is analogous to ultrasound imaging; however, it uses light instead of sound to visualize tissue cross-sections. Due to the wavelength difference of light compared to sound, OCT can visualize tissue microstructure with 1 – 10 um spatial resolution, about 2 – 3 magnitudes higher than clinical ultrasound. In addition, a typical OCT imaging system utilizes low power near-infrared light, which causes minimal damage to the biological tissue. OCT is generally categorized into two types based on the system setup: time-domain and frequency-domain.

In time-domain (TD) OCT, the optical path length of the reference arm in an interferometer is mechanically varied to get signals at different depths of the sample. Therefore, the imaging range of TD-OCT is determined by the moving range of the reference arm. The main limitation of TD-OCT is scanning speed. To achieve real-time imaging with TD-OCT, several groups adopted a rapid scanning optical delay line in the reference arm to scan across the sample. In this setup, the group delay was changed rapidly by moving a mirror mounted on a galvanometer, allowing 500

A-line scans per second with a 36 mm scanning distance [32]. However, there is a tradeoff between the scanning speed and sensitivity in TD-OCT so fast scanning will result in a lower signal-to-noise ratio.

With the development of Fourier Domain (FD) OCT, the speed and sensitivity of imaging have significantly improved. Since FD-OCT obtains depth information of the sample simultaneously through a wavelength-sweeping laser or a spectrometer and broad-band laser rather than mechanically scanning the reference arm, the imaging speed can be much faster than TD-OCT. In addition, FD-OCT does not have to sacrifice axial resolution for speed. However, the main drawback of FD-OCT is the finite imaging range. Typically imaging the entire airway lumen requires a 25 mm imaging range. Jun *et al.* overcame the short imaging range by implementing a phase modulator and effectively doubled the imaging range [33]. More recently, Jing *et al.* applied a vertical cavity surface emitting laser (VCSEL)-based swept-source laser and achieved long-range OCT imaging with much higher sensitivity by taking advantage of its narrow instantaneous pulse width of the light source [25]. Super-high-speed endoscopic imaging using a Fourier domain mode lock laser has been demonstrated with an MHz scanning rate [34]. In addition to the speed, the axial resolution has been improved up to 1 um by using a broad bandwidth light source such as a supercontinuum [35, 36].

Another major advancement in OCT is the development of Doppler OCT, a functional extension of traditional OCT imaging [37–39]. Doppler OCT utilizes the Doppler principle to quantify the velocity of a moving particle including blood flow. In this chapter, I will discuss the mathematical principle of OCT and some of the technologies that contributed to the advancement of the resolution, sensitivity, speed, and imaging range.

2.3 Time Domain (TD) OCT

The generic system setup for TD-OCT imaging is Michelson's interferometer (**Figure 2.1**). The collimated beam from a low-coherence light source is divided into a sample and a reference arm with a 50/50 ratio. The portion of the light that enters the reference arm is incident upon a reference delay, often consisting of a retro-reflector, and redirected back to the beam splitter. The portion of the light that enters the sample arm is incident upon an optomechanical system that is designed to focus the collimated light into a targeted sample and repeatedly scan in one or two-dimensions. The scanning of the beam is often controlled by a computer. Then, the back-reflected light from the sample is redirected to the beam splitter. Finally, the redirected light from both sample and reference arms is combined, and the constructive and deconstructive interference pattern will be formed in the photodetector.

In TD-OCT, the light source is a broad-band continuous-wave light, the amount of reference delay is repetitively changed to scan across the depth, and the photodetector consists of a single-channel detector. The envelope of the fringe burst detected in the detector corresponds to the depth-resolved reflectivity of the targeted sample. The bandwidth of the light source determines the coherence length and affects the axial resolution of the image.

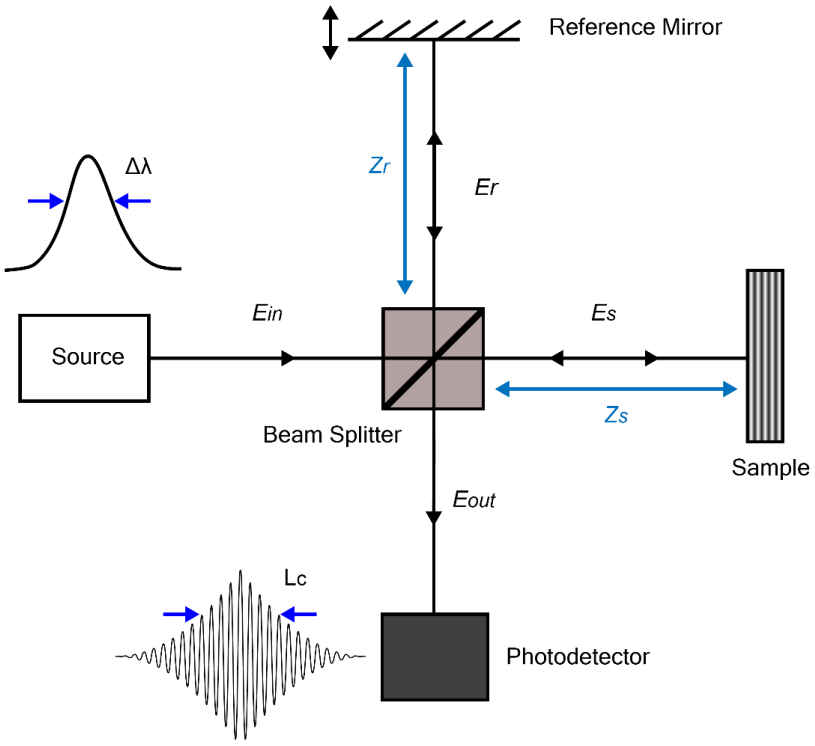

Figure 2.1 Schematic of TD-OCT system consists of a Michelson's interferometer with a low coherence source.

2.3.1 Theory of TD-OCT

To understand the principle of low-coherence interferometry, we consider the interference signal created in a Michelson's interferometer in **Figure 2.1**. The electric field of the illumination light from the source can be described as:

$$E_i = s(k,\omega)e^{i(kz-\omega t)} \tag{2.1}$$

where $s(k,\omega)$ is the amplitude of the electric field as a function of wavenumber $k = 2\pi/\lambda$, and angular frequency $\omega = 2\pi v$. In our case, angular frequency component can be ignored since v oscillates much faster than the response time of the detector. For simplicity, we will consider the sample consists of a single reflector. Now, the back-reflected light from the sample and reference can be described as:

$$E_s = \frac{s(k,\omega)}{\sqrt{2}} r_s e^{i(2kz_s - \omega t)} \tag{2.2}$$

$$E_r = \frac{s(k,\omega)}{\sqrt{2}} r_r e^{i(2kz_r - \omega t)} \tag{2.3}$$

where r_s and r_r are the sample and reference reflectivity, z_s and z_r are the optical path length of sample and reference arm. The factor of 2 in the exponential term accounts for the round-trip distance in each arm. In the detector, two electric fields from the sample and reference arms are combined, detected as an electric power, then converted into electric current:

$$I_D(k,\omega) = \frac{\rho}{2}\langle |E_s + E_r|^2 \rangle \tag{2.4}$$

$$= \frac{\rho}{2}\langle (E_s + E_r)(E_s + E_r)^* \rangle$$

where ρ is the responsivity of the photodetector, $\langle \quad \rangle$ represents the integration over the response time of the detector, * represents complex conjugate. Inserting equations (2.2) and (2.3) into (2.4) results in:

$$I_D(k) = \frac{\rho}{2}\langle \left| \frac{s(k,\omega)}{\sqrt{2}} r_s e^{i(2kz_s)} + \frac{s(k,\omega)}{\sqrt{2}} r_r e^{i(2kz_r)} \right|^2 \rangle \tag{2.5}$$

Here, the angular frequency term is eliminated for simplicity as the angular frequency exceeds the integration time of the detector:

$$I_D(k) = \frac{\rho}{2}\langle \left| \frac{s(k,\omega)}{\sqrt{2}} r_s e^{i(2kz_s)} + \frac{s(k,\omega)}{\sqrt{2}} r_r e^{i(2kz_r)} \right|^2 \rangle \tag{2.6}$$

Expanding equation (2.6) yields

$$I_D(k) = \frac{\rho}{4}\left\{ S(k)(R_s + R_r) + S(K) \cdot \sqrt{R_s R_r}\left(e^{i2k(z_s - z_r)} + e^{-i2k(z_s - z_r)} \right) \right\} \tag{2.7}$$

$$= \frac{\rho}{4}\left\{ S(k)(R_s + R_r) + S(K) \cdot \sqrt{R_s R_r}(\cos 2k(z_s - z_r)) \right\}$$

where $S(k) = \langle |s(k,\omega)|^2 \rangle$ is the power spectrum of the laser source. $R_s = |r_s|^2$ and $R_r = |r_r|^2$ are the power reflectivity of the sample and reference arms, respectively. The detected signal is composed of the DC term proportional to the reflectivity from the sample and the reference and the cross-correlation term with the frequency depending on the optical path difference (OPD) of the two arms.

In reality, the sample consists of depth-dependent multiple reflective surfaces. For simplicity, we assume the sample reflectivity as a series of delta functions scaled at a distinct reflective coefficient as follows:

$$r_s(z) = \sum_{i=1}^{N} r_{sn} \cdot \delta(z - z_{sn}) \tag{2.8}$$

The detector current can be now described as

$$\begin{aligned} I_D(k) = \frac{\rho}{4}\Bigg\{ & S(k) \cdot \left(R_r + \sum_{n=1}^{N} R_{sn} \right) + 2S(k) \\ & \cdot \sum_{n=1}^{N} \sqrt{R_r \cdot R_{sn}} \big(cos2k(z_r - z_{sn}) \big) + S(k) \\ & \cdot \sum_{n \neq m=1}^{N} \sqrt{R_{sn} \cdot R_{sm}} \big(cos2k(z_{sn} - z_{sm}) \big) \Bigg\} \end{aligned} \tag{2.9}$$

Equation (2.9) comprises of three distinct components. The first DC term corresponds to the summation of the light reflected from the sample and reference, and this is independent of OPD. The second term is the cross-correlation term that contains the desired interferometric signal which encodes the information of the depth-dependent reflectivity of the sample. The square root dependence to the reference reflectivity also gives a logarithmic gain factor over the direct detection of the sample. Finally, the third term describes the auto-correlation term from the interference between the different sample planes. These third terms are typically considered non-

desirable terms since they can interfere with the second term. However, a proper selection of the sample and the reference power can decrease the auto-correlation artifacts.

In TD-OCT, the wavenumber dependent detector current $I_D(k)$ is captured by a single detector, and the reference length z_r is rapidly scanned to retrieve sample reflectivity $\sqrt{R_{sn}}$. Here, the light source spectrum S(k) is assumed to be a Gaussian function and its Fourier transformation can be described as the Gaussian-shaped coherence function

$$S(k) = \frac{1}{\Delta k\sqrt{\pi}} e^{-\left[\frac{(k-k_0)}{\Delta k}\right]^2} \overset{F}{\leftrightarrow} \gamma(z) = e^{-(z)^2\Delta k^2} \tag{2.10}$$

The integration of equation (2.9) over wavenumber k gives

$$I_D(z_r) = \frac{\rho}{4}\left\{S_0 \cdot \left(R_r + \sum_{n=1}^{N} R_{sn}\right) + 2S_0 \cdot \sum_{n=1}^{N} \sqrt{R_r \cdot R_{sn}} e^{-[(z_r - z_{sn})]^2\Delta k^2} \left(cos 2k_0(z_r - z_{sn})\right)\right\} \tag{2.11}$$

where $S_0 = \int S(k)dk$ is the integrated power of the light source. Equation (2.11) can be understood as a convolution of the source spectrum across the reflectivity in the sample with the sinusoidal modulation frequency proportional to the center wavelength of the light source k_0 and the OPD of the two arms.

2.3.2 Axial resolution of TD-OCT

In OCT systems that employ a low numerical aperture objective, axial resolution Δz is independent of its lateral resolution. In the OCT imaging system, the axial point spread function (PSF) is determined by the coherence length (l_c) of the light source and described as the equation below:

$$\Delta z = l_c = \frac{2\ln(2)}{\pi}\frac{\lambda_0^2}{\Delta\lambda} \tag{2.12}$$

where $\Delta\lambda$ is the spectral bandwidth and λ_0 is the center wavelength of the light source. Intuitively, coherence length can be understood as the OPD range where the interference occurs between the reference and sample arms. Eq. (2.12) shows that the axial resolution of an OCT imaging system can be improved by either using lower wavelength light or increasing the bandwidth. However, the bandwidth is often limited due to the physical material properties of the laser.

2.3.3 Lateral resolution of TD-OCT

Similar to the conventional microscope, the lateral resolution of an OCT imaging system depends on the numerical aperture (NA) of the objective lens and the beam spot size illuminated to the sample. Assuming Gaussian profile sample illumination, the lateral resolution (Δx) of OCT can be described as

$$\Delta x = \frac{2\lambda}{\pi}\frac{1}{NA} = \frac{4\lambda}{\pi}\frac{f}{d} \tag{2.13}$$

Here, f is the focal length and d is the entrance pupil diameter of the sample beam. It is evident that increasing the numerical aperture of the lens will produce a smaller beam spot size at the focus and result in smaller lateral resolution. However, there exists a trade-off relationship between the lateral resolution and the axial field-of-view (FOV), or depth of focus (DOF). The DOF of a Gaussian illumination beam from an objective lens is described as double of the Rayleigh length z_R, which is the distance from the focal plane to the axial point where the cross-sectional area of the beam doubles:

$$DOF = 2 \cdot z_R = \frac{\pi\Delta x^2}{2\lambda} \tag{2.14}$$

From Eq. (2.14), it is evident that increasing the NA of the objective lens will result in superior lateral resolution, but the axial range where the resolution is maintained will be reduced.

2.3.4 Sensitivity of TD-OCT

Sensitivity, or dynamic range, in an OCT imaging system is defined as the ratio of signal power generated from a perfect reflector over the noise power. The sensitivity analysis of TD-OCT is well documented in optical coherence domain reflectometry (OCDR) or low-coherence interferometry (LCI) studies. Three primary noise sources in OCT systems are the shot noise σ_{SH}, the relative intensity noise σ_{RIN} of the light source, and the thermal noise σ_{TH} of the photodetector:

$$\sigma_{total}{}^2 = \sigma_{SH}{}^2 + \sigma_{RIN}{}^2 + \sigma_{TH}{}^2 \tag{2.15}$$

Here, the total noise σ_{total} is the square sum of all the noises since only the noise power is additive. It is important to note that noise has a zero mean and, therefore, can be described as its variance. In most OCT systems, the shot noise dominates the other two noise sources and, thus, can be considered as a shot-noise-limited system. Assuming the light reflected from the sample arm is much weaker than the reference arm, the mean photodetector current is dominated by the reference power and the noise can be described as

$$\sigma_{SH}{}^2 = \rho e P_{TDOCT} R_r B_{TDOCT} \tag{2.16}$$

where ρ is the responsivity of the photodetector, e is the electron charge, P_{TDOCT} is the instantaneous optical power, B_{TDOCT} is the full-width-half-maximum (FWHM) power bandwidth of the photodetector, and R_r is the light reflectivity of the reference arm.

The peak detector current from an ideal signal (I_d) occurs when the OPD is zero and given as:

$$\langle I_d \rangle_{TD}^2 = \frac{\rho^2 P_{TDOCT}^2}{2} [R_r R_s] \tag{2.17}$$

Therefore, the signal-to-noise (SNR) ratio for TD-OCT is given by

$$SNR_{TD} = \frac{\langle I_d \rangle_{TD}^2}{\sigma_{TD}^2} = \frac{\rho P_{TDOCT} R_s}{2eB_{TDOCT}} \tag{2.18}$$

In TD-OCT, depth scan is performed by the uniform-velocity mechanical movement in the reference arm which results in a Doppler frequency shift in the detected signal. The Doppler frequency shift (f_D) and the FWHM power spectrum of the signal (Δf) as a result of the uniform scan in the reference arm (υ) are given as

$$f_D = 2\frac{v}{\lambda} \tag{2.19}$$

$$\Delta f = \ln(4)\frac{4}{\pi}\frac{v}{l_c} = \frac{4\sqrt{\ln(2)}}{\pi}\upsilon\Delta k \tag{2.20}$$

Where Δk is the spectral bandwidth of the light source, and can be described by the center wavelength of the light source λ_0 and its wavelength bandwidth $\Delta\lambda$ as $\Delta k = \frac{\pi}{\sqrt{\ln(2)}}\frac{\Delta\lambda}{\lambda_0^2}$.

By the Nyquist theorem, the optimum bandwidth of the bandpass filter is $2\Delta f$:

$$B_{TDOCT} = 2\Delta f = \frac{8\sqrt{\ln(2)}}{\pi}\upsilon\Delta k \tag{2.21}$$

Therefore, it is evident that the SNR of the TD-OCT system is linked to the scanning speed as well as to the axial resolution. At a given imaging range and a given A-scan acquisition time, a wider detection bandwidth will decrease sensitivity whereas a narrower detection bandwidth will decrease the axial resolution. At a given detector bandwidth and a given A-scan acquisition time, increasing the maximum imaging range will be penalized by degradation of the axial resolution. Spatial resolution, scan speed, maximum imaging range, and dynamic range of TD-OCT should be designed and optimized based on the application.

2.3.5 Imaging range of TD-OCT

The imaging range in OCT is defined as the total OPD length that the signal can be acquired whereas the penetration depth in OCT is a function of scattering properties and wavelength. In TD-OCT setups, the imaging range depends on the scanning distance of the reference arm and has no physical limits. Several approaches have been proposed to effectively scan the reference path. The piezoelectric transducers and linear translation stage are conventional depth scanning approaches in TD-OCT, but the scanning speed is generally limited in those approaches [40, 41]. Another scan approach in TD-OCT systems is called rapid scanning optical delay (RSOD). RSOD utilizes scanning galvanometers and a spinning mirror or spinning glass cube pairs to generate a high-speed axial scanning rate of up of 100-400 Hz [42, 43]. Although a higher scanning rate can be achieved, these methods can introduce delay-dependent nonuniformity and have limited scan range. Another related technique of RSOD utilizes a spatially diffractive grating paired with a galvanometer to generate an optical group delay by scanning the angle of a beam instead of employing mechanical translation [44, 45]. This approach has the advantage of generating a relatively long scanning range and a repetition rate of up to 2 kHz. However, the trade-off between the sensitivity and the scanning speed still poses fundamental limitations to TD-OCT systems.

2.4 Fourier Domain (FD) OCT

In TD-OCT systems, image acquisition speed is limited by the mechanical scanning speed of the reference arm. After 1995, to overcome the speed limitation and increase the sensitivity, Fourier domain or frequency domain OCT (FD-OCT) was demonstrated by Fercher *et al.* [46]. In FD-OCT, the reference arm is fixed at the position that corresponds to the position of the sample, and the spectral interference signal is used to reconstruct the depth profile of the backscattered

photons in the sample. Since FD-OCT does not have any mechanical moving components in the reference arm, the image acquisition speed can be 2–6 orders of magnitude faster than conventional TD-OCT systems [47]. Additionally, several studies have suggested 20 dB or a greater sensitivity advantage of the FD-OCT scheme over comparable TD-OCT schemes [48–50]. FD-OCT is subdivided into spectral domain (SD) systems and swept-source (SS) systems **(Figure 2.2)**. In SD-OCT systems, the light source is a broadband continuous wavelength light source, and the spectral interference pattern is detected in a spectrometer which consists of an array detector, such as a charge-couple device (CCD) or a complementary metal-oxide sensor (CMOS). In the SS-OCT system, the source is a narrow-band wavelength sweeping laser, and spectral interference as a function of time is detected by a single photoreceiver. In both systems, a depth-resolved reflectivity of the sample, or A-line, can be recovered using inverse Fourier transformation of the spectral interference.

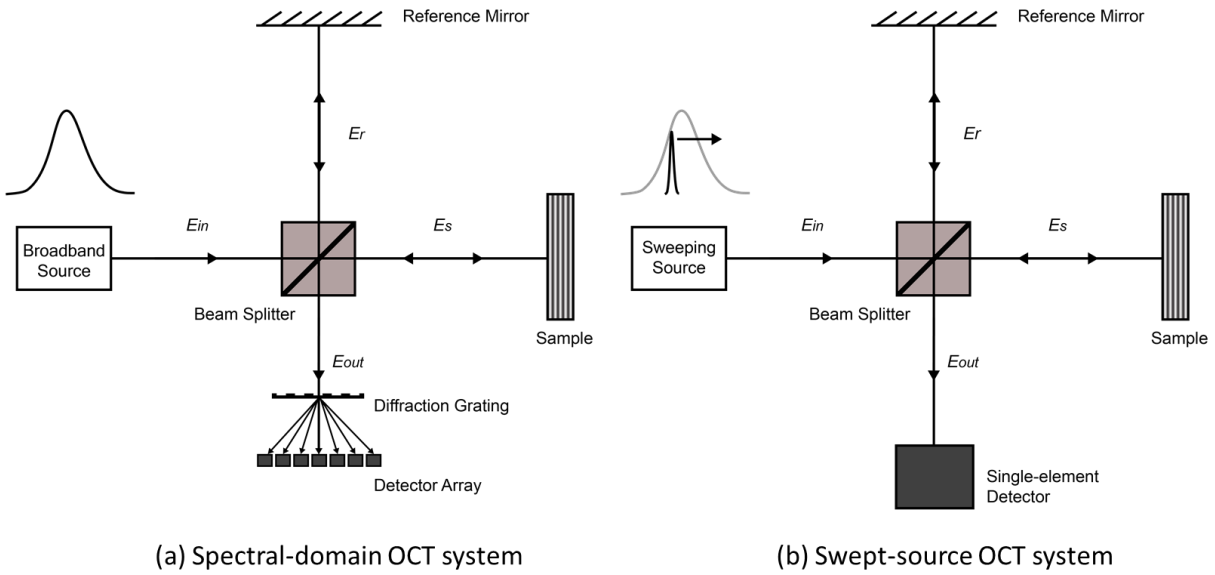

Figure 2.2 Schematic of (a) SD-OCT system and (b) SS-OCT system.

2.4.1 Theory of FD-OCT

In FD-OCT, the wavelength-dependent signal $I_d(k)$ in Eq. (2.9) is captured in the detector. Then, the axial scattering profile is calculated using inverse Fourier transformation. Applying the Fourier transformation pair $\mathcal{F}^{-1}(\cos(k \cdot z_0)) = \frac{1}{2}\left[\left(\delta(z + z_0) + \delta(z - z_0)\right)\right]$ and $\mathcal{F}^{-1}\big(X(k) \cdot Y(k)\big) = X(z) \otimes Y(z)$ into Eq. (2.9) gives

$$I_d(z) = \frac{\rho}{8}\left[\gamma(z) \cdot \left(R_r + \sum_{n=1}^{N} R_{sn}\right)\right] + \frac{\rho}{4}\left[\gamma(z) \otimes \sum_{n=1}^{N} \sqrt{R_r \cdot R_{sn}}\big(\delta(z \pm 2(z_r - z_{sn}))\big)\right] + \frac{\rho}{8}\left[\gamma(z) \otimes \sum_{n \neq m=1}^{N} \sqrt{R_{sn} \cdot R_{sm}}\big(\delta(z \pm 2(z_{sn} - z_{sm}))\big)\right] \tag{2.22}$$

where $\gamma(z) = \mathcal{F}^{-1}(S(k))$ is the inverse Fourier transform of the spectral power density, $\otimes$ is the convolution operator, and δ indicates the Dirac delta function. Eq. (2.22) consists of three subcomponents: DC term, cross-correlation term, and auto-correlation term. The DC term appears as a high-intensity noise near the 0 OPD position. This term is dominated by the reference arm reflectivity, and therefore, it can be easily removed by recording the signal without the sample and subtracting the "background" signal. The auto-correlation term appears as image artifacts near the zero position as the reflections in the sample tend to be clustered together. Although the auto-correlation artifacts are difficult to remove, the amplitude of this term typically is small compared to the DC and cross-correlation terms as the sample reflectivity is usually much smaller than the reference reflectivity. Hence, a proper selection of the reference power can minimize this term. Lastly, the cross-correlation term contains the desired OCT signal, the sample field reflectivity

profile $\sqrt{R_s(z)}$. The signal profile from this term can be described as a series of delta functions positioned with respect to the pathlength difference with the reference arm mirror position and the amplitude scaled as a function of sample and reference reflectivity. Each sample reflective profile is broadened to a width of about the coherence length by coevolving the coherence function $\gamma(z)$. This determines the PSF, or axial resolution, in the FD-OCT systems. Another consideration for the cross-correlation term is the presence of the mirror images. The mirror image artifact is the blurred version of $\sqrt{R_s(z)}$ formed at the opposite side of the zero pathlength as indicated by $\delta(z \pm 2(z_r - z_{sn}))$. This is called complex conjugate artifacts in FD-OCT and formed as a result of Fourier transformation. Since the recorded interferometric spectrum is real, the resulting inverse Fourier transform must be Hermitian symmetric and conjugate artifacts that will be formed at negative distances whose amplitudes are identical to their positive counterparts. This artifact can be minimized as long as the sample can be kept entirely to one side of the zero pathlength; however, it will effectively reduce the imaging range by half.

2.4.2 Axial resolution of FD-OCT

Similar to TD-OCT, the axial resolution of FD-OCT is determined by the coherence length of the light source. Eq. (2.22) shows the desired signal is a series of source coherence functions positioned at each scattering position. The inverse relationship of the coherence length with respect to the light source bandwidth indicates the increasing fidelity of estimating $\sqrt{R_s(z)}$ can be achieved by using a broad-band light source. Eq. (2.12) gives the axial resolution of the FD-OCT system.

2.4.3 Lateral resolution of FD-OCT

Similar to TD-OCT, the lateral resolution of FD-OCT is decoupled from its axial resolution and solely determined by the imaging optics in the sample arm. Eq. (2.13) gives the lateral resolution of the FD-OCT system.

2.4.4 Sensitivity of FD-OCT

To understand the sensitivity analysis of FD-OCT, we must consider how both the spectral interference signal and noise are sampled and processed in the inverse Fourier transform processes. Under the assumption that the auto-correlation term is much weaker than the other terms, the sampled spectral interference signal can be expressed as

$$I_d(k_m) = \frac{\rho}{2} P_{FD}[k_m] \left[R_r + R_s + 2\sqrt{R_r R_s} cos[2k_m(z_r - z_s)] \right] \tag{2.23}$$

where $P_{FD}[k_m]$ is the instantaneous power incident to the sample that corresponds to the spectral channel k_m. The inverse Fourier transform of the sample spectral signal over all the M wavelength can be described as

$$i_d(z_m) = \sum_{m=1}^{M} I_d(k_m) e^{ik_m z_m / M} \tag{2.24}$$

Now, assuming the case of $z_m = 0$ and the spectral power of source is evenly distributed as a function of wavelength, Eq. (2.24) becomes

$$i_d(z_m = 0) = \frac{\rho}{2} \sqrt{R_r R_s} \sum_{m=1}^{M} P_{FD}[k_m] = \frac{\rho}{2} \sqrt{R_r R_s} \cdot P_{FD}[k_m] \cdot M \tag{2.25}$$

The noise in FD-OCT is also sampled and processed through inverse Fourier transformation. The noise in each spectral channel can be considered as a zero-mean, uncorrelated, Gaussian white noise with a lower limit set by shot noise, assuming the proper selection of the reference power.

Therefore, the total noise variance over all the wavelength is given by the inverse Fourier summation

$$\sigma_{FD}^2[z_m] = \sum_{m=1}^{M} \sigma_{FD}^2[k_m] = \rho e P_{FD}[k_m] R_r B_{FD} \cdot M \tag{2.26}$$

Thus, the SNR of FD-OCT is given by

$$SNR_{FD} = \frac{\langle I_d \rangle_{FD}^2}{\sigma_{FD}^2} = \frac{\rho P_{FD}[k_m] R_s}{4eB_{FD}} \cdot M \tag{2.27}$$

In the case of swept source-based FD-OCT systems, $P_{FD}[k_m] = P_{TD}$ and $B_{FD} = B_{TD}$. In the case of spectral domain systems, $P_{FD}[k_m] = P_{TD}/M$ and $B_{FD} = B_{TD}/M$. Therefore, we can write expression for the SNR of both swept-source OCT and spectral domain OCT as

$$SNR_{FD} = \frac{\rho P_{TD} R_s}{4eB_{FD}} \cdot M = SNR_{TD} \cdot \frac{M}{2} \tag{2.28}$$

Intuitively, the M/2 factor of SNR improvement in FD-OCT systems can be understood from the fact that both FD methods acquire information from all the depths all the time, leading to potential SNR improvement by a factor of M. The SNR decrease by a factor of 2 accounts for the fact that the FD-OCT method generates complex conjugates in the negative sample position. Considering the fact that the number of sampling channel M is at least 10^3 in most FD-OCT systems, we can expect at least a 20 – 30 dB SNR improvement compared to TD-OCT systems.

2.4.5 Imaging range of FD-OCT

While mathematically the inverse Fourier transform of the spectral interferogram gives the depth-dependent reflectivity profile in FD-OCT, some additional factors must be taken into consideration. In practical implementations of these devices, both the instrument that generates spectral interferogram data and the sampling device have real-world limitations that can place constraints on the imaging range of the FD-OCT system. Generally, there are three components

that can limit the imaging range of FD-OCT. First, as was described previously, the inverse Fourier transformation operation generates mirror images at the negative pathlength position due to the fact that the detected signal is real. Without any advanced computation techniques, this forces the imaging sample to be constrained on one side of the path length position which effectively reduces the imaging range by half.

The second constraint arises from the fact that the spectral interferogram always has a limited spectral resolution, denoted by δk. In SS-OCT, δk is limited by the instantaneous pulse width of the sweeping source laser while in SD-OCT, δk is limited by the spectral resolution of the spectrometer. Mathematically, the effect of finite spectral resolution can be modeled applying convolution of a Gaussian function with FWHM of δk to the spectral interferogram. As a result, the inverse Fourier transform of the spectral interferogram, or A-scan, is multiplied by a Gaussian-shaped "roll-off" factor:

$$I_d(k) \otimes e^{-\frac{4\ln(2)k^2}{\delta k}} \overset{\mathcal{F}T}{\leftrightarrow} I_d(\tilde{z}) \cdot e^{-(\tilde{z})^2 \frac{\delta k^2}{4\ln(2)}} \tag{2.29}$$

Here, the variable $\tilde{z} = 2z$ is substituted for the depth-doubling factor in FD-OCT and represents the processed A-line data to be compared directly to the sample structure. This exponential sensitivity roll-off factor of FD-OCT can be understood as the decrease in the fringe visibility at higher frequency interference, which corresponds to the large sample depth. The depth that corresponds to 6 dB, or 50%, sensitivity roll-off z_{6dB} is given as:

$$\tilde{z}_{6dB} = \frac{2\ln(2)}{\delta k} = \frac{\ln(2)}{\pi} \frac{{\lambda_0}^2}{\delta \lambda} \tag{2.30}$$

where the wavelength term is recognizable as one-half of the coherence length. It is also evident that a narrow spectral resolution results in longer coherence length as well as 6 dB imaging range.

The last constraint arises from the finite characteristic of the digital sampling. In SS-OCT, the sampling interval δk is limited by the acquisition speed of the digitizer while in SD-OCT, the sampling interval is limited by the physical size of the detector in the camera. Assuming the spectral interferogram is sampled into M spectral channels linearly spaced in k at the interval δk, the sampled wavenumber range is described as $\Delta k = M \cdot \delta k$. In the z-domain, the sampling interval is $\delta \tilde{z} = 2\pi/(2\Delta k)$, where the factor of 2 arises from the rescaled depth parameter $\tilde{z}$. The maximum depth samples are thus given by the Nyquist sampling requirement as:

$$z_{max} = \frac{M}{2} \cdot \delta \tilde{z} = \frac{\pi}{2 \cdot \Delta k} \tag{2.31}$$

It is evident from Eq. (2.29) that a finer sampling interval in the spectral interferogram allows for a larger potential maximum imaging range. However, the actual maximum imaging range of FD-OCT is a combination of all three factors.

2.5 OCT Implementation

2.5.1 Calibration

In FD-OCT, the spectral interferogram signal is converted from a k-domain to a z-domain using inverse Fourier transformation. To get an accurate sample reflectivity profile, the spectral interferogram must be sampled uniformly in wavenumber, or k-space. However, the tuning of a swept-source in SS-OCT is not always linear in k-space, and the non-linear sampling in the wavenumber will give rise to poor PSF with increasing sample depth [51]. To avoid this problem, one approach is to sample the detector signal at a nonlinear interval so that the resulting output signal is produced uniformly. In SS-OCT, swept-source lasers with a “k-clock” output combined with a digitizer with an external clock input can perform nonuniform sampling [52]. The “k-clock” is no more than an external Mach-Zehnder interferometer (MZI) implemented inside the swept-

source lasers to generate a dynamic calibration interference pattern. The external MZI generates a spectral interferogram with the frequency-dependent on the optical path length difference (Δz) of the two optical paths:

$$I_d[k] \approx \frac{\rho}{2}[S(k)(cos2k(\Delta z))] \tag{2.32}$$

Here, Eq. (2.32) can be considered as the detector signal of OCT when the two reflectors have the same reflectivity of 1, and the sample arm consists of a single reflector at a fixed position. It is evident that the resultant spectral interferogram is the source power spectrum modulated by a cosine function that oscillates as a function of wavenumber. The peaks, valleys, and zero-crossing points of Eq. (2.32) correspond to the equidistant spacing interval in k-space and can be used as a reference clock to sample the OCT interferogram linearly as a function of wavenumber.

However, the nonuniform sampling may not be an option due to either the laser, digitizer, or the type of imaging approach. An alternative calibration approach is to apply a calibration vector to the detected signal during the post-process. The detector output with a uniform time interval is acquired first, and then, this data is resampled to a uniform interval in k-space using interpretation based on the calibration vector. The calibration vector can be acquired by first sampling an interferogram with a fixed single-reflectance sample and reference reflector. Then a Hilbert transformation is applied to extract analytical phase information in the interferogram:

$$\varphi[t] \approx phase\big(H(I_d)(t)\big) = cos^{-1}[2(k[t])\Delta z] \tag{2.33}$$

This phase function is unwrapped to obtain $\varphi'[t]$ which describes the accumulative phase of the system as a function of discrete time. Inverting $\varphi'[t]$ and resampling for a uniformly spaced discrete phase yields t[φ] which is the calibration vector of time points that corresponds to the equidistant discrete spacing of wavenumber k. Resampling using this calibration vector with interpolation, such as a nearest neighbor method or a spline-based approach, can be performed. In

the case of SD-OCT, the same concept can be applied but the signal is sampled as a function of lateral position in the spectrometer instead of time, and thus, $\varphi[t]$ can be simply replaced with $\varphi[x]$. Given sufficient stability of the system, the calibration vector approach can remain valid for at least a few months.

2.5.2 Dispersion compensation

The use of a broad bandwidth light source increases the axial resolution of the OCT system. However, increasing the bandwidth of the laser also increases the dispersion that can deteriorate the axial PSF [53]. If all the distances were assumed to be in free space, the effects of chromatic dispersion can be ignored. In reality, however, both reference and sample arms contain materials with various indices of refraction, such as glass, optical fibers, air, and biological tissue. In this case, the light propagating through each arm will have a different wavelength-dependent refractive index (n[k]), which alters the propagation speed of the individual wavenumber of light. The effect of chromatic dispersion is cumulative with respect to the propagation distance in the media. However, as is evident in Eq. (2.9), only the OPL difference between the sample and the reference arm is preserved in OCT. Therefore, the amount of chromatic dispersion depends on the path length mismatch between the two arms in OCT. Typically, the difference in the path length is due to the residual unmatched fiber or the biological tissue placed in the sample arm. With proper dispersion compensation, we can obtain optimum axial resolution and avoid the reduction in fringe visibility. One approach is to physically insert a dispersion compensation element into the optical path of the reference arm. If the index profile of the system and the precise OPL differences are known, such as in the case of ocular imaging, a dispersive material, like glass or water, can be added to compensate for the dispersion.

Alternatively, the dispersion can be numerically compensated for by applying wavenumber-dependent dispersion correction coefficients to the spectral interferogram signal. The phase shift, $\varphi(k)$, from the dispersion present in a medium can be expanded as a Taylor series expansion around the center wavelength $k_0 = 2\pi/\lambda_0$ as

$$\varphi(k) = \varphi(k_0) + \frac{\partial\varphi(k_0)}{\partial k}(k - k_0) + \frac{1}{2!}\frac{\partial^2\varphi(k_0)}{\partial k^2}(k - k_0)^2 + \cdots \tag{2.34}$$

The zeroth-order and the first-order terms correspond to the phase offset and the phase velocity which does not contribute to the broadening in the PSF. The second-order term represents the group velocity delay (GVD) in the light and contributes to the broadening in the coherence function which leads to reduced fringe visibility and broadened reflective signals. It is important to note that the majority of dispersive broadening in OCT signals arises from the GVD; however, higher-order terms can also contribute to the decreased axial resolution. The dispersion broadening can be minimized by introducing the complex conjugate term, whose value is equal to third and higher-order dispersion, since it will cancel out the dispersion present in the system. Similar to the wavenumber calibration vector method, the spectral interferogram is first acquired from a single reflector such as a mirror surface. Then, a Hilbert transformation is performed to extract the phase described in Eq. (2.33). A polynomial fitting is applied to the unwrapped phase with a degree typically greater than 3, and the resultant coefficients equate to the amplitude of dispersion from the GVD and higher-order terms. Finally, the coefficient can be substituted into Eq. (2.34) with the first and the second term omitted to calculate the amount of phase required to compensate for dispersion [54].

2.5.3 Full-range imaging by phase shifting

In the previous section, it was established from Eq. (2.22) that the complex conjugate artifacts of FD-OCT effectively halves the imaging range due to the nature of Fourier transform operation. However, it is possible to separate the positive frequency component from the negative frequency conjugate artifact using techniques drawn from radio frequency signal processing [55]. Removing the mirror image will increase the imaging range of FD-OCT to cover the entire coherence length of the laser source. In the edge-emitting swept-source lasers, the coherence length is limited to typically 10 – 16 mm. By choosing an appropriate carrier frequency, one can separate the complex conjugate in positive and negative frequency terms. Mathematically, the introduction of the carrier frequency can be expressed by the additional phase modulation term $e^{-i\Delta ft}$). Typically, a phase modulator is introduced in the reference arm so the returning light from the reference can be expressed as:

$$E_r(k) = \frac{s(k)}{\sqrt{2}} r_r e^{i(2kz_r - 2\Delta ft)} \tag{2.35}$$

Here, the factor of 2 accounts for the double-pass of light through the phase modulator. Inserting Eq. (2.35) into Eq. (2.9) gives

$$\begin{aligned} I_D(k) = \frac{\rho}{4}\Bigg\{ & S(k) \cdot \left(R_r + \sum_{n=1}^{N} R_{sn} \right) + 2S(k) \\ & \cdot \sum_{n=1}^{N} \sqrt{R_r \cdot R_{sn}} (\cos\,[2k(z_r - z_{sn}) + 2\Delta ft]) \\ & + S(k) \cdot \sum_{n \neq m=1}^{N} \sqrt{R_{sn} \cdot R_{sm}} \big(cos2k(z_{sn} - z_{sm}) \big) \Bigg\} \end{aligned} \tag{2.36}$$

It is evident from Eq. (2.36) that the DC and auto-correlation terms are not affected by the carrier frequency and, thus, can be separated from the spectral interferogram signal. The amount of phase

shift needed can be estimated as a distance shift in the z space as $z_0 = \Delta f/m$. Assuming the linear spectral tuning of the laser as $k = k_0 - mt$, the cosinusoidal function of the cross-correlation term in Eq. (2.36) and its inverse Fourier transform can be expressed as:

$$\cos[2(k(z_r - z_{sn}) - \Delta f t)] = \cos[2(k(z_r - z_{sn} - z_0) + \frac{\Delta f k_0}{m})] \tag{2.37}$$

$$\xrightarrow{FT} \frac{1}{2}[\delta(z + \Delta z + z_0)e^{-\frac{\Delta f k_0}{m}} + \delta(z - \Delta z - z_0)e^{-\frac{\Delta f k_0}{m}}]$$

Here, $\Delta z = z_r - z_{sn}$ and m is the angular frequency of the laser source. Compared to the cross-correlation term in Eq. (2.9), the negative and positive terms of the inverse Fourier transformation are separated by an additional z_0. Therefore, the image can be constructed with only the positive or negative term by taking advantage of the entire coherence length of the laser.

2.6 Doppler OCT

Doppler OCT combines the Doppler principle with OCT to obtain high-resolution tomographic images of both static and moving constitutents in highly scattering tissues [38, 56]. When backscattering light from the moving particles interferes with the reference beam, a Doppler frequency shift Δf_Doccurs in the resulting spectral interference signal. The amount of Doppler frequency shift is proportional to the velocity of the particle movement (v), the angle of the sample beam with respect to the direction of the particle movement (θ), and the center wavelength of the light source (λ_0) [38, 56, 57]:

$$\Delta f_D = \frac{2v \cdot \cos(\theta)}{\lambda_0} \tag{2.38}$$

The factor of 2 arises from the fact that the Doppler shift is affected when the light incident upon the target as well as the light are back reflected.

The first *in vivo* two-dimensional Doppler OCT measurements were reported in 1997 [58, 59]. These early approaches utilized the spectrogram method based on either short-time Fourier transformation (STFFT) or wavelet transformation to determine the power spectrum of the measured fringe signal. Although spectrogram methods allow for simultaneous imaging of tissue structure and flow velocity, the velocity sensitivity is directly linked to both spatial resolution and imaging speed; increasing the velocity sensitivity will decrease spatial resolution and imaging speed. The minimum detectable Doppler frequency shift varies inversely with the STFFT window size which couples with the pixel acquisition time and frame rate. Moreover, spatial resolution is also proportional to the STFFT window size. This coupling between velocity sensitivity, spatial resolution, and imaging speed prevents the spectrogram method from achieving simultaneous high imaging speed, high resolution, and high-velocity measurement essential for measuring blood flow in small blood vessels where the flow velocity is low.

Phase-resolved Doppler OCT was developed to overcome those limitations [56]. This approach utilizes the phase change between the sequential A-line scans for velocity image reconstruction. In the phase-resolved Doppler OCT method, spatial resolution and velocity sensitivity is decoupled and the imaging speed can be increased by more than two orders of magnitude. In addition, since the time interval between successive A-line scans is much longer than the pixel time in STFFT, a much higher velocity sensitivity can be achieved using this approach. Mathematically, the Doppler frequency shift is obtained by measuring the phase difference between sequential A-line scans. The phase information of the fringe signal can be determined from the complex analytical signal at the j^{th} A-scan and depth of z as $A_{j,z}$. Then the Doppler frequency shift can be expressed as:

$$\Delta f_D = \frac{1}{2\pi}\frac{\Delta\phi}{\Delta T} = \frac{1}{2\pi \cdot \Delta T}[tan^{-1}\left(\frac{Im(A_{j+1,z})}{Re(A_{j+1,z})}\right) - tan^{-1}\left(\frac{Im(A_{j,z})}{Re(A_{j,z})}\right)] \quad (2.39)$$

where ΔT is the time interval between j[th] A-scan and (j+1)[th] A-scan. In TD-OCT systems, the complex analytical signal $A_{j,z}$ is determined through analytic continuation of the measured interference fringe function using a Hilbert transformation. In FD-OCT systems, the complex signal $A_{j,z}$ is obtained directly though the Fourier transformation of the acquired spectral interferogram.

Alternatively, the phase change can also be calculated by the cross-correlation of the sequential A-line scans as:

$$\Delta f_D = \frac{1}{2\pi \cdot \Delta T}\left[tan^{-1}\left(\frac{Re(A_{j+1,z}A_{j,z})}{Im(A_{j+1,z}A_{j,z})}\right)\right] \quad (2.40)$$

$$= \frac{1}{2\pi \cdot \Delta T}\left[tan^{-1}\left(\frac{Im(A_{j+1,z})Re(A_{j,z}) - Im(A_{j+1,z})Re(A_{j,z})}{Re(A_{j+1,z})Re(A_{j,z}) + Im(A_{j+1,z})Im(A_{j,z})}\right)\right]$$

Furthermore, it is demonstrated that averaging can be performed in both lateral and depth direction to further increase the SNR [60]:

$$\overline{\Delta f_D} = \frac{1}{2\pi \cdot \Delta T}[tan^{-1}\left(\frac{\sum_{j=1}^{M}\sum_{z=1}^{N} Re(A_{j+1,z}A_{j,z})}{\sum_{j=1}^{M}\sum_{z=1}^{N} Im(A_{j+1,z}A_{j,z})}\right) \quad (2.41)$$

where M is the number of A-lines that are averaged and N is the number of depth points that are averaged. In practice, the choice of M and N depends on the application; a larger M and N will increase the SNR with increased computation time and decreased resolution.

In addition to the Doppler shift, the variance of the Doppler frequency can also be used to map flow. Variations in flow velocity will broaden the Doppler frequency spectrum and result in a larger variance value (σ):

$$\sigma^2 = \frac{\int_{-\infty}^{\infty}(f-\bar{f})^2 P(f)df}{\int_{-\infty}^{\infty} P(f)\,df} \tag{2.42}$$

where $P(f)$ is the Doppler power spectrum and $\bar{f}$ is the centroid value of the Doppler frequency shift. Using the autocorrelation theory, the variance can be expressed as:

$$\sigma^2 = \frac{1}{(2\pi\cdot\Delta T)^2}\left[1 - \frac{\left|\sum_{j=1}^{M}\sum_{z=1}^{N}\left(A_{j+1,z}A_{j,z}^*\right)\right|}{\sum_{j=1}^{M}\sum_{z=1}^{N}\left(A_{j,z}A_{j,z}^*\right)}\right] \tag{2.43}$$

Doppler variance approach has the benefit of being less sensitive to the pulsatile nature of blood flow and the incidence angle which allows for better discrimination of transverse flow velocity [61]. In addition, it has been shown that the dynamic range of the flow velocity measurement in the variance approach can be as much as 10 – 20 times more than the corresponding phase-resolved method based on the Doppler angle [62].

Another related technique of the Doppler variance method is the intensity-based modified Doppler variance method [63]. In the phase-resolved Doppler variance in Eq. (2.43), the variance is acquired by the averaging of multiple correlation calculations in lateral and axial directions and is thus dependent on both the amplitude and phase terms of the complex OCT data. This Doppler variance obtained from Eq. (2.43) shows excellent results when the phase stability of the system is high. However, in a phase instable situation where there are phase jumping and jittering between A-lines, the acquired variance value will be affected greatly by the abrupt phase change. To overcome this limitation in a phase unstable situation, a modified averaging Doppler variance method removes the phase dependence and solely relies on the intensity values of the correlation data:

$$\sigma^2 = \frac{1}{(2\pi\cdot\Delta T)^2}\left[1 - \frac{\sum_{j=1}^{M}\sum_{z=1}^{N}\left|A_{j+1,z}A_{j,z}^*\right|}{\sum_{j=1}^{M}\sum_{z=1}^{N}\left(A_{j,z}A_{j,z}^*\right)}\right] \tag{2.44}$$

2.7 Summary

In this chapter, the principles of TD-OCT systems and FD-OCT systems have been discussed. For each approach, the axial resolution, lateral resolution, signal sensitivity, and imaging range have been presented. Several important implementation techniques for OCT system designs have been reviewed. Lastly, various Doppler OCT algorithms for the detection of motion were presented.

Chapter 3 –Image Segmentation Techniques for Airway OCT

3.1 Overview

Image segmentation is the commonly used digital processing technique in the field of medical imaging to convert a large set of digital data into a simple and easy-to-interpret format. In the context of OCT, image segmentation has been used to separate different tissue layers, remove noises and enhance the image, create a 3D model, and acquire quantitative analysis results needed for clinical assessment. Although various image segmentation techniques have been reported and evaluated for retinal OCT imaging, segmentation of airway images still relies mostly on manual segmentation. Furthermore, very few algorithms have been tested on airway OCT images with inhalation injuries. In this chapter, we present several image segmentation and quantification techniques for assessing the severity of airway inhalation. The accuracy of each algorithm was evaluated against manual segmentation.

3.2 Background and Motivation

In computer vision, image segmentation refers to the process of partitioning a digital image (e.g., OCT) into multiple segments. The purpose of image segmentation is to simplify the information by converting it into an easy-to-interpret format. It can be used to reduce noises, enhance the image, and reduce the amount of data by removing excess information and leaving only the region-of-interest (ROI). While image segmentation is an essential step for computer-aided diagnosis, the algorithms for segmentation are specific to imaging modality and application.

In airway OCT application, accurate segmentation will help clinicians to conduct large-scale early detection and monitoring of patients with airway injuries by providing quantitative

injury-related parameters, such as cross-sectional areas [12, 64], tissue layer thickness [65–67], and the amount of fluid accumulation [68]. Automated segmentation of OCT images, however, remains one of the most difficult steps in OCT image analysis. OCT images are typically contaminated with speckle noise since OCT forms an image using the interference of light [69]. Moreover, the intensity values of OCT decrease with imaging depth due to the absorption and scattering of light which makes it hard to resolve features in deep tissue. The illumination condition of the sample beam can impact the image quality as well since non-uniformity in the optical field or defocus during image acquisition can cause intensity inhomogeneity as well as broadening in the point spread function. In addition, endoscopic OCT imaging of an airway tissue poses its own challenges in terms of segmentation. First, various imaging artifacts are present since endoscopic OCT images are acquired by helical scanning of a fiber-optic catheter inside a protective plastic tube [**Figure 3.1 (a)]**. Strong back-reflection from the sheath surface may saturate the detector and create a vertical line artifact in the unwrapped OCT image. The sheath surface can also be visualized as a double-wall structure in the OCT image. Internal reflection in the fiber optic interface sometimes create a horizontal artifact in the unwrapped OCT images. Second, the curvature and the sharpness of the tissue surface can change depending on the position of the endoscopic probe with respect to the tissue. Third, the signal coming from the sheath can sometimes be indistinguishable if the tissue contacts the sheath, further adding difficulties to separate tissue from other artifacts [**Figure 3.1 (b)]**. All these artifacts and imaging features make it difficult to apply a single universal segmentation algorithm.

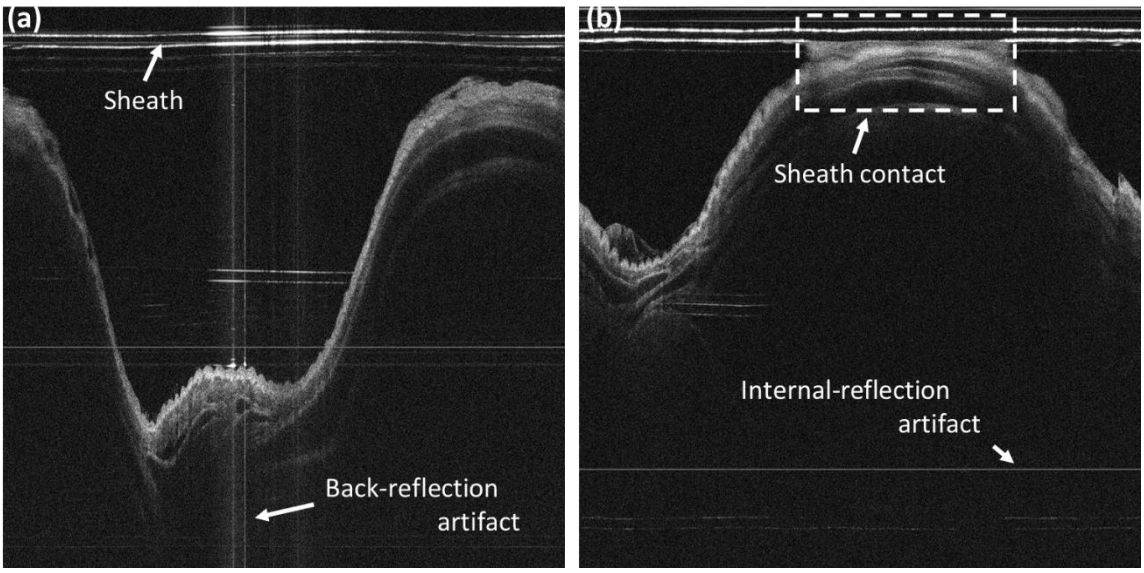

Figure 3.1 Typical imaging artifacts present in airway OCT images. (a) Strong back-reflection of the incident beam can saturate the photodetector and create vertical back-reflection artifacts and ghost images. (b) Edge blurring can be induced when the tissue is in contact with the sheath surface making it difficult to distinguish them apart. Internal reflection of the optics interface in the imaging probe shows up as a vertical line artifact in the image.

Several automated segmentation and analysis algorithms have been proposed to assist data interpretation of airway OCT images, such as a clustering algorithm [66, 70], morphological operation and thresholding [71], and the shortest path [19]. However, those methods are not robust enough to handle speckle noise and quality degraded images. In addition, the airway wall thickness measurement from those intensity-based segmentation methods often depends on the signal attenuation in the OCT image. Li *et al.* have proposed a robust segmentation method based on a dynamic programming (DP) algorithm to delineate boundaries of airway regions [65]. The major strength of the dynamic programming algorithm is that it can preserve the continuity of the boundary which means it is less susceptible to noises and outliers. Compared to other graph-based edge detection algorithms, the DP method is an efficient graph solving method that has quadratic time complexity. The algorithm can further be extended to a 3D graph search of airway data [72]. Another promising segmentation approach for OCT is deep learning, or convolutional neural

network (CNN) to be more specific, which is a growing field in image processing and image recognition thanks to the recent technological breakthroughs in computational power. Deep learning has been applied to retinal OCT imaging to diagnose and segment features of diabetic retinopathy [73, 74], age-related macular degeneration [75, 76], and glaucoma [77, 78] with comparable or superior results. However, at the time of writing, to our best knowledge no deep learning segmentation algorithm on airway OCT images have been reported. In this study, we propose to apply DP segmentation and CNN segmentation on endoscopic OCT images for quantitative assessment of airway injuries.

3.3 Methods

3.3.1 Image acquisition and display in airway OCT

To discuss the segmentation approaches for airway OCT images, we must first understand how the OCT images are acquired in the airway. In airway studies, most OCT imaging systems are based on a swept-source laser and catheter-type fiber optic-based imaging probe, as illustrated in **Figure 3.2**. Swept-source laser has the high imaging speed and long imaging range. Catheter-type fiber optic-based imaging probe has flexibility to image complex airway structure and can be combined with a clinical bronchoscope. The catheter imaging probe is accompanied by either an external rotational unit, such as a fiber optic rotary joint or an internal rotational unit such as a micromotor, to perform a rotational scan of the targeted lumen (**Figure 3.3**). In addition, most imaging systems are equipped with a linear pullback motorized stage to perform a 3-dimensional scan in depth, radial, and longitudinal directions. As described in the previous section, earlier design of the long-range OCT system utilizes a phase modulator, such as an acousto-optic modulator, to extend the imaging range by eliminating complex conjugate artifacts [26].

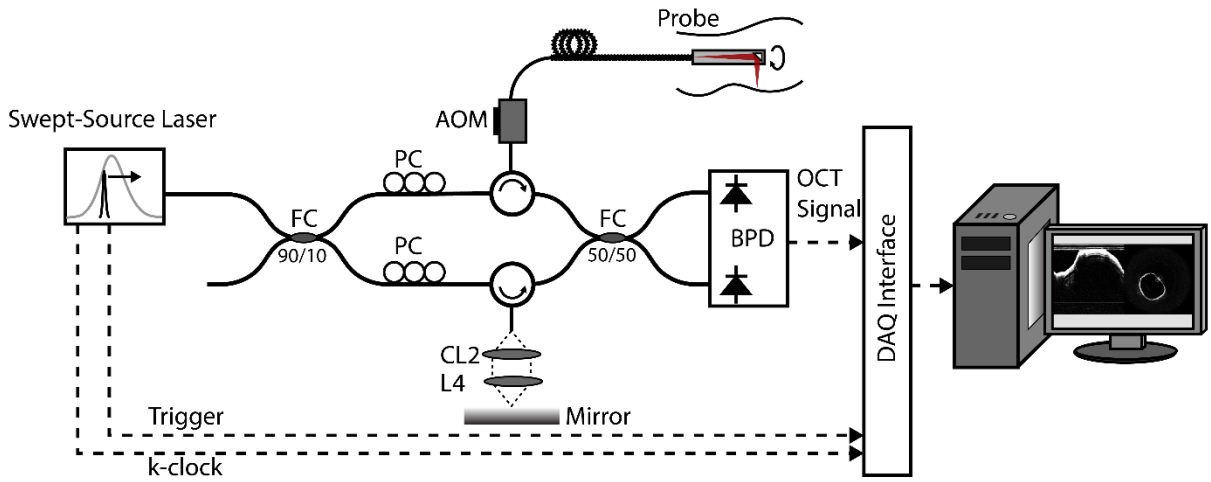

Figure 3.2 Schematics of a typical system setup for airway OCT imaging based on a Mach-Zehnder interferometer. FC: fiber coupler, L: lens, PC: polarization controller, BPD: balanced photodetector, AOM: acousto-optic modulator.

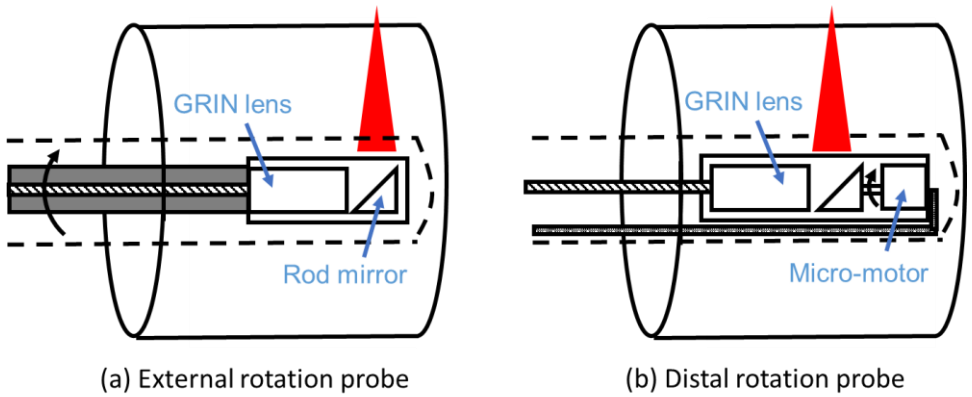

Figure 3.3 Two types of endoscopic OCT probes for airway imaging. (a) In the external rotational scheme, probe scanning is driven by an external motor. (b) In a distal rotational probe, probe scanning is driven by the rotation of the integrated micro-motor. Gradient index (GRIN) lens focuses the OCT light from the optical fiber to the sample.

Once the raw spectral interferogram data sets are acquired, they are converted to logarithm depth-resolved intensity values using the Fourier transformation described in section 2. Here, the number of A-scans needed to reconstruct a single airway cross-section image can be precisely determined from the laser scanning rate and the rotation speed of the imaging probe. All the airway cross-section images are initially displayed as a polar coordinate system where the vertical axis represents imaging depth and the horizontal axis represents angular component [**Figure 3.4 (a)]**.

Here, the structure of the porcine airway wall, including the mucosa, submucosa, and cartilage, can be identified. The polar OCT images can eventually be converted to a Cartesian coordinate using interpolation to get an accurate representation of the airway geometry [**Fig. 3.4 (b)]**. Nonetheless, most segmentation algorithms use the polar image as data input since they can be considered as a layer segmentation problem, similar to the segmentation problem in retinal OCT.

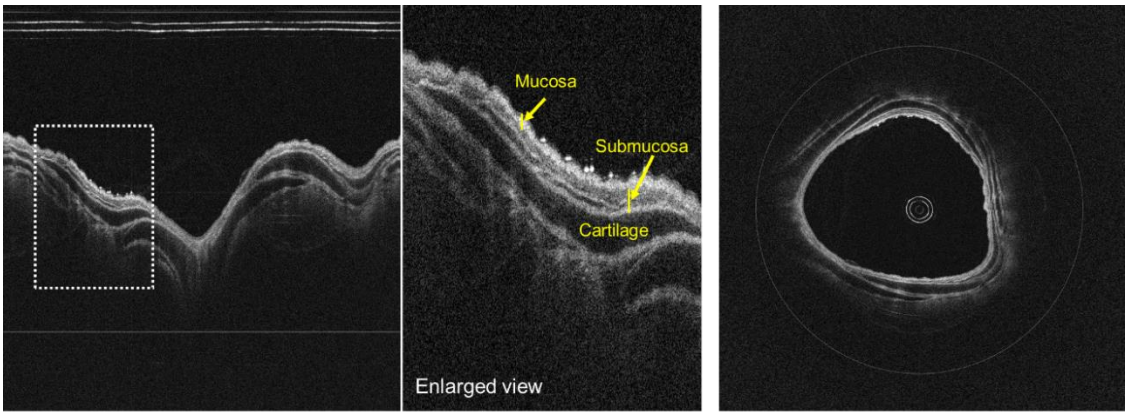

Figure 3.4 Same airway OCT image displayed in two coordinate systems. (a) Polar coordinate and (b) Cartesian coordinate.

3.3.2 Dynamic programming segmentation

Dynamic Programming (DP), first introduced by Richard Bellman in the 1940s, is a widely-used image processing technique based on graph theory to solve minimization problems in a simple and effective way. In computer vision, the DP algorithm has found widespread applications from calculating the shortest path in computer gaming to detecting roads and other features in satellite images. In biomedical applications, the DP algorithm has been applied in the processing of medical imaging to delineate contours, lines, and boundaries of organs, bones, vessels, and cells. The DP algorithm has successfully been applied in some OCT applications, both in research and in the clinic, including delineating retinal layers [79–82] and the thickness measurement of cornea [83].

Generally, DP-based segmentation of airway OCT images can be separated into three parts: pre-processing, path searching using DP algorithm, and quantification. The pre-processing mainly comprises of denoising and binarization of the original intensity image to identify the prominent airway tissue region in the image. In the path searching step, tissue boundaries and edges are localized by solving a minimization problem using the DP algorithm. Finally, the segmented areas are converted to a quantitative value, such as thickness or a 3D representation, of the airway anatomical structure. In the following, we will detail each step of the airway segmentation.

Pre-processing

In most segmentation methods, a series of low-level operations are used on the input images to reduce background and other artifacts before performing the segmentation. This will improve the accuracy of the segmentation and can sometimes reduce the computational load. As mentioned in section 3.2, the OCT images are contaminated by multiple defects, including speckle noise, signal saturation artifacts, and ghost objects produced from internal interference of the optics. To reduce those imaging artifacts, a series of low-level operations can be applied:

1) Speckle noise suppression - 2D median filter with an appropriate kernel size can reduce random noise while maintaining the edge features.
2) Vertical line artifacts reduction - the mean intensity of each A-scan is subtracted from each pixel in the same line to suppress vertical line artifacts caused by the saturation in the detector [**Figure 3.5 (b)]**.
3) Horizontal noise reduction – morphological dilation and erosion operation with a vertical structure element is applied to the image to reduce the thin horizontal noise such as sheath artifacts. This operation can also be performed after creating a binary image in the next step.

4) Thresholding and area filtering – position and shape of airway structure in the image can be somewhat extracted by applying thresholding using a user-defined threshold value [**Figure 3.5 (c)]**. Once the binary image is created, any connected region with the pixel number smaller than a certain value is removed. This will only leave the regions that could potentially be considered as the airway structure and remove any small artifacts. Then, dilation and bridging operation are applied to connect some of the airway features that may be separated due to the low image contrast [**Figure 3.5 (d)]**. At this point, the region with the largest area can be considered as the area of the image that contains airway structure, and thus, all the other pixels are removed from the input OCT images to obtain a cleaner noise-reduced image.

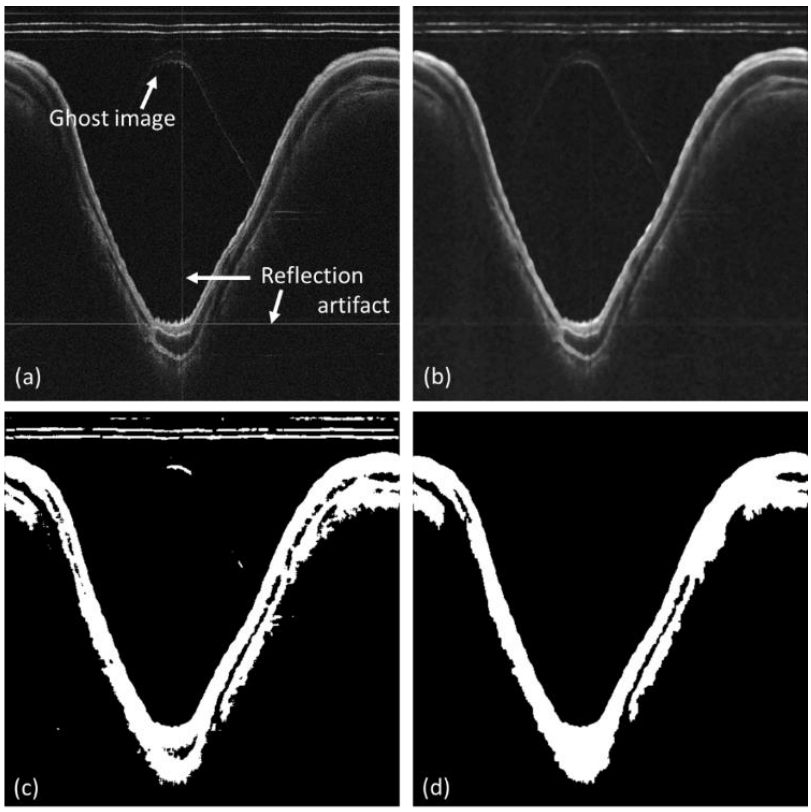

Figure 3.5 Pre-processing for DP segmentation (a) Raw OCT data after (b) A-line normalization and median filter, (c) binary thresholding, and (d) area filtering.

Shortest path searching based on dynamic programming

Finding edge features in an image can be considered as solving energy minimization tasks in graph theory. Graph is defined as a structure that contains nodes connected by edges. A path in a graph is a connection of several nodes via edges, which can be associated with a specific weight, known as cost. The solution to the energy minimization problem is known as the shortest path, which is a path with the lowest cost in a graph. Dynamic programming has proven to be an efficient method to solve this "shortest path problem" since it sequentially solves the original problem by splitting it into simpler subproblems. Here, the principle of the shortest path problem by DP algorithm is reviewed briefly using the single-source shortest path problem as an example (**Figure 3.6**).

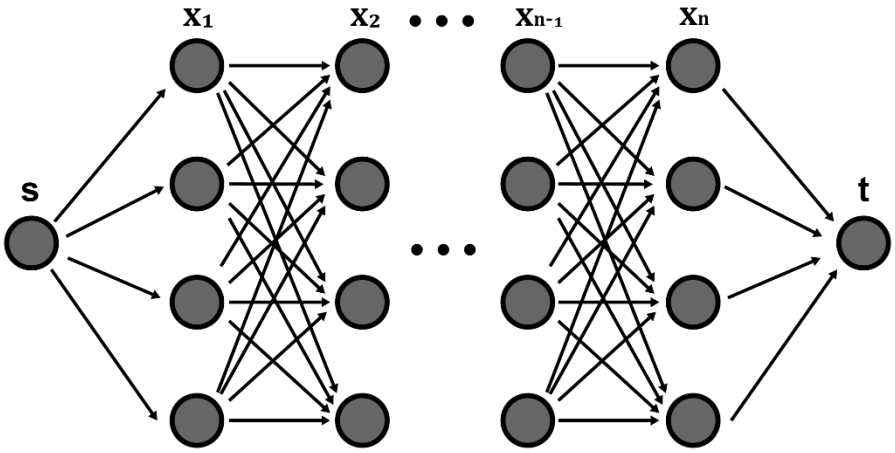

Figure 3.6 Single-source shortest path problem with possible path (x1,x2,….xn) from node s to node e.

The DP algorithm sequentially evaluates the shortest paths starting at node s and at each state i = 1 …n until the last node t. Due to this sequential nature of the algorithm, it can only find the shortest paths from one side of the graph to the other side, known as a directed acyclic graph (DAG), which prevents looping. In a discrete energy minimization problem like this, the

cumulative energy can be considered as the summation of energy based on observations in the underlying data and prior energy:

$$E_{total} = E_{data} + E_{prior} \tag{3.1}$$

Let x_i | i=1,2,….n be an arbitrary path of n element in the graph in **Figure 3.6**, the combination of optimal path is obtained by minimizing E. Furthermore, the energy at any given state can be estimated from the sum of the proceeding energy and the current cost as:

$$E(\, x_1, x_2, \ldots\, x_i) = E(\, x_1, x_2, \ldots\, x_{i-1}) + c(x_i) + d(x_{i-1}, x_i) \tag{3.2}$$

Here, $c(x_i)$ is the cost of the path passing through x_i, and $d(x_{i-1}, x_i)$ is the cost of the partial path between $x_{i-1}\ and\ x_i$. For example, $c(x_i)$ can be a feature in the image, such as pixel intensity value, and $d(x_{i-1}, x_i)$ is a geometrical cost where specific neighborhoods can be penalized in terms of their position (e.g., the connectivity of the neighboring pixels and the boundary conditions). Now, energy minimization by the DP algorithm can be performed with the following recursive formula:

$$C_1(x_1) = c(x_1) \tag{3.3}$$

$$C_i(x_i) = c(x_i) + \min_{x_{i-1}}(C_{i-1}(x_{i-1}) + d(x_{i-1}, x_i)) \tag{3.4}$$

where C_i is cumulative cost of the shortest path from x_i back to the beginning of the graph. Therefore, by evaluating the minimum of the cumulative cost at last column C_n, one can find the starting point of the global shortest path x_n^* that minimizes the energy. From x_n^* , one can trace back the global shortest path through the entire graph from state n back to state 1 by following:

$$x_1 = \arg\min_{x_1}(C_1\ (x_1\ ) + \mathrm{d}(x_1, x_{i+1}^*\ )\ ) \tag{3.5}$$

The OCT image can be regarded as an $m \times n$ image matrix and thus can be seen as a graph, where the neighboring pixels are connected. Therefore, **Figure 3.6** can be simplified to having each node connected to three predecessors. The number of possible starting points is equal

to the number of rows of the image matrix. The tissue edge in the segmentation can be obtained as a result of finding the shortest path traversing the image from left to right, where it passes each column of the image exactly once. The graph construction step, where the DP algorithm solves the shortest path problem in the $m \times n$ image matrix, is described as follows:

Algorithm 3.1 Solving the shortest path problem using DP algorithm

```
for node j =1,2,...,m at first column do
    C1,j [x1,j] ← E [x1,j]
end
for node i =2,3,...,n
    for node j =1,2,...,m at column do
        Ci,j [xi,j] ← min_{xi-1,k} (E(xi-1,k , xi,k) + Ci-1 [xi-1,k])      where k = j-1, j, j+1
    end
end
```

Here, k is determined by the number of possible connections from pixel-node $x_{i,j}$ to its neighboring pixel-nodes in the previous column x_{i-1}: three connected neighbors ($k = j - 1, j, j + 1$) in our case. The recursive graph construction formula in Eq. (3.3) and Eq. (3.4) can also be described as

$$C_1(x_{1,j}) = 0 \qquad \text{, where } j = 1,2, \dots m \tag{3.6}$$

$$C_i(x_{i,j}) = min\begin{bmatrix} \alpha \cdot E(x_{i-1,j+1}, x_{i,j}) + C(x_{i-1,j+1}) \\ E(x_{i-1,j}, x_{i,j}) + C(x_{i-1,j}) \\ \alpha \cdot E(x_{i-1,j-1}, x_{i,j}) + C(x_{i-1,j-1}) \end{bmatrix} = min\begin{bmatrix} Cost_1 \\ Cost_2 \\ Cost_3 \end{bmatrix} \tag{3.7}$$

where α is a weight factor and $Cost_1, Cost_2, Cost_3$ are the cumulative costs of picking the three possible neighboring paths. E is energy of partial path from x_{i-1} to x_i and defined as

$$E\big(I(x_{i,j}), I(x_{i2,j2})\big) = 2 \cdot \max(I) - I(x_{i,j}) - I(x_{i2,j2}) \tag{3.8}$$

where I($x_{i,j}$) is the pixel intensity at the pixel-node position $x_{i,j}$. The inverse operation is needed in terms of the energy minimization problem. This energy minimization function is based on the fact that the edge features in the OCT image are likely to have multiple connected pixels with similarly high-intensity pixel values. Intuitively, calculating the cost function at each node can be considered as measuring similarity against the three neighbor pixels on the left.

Graph construction is followed by recursive path searching. While getting the cost for each path, another parameter is recorded simultaneously to log the possible solutions for getting the shortest path:

$$Path(I_{i,j}) = \begin{cases} j+1, if\ C = Cost1 \\ j, if\ C = Cost2 \\ j-1, if\ C = Cost3 \end{cases} \quad (3.9)$$

The path value in each node indicates the solution to the local shortest path problem. Similar to the single-source shortest path problem, the starting point of the global shortest path is the pixel-node with the minimum cumulative cost in the last column x_n. Then, the global shortest path can be traced back to the first column by simply retrieving the local shortest path information recorded by the $Path(I_{i,j})$ function recursively (**Figure 3.7**).

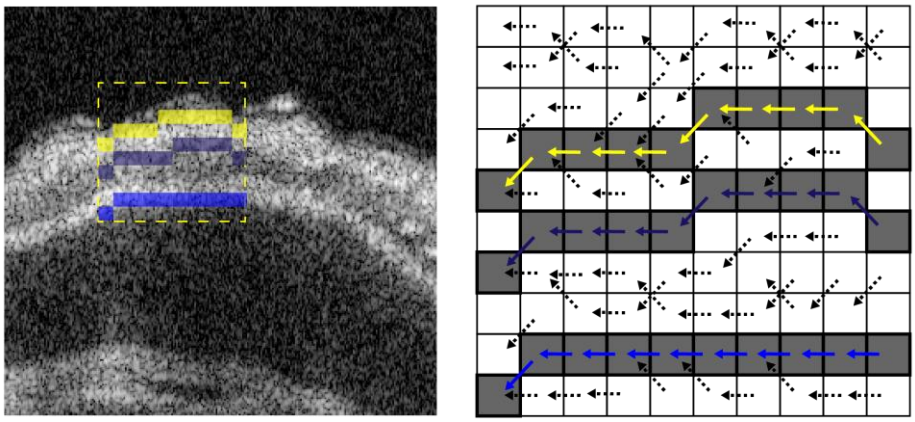

Figure 3.7 Dynamic Programming principle. Costs are estimated from the intensity of neighboring pixels. Path with minimum costs is back propagated.

In order to maintain the closeness of the counter when converting to the Cartesian coordinate, the shortest path has to meet at the same position or within the neighborhood at both ends. To apply this constraint, we applied the image patching algorithm to the input image where the image size is extended by copying a patch. For example, a specified number of columns on the left is patched to the right side of the image and vice versa. It is important to note that the image patching algorithm attracts a circular contour but does not guarantee closeness.

In our case, the input image of the DP shortest path problem is the gradient magnitude of the original intensity image in order to emphasize the edges:

$$I_{i,j} = -||\nabla f(x_{i,j})|| \tag{4.0}$$

Quantification of airway parameters

Image segmentation can help quantify various airway parameters from the raw OCT data, including the lumen cross-sectional area [12, 64], tissue layer thickness [65–67], amount of fluid accumulation [68], and reconstruction of a three-dimensional anatomical structure [25, 84]. Here, we will discuss the DP-based quantification steps for two airway parameters most relevant to airway inhalation injuries: tissue layer thickness and cross-sectional areas.

The estimation of the cross-sectional area and volume follows these steps. Once the surface of the tissue lumen is identified using the DP shortest path search in each polar OCT image, binary images are created to highlight the intraluminal space. The back-and-white (BW) images of the lumen are then converted to the Cartesian coordinate using interpolation to represent the actual airway structure. Finally, the BW image stack is interpolated based on the correct inter-frame distance to display a three-dimensional airway model.

Segmentation and quantification of the tissue layer start with identifying the tissue lumen surface as well. However, the DP-based path searching is performed repeatedly to find multiple

surfaces (**Figure 3.8**). To reduce the computational load and limit the search area, we adopted the flattening method after the initial search to identify the lumen. We simply flattened the image according to the segmented lumen boundaries which reduces the curvature in the tissue features as well as shifts all the relevant tissue information to one side of the image. Then, a specific number of rows below the lumen boundaries are cropped out to limit the range of searching for other boundaries, including the mucosa and submucosa surface. After flattening, the tissue boundaries of the mucosa and submucosa are searched separately using the slope-constraint graph search method where the weight factor in Eq. (3.7) is set to less than 1. Since the flattening method does not require interpolation, segmentation accuracy can be maintained. Finally, once all the tissue boundaries are delineated, the thickness of the tissue is calculated by simply counting the number of pixels between each layer in the vertical direction. Alternatively, the area between each layer can be used to indicate the tissue thickness.

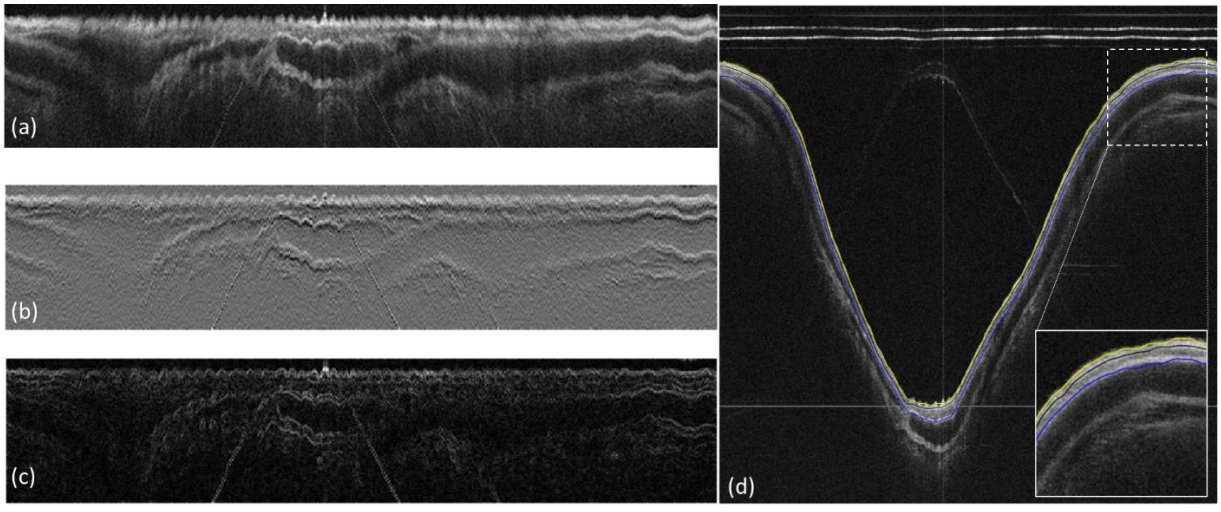

Figure 3.8 Multi-layer tissue segmentation. (a) Flattened image based on the lumen surface detection, (b) gradient image, (c) gradient amplitude, and (d) DP segmentation of lumen (yellow), mucosa-submucosa (purple), and submucosa-cartilage (blue) boundaries.

3.3.3 Deep learning segmentation

Constructing the convolutional neural network

Convolutional neural network (CNN) is the most widely used deep learning architecture in image segmentation. CNN takes in an image as input and has a three-dimensional arrangement of neurons that connect with the small region of preceding layers as shown in **Figure 3.9 (a)**. CNN is typically comprised of a combination of convolutional layers and non-linear activation layers, such as rectified linear unit (ReLu) function, pooling layers, and fully-connected layers. The convolution layer applies a convolution filter to the input matrix to obtain volumes of feature maps containing features extracted from each filter. The non-linear activation layer applies a non-linear function such as $y = max(0, x)$ to the input values to increase non-linearity and improve the training speed. The pooling layer down-samples the input matrix to reduce the spatial dimensionality which will reduce the computational cost and prevent overfitting. A fully connected layer is the layer where all the inputs are connected to every activation unit of the next layer and are typically used in the last layer of CNN to form the final output. CNN is commonly used in a classification problem. In order to use CNN for semantic segmentation, one can divide an input image into smaller patches by utilizing a sliding window and classify the center pixel of the patch before sliding the window forward [85]. However, such an approach is inefficient as the overlapping features of the sliding window are not re-used. To overcome this limitation, a fully-convolutional network (FCN) was proposed in which the final fully connected layers were replaced with a series of transposed convolutional layers as shown in **Figure 3.9 (b)**. The transposed convolutional layers, also known as the decoder, applied up-sampling to the low-dimensional feature maps to recover the original spatial dimension while simultaneously performing semantic segmentation. U-Net, which is the FCN developed for biomedical imaging applications, is one of

the most commonly used neural network architecture for OCT segmentation [86]. The most distinctive feature of U-net is the skip connections between the contraction layers and the expansion layers which are used to share localization information by directing concatenation on some of the contraction layers to the expansion layers of the same size. Compared to the simple FCN, U-net can maintain the sharp edges in the segmented image since the skip connections preserve the spatial information of the input image.

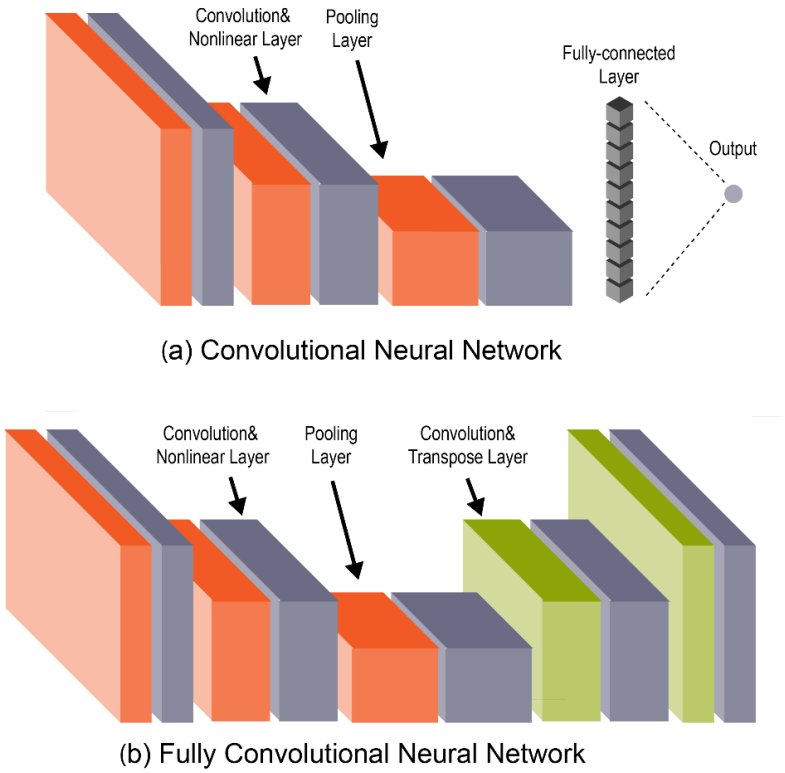

Figure 3.9 Example of neural network for image classification and segmentation. (a) Convolution neural network, typically comprised of a combination of convolution layers, non-linear activation layers, pooling layers, and fully connected layers. (b) Fully convolutional neural network comprised of a combination of convolutional layers. non-linear activation layers, pooling layers, and transposed convolutional layers.

Implementing the convolutional neural network

To implement CNN for the image segmentation problem, the neural network can be trained using, typically, a large labeled data set. However, it can be time-intensive to build and train the

network from scratch. Alternatively, one can use a deep learning approach called transfer learning where the network incorporates an existing pre-trained network such as AlexNet. The typical process of transfer learning is to remove the last layer of the pre-trained network and replace it with task-specific layer(s). This allows the network to utilize the low-level features learned from millions of images to extract task-specific features in the last layer in order to perform the classification /segmentation of new images. The main advantage of using transfer learning is the reduced computational cost for the training since only a small number of weights have to be optimized. Another typical challenge with the convolutional neural network in biomedical imaging is that gathering a large number of labeled data in medical imaging can sometimes be impractical. Since the performance of the neural network is dependent on having sufficient training data, it can lead to underfitting or overfitting. To overcome this, data argumentation techniques can be used to increase the training data sets in the absence of real data. Data argumentation creates additional data sets from the available existing data by applying class preserving transformation including, but not limited to, the following operations [87]:

1) Transformation – shift the image in the horizontal or the vertical direction while preserving the image size.
2) Rotation – rotate the image in the clock or counter-clock direction.
3) Mirroring – horizontal or vertical flip by reversing the pixel position in columns or rows.
4) Scaling – zoom in or out of the image by interpolation. In the case of scaling down, boundary pixels are added to maintain the same image size.
5) Contrast adjustment – adjusting the histogram to train the network to account for the intensity variation in the test images.

6) Image stretching – scaling the image differently in one direction compared to the other.
7) Shearing – stretching the image in the diagonal direction.
8) Elastic deformation – apply scale normalized random deformation field to the image.

In all cases, the image size is maintained to the one in the original data by using nearest-neighbor fill, duplication, averaging, and interpolation. The primary function of the data augmentation is to increase the generalization of the data and prevent underfitting or overfitting. Data augmentation can effectively increase the number of training data and overcome the shortage of available data; however, heavy use of augmentation can generate features that are not realistic. In addition, it is important to note that data augmentation cannot account for all the variations occurring in the training data. Neural networks are typically trained through an optimization algorithm in which the network weights are updated though back-propagation based on the gradient of a loss function. The loss function is obtained by comparing the predicted outcome from the "ground truth" (e.g., manual annotation).

Evaluating the convolutional neural network

Once the neural network is trained, the model needs to be evaluated by performance metrics in order to assure the high segmentation accuracy. The selection of an appropriate evaluation metric depends on the many factors; however, the most commonly used performance metrics are listed below.

1) Accuracy – the percentage of image pixels that are classified correctly. Accuracy is the most basic evaluation metric but has limitations to misrepresent image segmentation performance in the case of class imbalance. Class imbalance occurs when one segmentation class dominates others. In the case of class imbalance, the high segmentation accuracy of the dominant class will affect the accuracy of the other classes.

$$Accuracy = \frac{Correctly\ Predicted\ Pixels}{Total\ number\ of\ Image\ Pixels} = \frac{TP + TN}{TP + FP + FN + TN}$$

2) Prevision – the proportion of the pixels in the automated segmentation results that match with the group truth. Prevision is sensitive to over-segmentation as it will result in low precision scores.

$$Precision = \frac{Correctly\ Predicted\ Positive\ Pixels}{Total\ number\ of\ Predicted\ Pixels} = \frac{TP}{TP + FP}$$

3) Recall – the proportion of the positive pixels in the ground truth that were correctly identified through automated segmentation. Recall is sensitive to under-segmentation as it will result in low recall scores.

$$Recall = \frac{Correctly\ Predicted\ Positive\ Pixels}{Total\ number\ of\ Positive\ Pixels} = \frac{TP}{TP + FN}$$

4) Dice similarity coefficient (DSC) – the harmonic mean of precision and recall which considers both the false alarm and the missed values in each class. High DSC score means the predicted segmentation regions match with the ground truth both in terms of location and the level of details.

$$DSC = \frac{2\,|A_{Ground\ Truth} \cap A_{CNN}|}{|A_{Ground\ Truth}| + |A_{CNN}|} = \frac{2 \times TP}{2 \times TP + FP + FN}$$

where *A* is the segmented area.

5) Intersection-over-Union (IoU) – the ratio of the area of the overlap between the predicted segmentation and the ground truth to the area of the union of the two. Although correlated to DSC, IoU penalizes incorrect labeling more than the DSC.

$$IoU = \frac{A_{Ground\ Truth} \cap A_{CNN}}{A_{Ground\ Truth} \cup A_{CNN}} = \frac{TP}{TP + FP + FN}$$

3.4 Results and Discussion

3.4.1 Evaluation of the DP segmentation in healthy airway

In order to evaluate the accuracy of the DP segmentation on the airway data set, manual segmentation was performed on the same data set. The airway data set consisted of more than 200 OCT cross-section images from a post-mortem rat trachea, which corresponded to the anatomical location between epiglottis and carina. The manual segmentation was conducted on the same OCT data set using 3D Slicer (Version 4.6 available from https://www.slicer.org/)[88, 89]. Two readers, without prior knowledge of the automated 3D segmentation results, were recruited to manually trace out the lumen boundary.

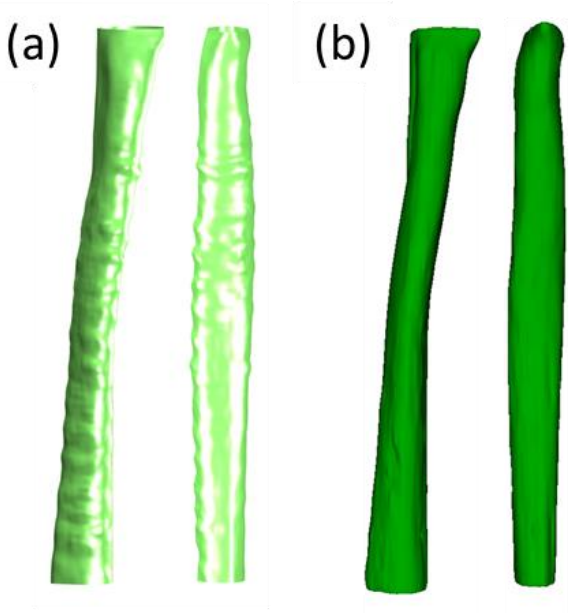

Figure 3.10 3D reconstruction of healthy rat trachea using (a) automated and (b) manual segmentation. Normal rat trachea has a relatively uniform diameter with a tubular structure in both the automated and manual reconstructions. The epiglottis opening can be located at the top of the reconstructed trachea.

It is evident from the comparison of the two 3D airway models that the DP segmentation provides similar results to the manual annotation in terms of airway structure (**Figure 3.10**). While the automated airway models show a ribbed structure where the cartilage rings are present, the manual models have a smooth surface throughout the trachea. This indicates that the accuracy of

the DP algorithm to segment airway structure is comparable or even superior to the human reader. Bland-Altman plots of healthy airway segmentation show that there is very little bias (<5%), indicating good correlation between manual and automated segmentation results (**Figure 3.11**).

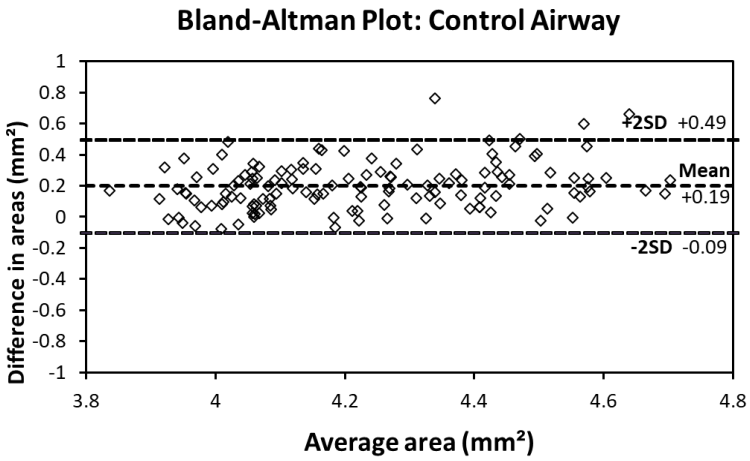

Figure 3.11 Bland-Altman plots of healthy airway segmentation. 95% limits of agreement and bias versus the mean are shown by dashed lines.

3.4.2 Evaluation of the DP segmentation in obstructed airway

Next, the accuracy of DP segmentation was evaluated on the obstructive airway data obtained from a methyl-isocyanate (MIC) inhaled rat trachea (**Fig. 3.12**). Generally, accurate segmentation of an obstructive airway is substantially more challenging compared to a healthy one due to the structural complexity and the "noise" present in the image, including secretion and tissue debris. This can also be evident from the large variance in the cross-sectional area resulting from the narrowing and variability of injury within the airway due to the effects of the toxic gas exposure. Similar to the health airway, the DP algorithm provided similar segmentation results to the manually traced airway. The unique structures due to the cartilage rings are visible only in the automated segmentation, indicating the senitivity and accuracy of the segmentation compared to the human reader.

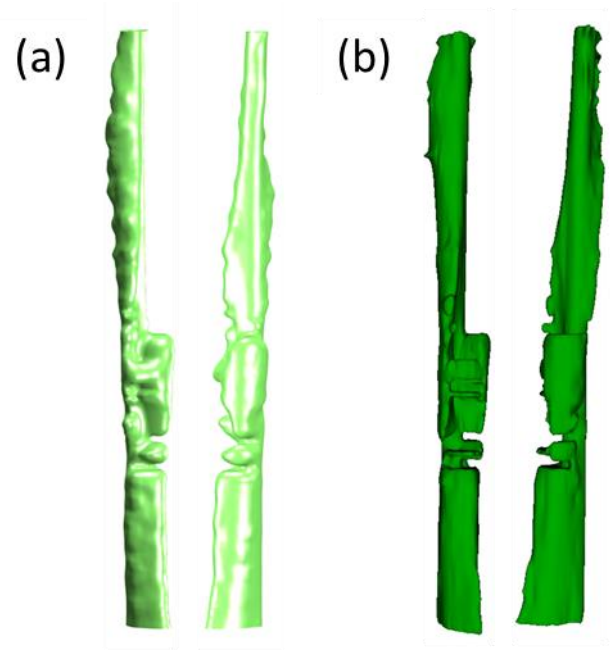

Figure 3.12 3D reconstruction of MIC-exposed rat trachea using (a) automated and (b) manual segmentation.

From the Bland-Altman plot of the obstructive airway data **(Figure 3.13)**, it is evident that the automated segmentation provides conservative estimates of the luminal area in the "noisy" region, and it occasionally estimates the cross-sectional area to be smaller than the actual area due to airway edema and luminal debris that are scattered within the trachea. The automated segmentation of the upper trachea in the MIC sample, where the airway is severely obstructed and "noisy," indicates a lower mean cross-sectional area than the manual results despite that manual tracing tends to give smaller estimates in the normal regions. This may be desirable in some cases since the tissue debris and fluid accumulation substantially compromise the airway function and cause airflow obstruction. However, the automated segmentation algorithm can be calibrated as well so that it covers a larger region and provides a more accurate assessment of only the intraluminal cross-section areas. Additionally, artificial neural networks can be implemented to better differentiate the difference between the lumen wall and the fluid and/or debris that are situated inside the airway. Furthermore, in some cases, additional "lumens" or "false lumens" are

created by separation and/or sloughing of tracheal tissue layers. The degree to which these lumens conduct airflow is likely to be variable. The automation algorithms can also be modified to map the secondary lumens if clinically useful.

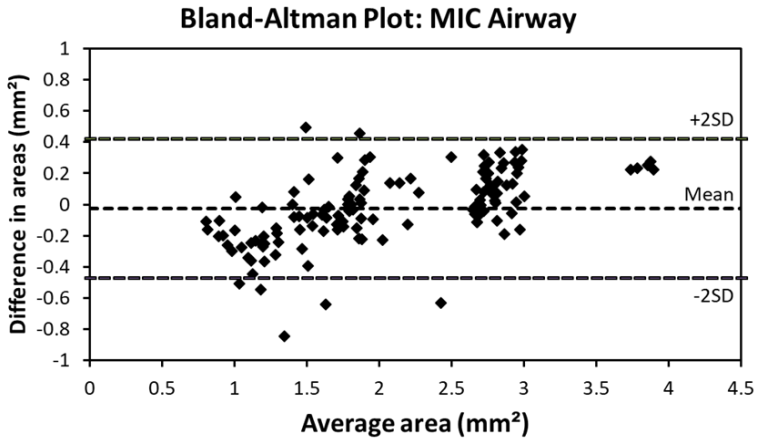

Figure 3.13 Bland-Altman plots of the MIC airway segmentation show that there is very little bias (<5%), indicating good correlation between manual and automated segmentation results; 95% limits of agreement and bias versus the mean are shown by dashed lines.

3.5 Summary

We propose that automated segmentation may outperform manual tracing, especially when handling large data sets, since it will not be subject to intra- and inter-reader variation and will significantly decrease the processing time.

Chapter 4 – ACUTE OBSTRUCTIVE AIRWAY IN METHYL ISOCYANATE-INHALED RAT MODEL REVEALED BY MINIATURE OCT ENDOSCOPE

4.1 Overview

Development of effective rescue countermeasures for toxic inhalational industrial chemicals, such as methyl isocyanate (MIC), has been an emerging interest. Nonetheless, current methods for studying toxin-induced airway injuries are limited by cost, labor time, or accuracy, and only provide indirect or localized information. OCT endoscopic probes have previously been used to visualize the 3-D airway structure. However, gathering such information in small animal models, such as rat airways after toxic gas exposure, remains a challenge due to the required probe size necessary for accessing the small, narrow and partially obstructed tracheas. In this study, we have designed a 0.4 mm miniature endoscopic probe and investigated the structural changes in rat trachea after MIC inhalation. An automated 3D segmentation algorithm based on graph theory was implemented so that anatomical changes, such as tracheal lumen volume and cross-sectional areas, could be quantified. The tracheal region of rats exposed to MIC by inhalation showed significant airway narrowing, especially within the upper trachea, as a result of epithelial detachment and extravascular coagulation within the airway.

4.2 Background and Motivation

The development of effective countermeasures to inhalation poisoning by industrial chemicals has been of great interest for several decades. Industrial chemicals, such as methyl

isocyanate (MIC), are inexpensive and easy to manufacture, but they can inflict massive damage if released intentionally as an act of terror, or from large-scale accidents or natural disasters, as was the case in the Bhopal disaster [90]. Airways are especially sensitive to vesicants like MIC, as MIC inhalation can acutely cause airway inflammation and obstruction, pulmonary edema, and death [91, 92]. If the victim survives, airway hyperresponsiveness, reactive airway dysfunction syndrome, and/or asthma can occur. Current efforts to develop new therapeutic agents and approaches for MIC rely on animal studies with chemical and structural analysis of MIC-induced damage [93], *in vitro* testing [92], histological examination, and arterial blood gas analysis in these models [94, 95]. However, anatomical changes in the airway structure during and after exposure to MIC gas have not been directly recorded.

The ability to optimally assess responses to therapeutic interventions necessitates development of efficient, accurate, and quantitative methods for determining airway injury. MRI and CT have been used to visualize airway structure [96, 97]. Unfortunately, both MRI and CT tend to be bulky, expensive, and feature insufficient resolution for imaging small airways; thus, they are not optimal for studying airway injuries in small animal models in laboratory settings, and their availability is limited at exposure facilities. OCT is a non-invasive imaging technique that uses non-ionizing infrared light to visualize a cross-section of tissue with micrometer scale resolution. Endoscopic OCT probes have been developed to image intraluminal tissues and to get access to the deep structures in the body [27, 98]. In the respiratory system, endoscopic OCT has previously been used to quantify airway tissue structure [21, 99, 100], compliance [101], and lumen caliber [32]. Our group has previously demonstrated anatomical OCT scanning and three-dimensional reconstruction of a human upper airway in patients with obstructive sleep apnea [26] and quantified respiratory airflow using computational fluid dynamic (CFD) simulation [25].

However, to translate our studies into the airways of rodent models requires a significantly more compact endoscopic probe than previous designs since the diameter of a typical rat trachea is about 6 times smaller than a human's. Another limitation in previous studies was the manual tracing utilized to reconstruct the 3D structure of the airway from OCT images. This approach was tedious, time consuming, and limited the number and extent of airway analyses that could be performed.

The main challenge for studying airways in a small animal model using OCT is the size of the imaging probe. The maximum acceptable probe diameter is limited by the size of the conducting airways. The average diameter of the rat trachea is 2.8 mm [102]. In addition, animals exposed to MIC are likely to have edema, intraluminal narrowing due to epithelial sloughing and exudate, resulting in airway obstruction, with further compromise of the airway cross-sectional area. Although the traditional 1.5 um-in-diameter probe with focusing optics provides high resolution and long working distance image, a smaller size is needed for investigating an obstructed airway in small animals in order to preserve the tissue structure. Recently, Moon *et. al.* proposed an all fiber optic endoscopic design for an ultra-thin imaging OCT probe [103, 104]. This design utilizes a large-core fiber and a stepwise transitional core structure to create a compact and flexible OCT endoscopy probe with a diameter of less than 1 mm. Nevertheless, practical translation of this technology for imaging rat airways exposed to toxic gas remains a challenge because another important aspect of repeatable testing within animal models is an automated measurement and quantitation of airway structure. In order to conduct large-scale animal testing, such as antidote efficacy screening, analysis of OCT images needs to be automated. An automatic segmentation method based on edge detection and graph theory has been recently developed to delineate and quantify the interior airway lining [105, 106]. However, those studies have been mostly limited to distinguishing tissue structure, such as thickness in 2D OCT images.

In this study, we optimized the design of a previously developed all fiber optic endoscopic probe specifically for use within rat trachea and applied an automated segmentation algorithm on OCT images to generate accurate 3D reconstructions. In the structural analysis, automatic and quantitative read-outs of trachea volume and cross-sectional area were obtained. The analysis results obtained from automated segmentation were evaluated and compared with manual segmentations. Additionally, we further questioned whether there was any spatial variation in the degree of injury and, if so, whether the obstructed region could be defined within the trachea. This paper details the fabrication process of an all-fiber probe, method of automated segmentation, and analytic results in an MIC-exposed rat model.

4.3 Methods

4.3.1 MIC synthesis and rat inhalation exposure model

Methyl isocyanate (MIC) was prepared on site at MRIGlobal (Kansas City, MO) using the Curtius Rearrangement method by refluxing acetyl chloride with sodium azide in toluene until the starting materials were consumed. It was demonstrated to be 99.2% pure by gas chromatography-flame ionization detection (GC-FID). For exposure of rats, the entire system was contained within a fume hood. Male Sprague-Dawley rats (250-300 g) were exposed in a nose-only (CH Technologies) system. MIC vapor was generated using a custom vapor diffusion proprietary system (MRIGlobal) and delivered to the plenum of the exposure system in a mixture of dry nitrogen (50 mL/min UHP nitrogen) that was subsequently blended with carbon- and HEPA-filtered dry air (10-15 L/min depending on desired dose). Downstream from the site of mixing, gas constituents were monitored via access of a 3-way valve by Fourier transform infrared spectroscopy (FTIR) and subsequently delivered to the plenum of the CH Technologies system.

Exhaust from that system was subsequently scrubbed in 10% sodium hydroxide and exhausted through the hood via a pump**.** All procedures were performed under the approval and in accordance with the regulations of Institutional Animal Care and Use Committee (IACUC) at MRIGlobal (Kansas City, MO) under protocol 112515(06)1E.

4.3.2 Optical coherence tomography imaging system

Our imaging system is based on SS-OCT system described in **Figure 3.2** and utilizes a 50 kHz swept-source laser (1310nm, AXSUN Technologies, Billerica, MA) with a bandwidth of 110 nm. The output beam from the laser is first split by a 90/10 coupler into the OCT sample arm and the reference arm. The reference arm has an optical delay line and a Faraday mirror to adjust the optical path length and create interference with the light in the sample arm. The sample arm consists of a fiber optic rotary joint, a motorized linear pullback stage, and an endoscopic probe to achieve volumetric scanning of the rat airway. Dual circulators direct the reflected light from the sample and reference arm to a 50/50 coupler, and the OCT interference fringe is detected by a 1.6 GHz wide balanced detector. Finally, the signal from the detector is sampled using a 12-bit data acquisition card (500MHz, Alazar Technologies Inc., Pointe-Clare, Quebec, Canada). The emitting power of the probe was 5.8 mW, and the system sensitivity was estimated to be 102 dB at the time of the measurement.

4.3.3 Fabrication of a fully fiber optic endoscopic probe.

A flexible, side-scanning, ultra-small endoscopic OCT probe was designed to examine rat tracheas. Since toxic gas inhalation often causes airway obstruction and narrowing, the anatomical structure of the airway is severely restricted, which makes it difficult for most endoscopic OCT probes to pass through. We adopted a previously proposed lens-free probe design [103] and optimized it for examining the rat airway. In this probe, a stepwise transitional core structure was

utilized instead of a focusing lens to reduce the divergence of light and increase the lateral resolution of the probe. This was done by splicing together a series of optical fibers with different core diameters of 9, 12, and 20 um (**Figure 4.1**). The probe did not require any additional focusing optics since the diameter of healthy rat trachea is typically 2.8 mm. In this range, the light divergence is not significant. Additionally, the distal end face of the optical fiber was polished at a 49-degree angle (ϕ) to achieve total internal reflection. Based on our previous lens-free probe designs, the polishing angle was slightly deviated from 45 degree to reduce back reflection from the fiber cladding and the sheath surface [103, 104]. A metal housing was placed outside the optical fiber to reduce friction during rotational scanning and minimize non-uniform rotational distortion from degrading the image. During scanning, the probe was further protected by a 24-gauge optically transparent sheath so that the endoscopic probe would not damage the airway epithelium during rotation. The outer diameter of the fabricated probe was 0.4 mm, which was much smaller than the previously designed 1.2 mm endoscopic probe used for humans [26]. The probe was proximally connected to an external rotational motor so that it rotated at 1,500 rpm and acquired the 2D images at a rate of 25 frames per second. The probe was pulled back at a constant speed of 5 mm/s along the airway to obtain three-dimensional scanning of the entire trachea. The axial and lateral resolutions of the probe are 6.8 um and 34 um in air, respectively, when the target is placed at a distance of 0.5 mm. Detailed characterizations of the fiber optic probe with a similar design have been described previously by Moon *et al.* [104].

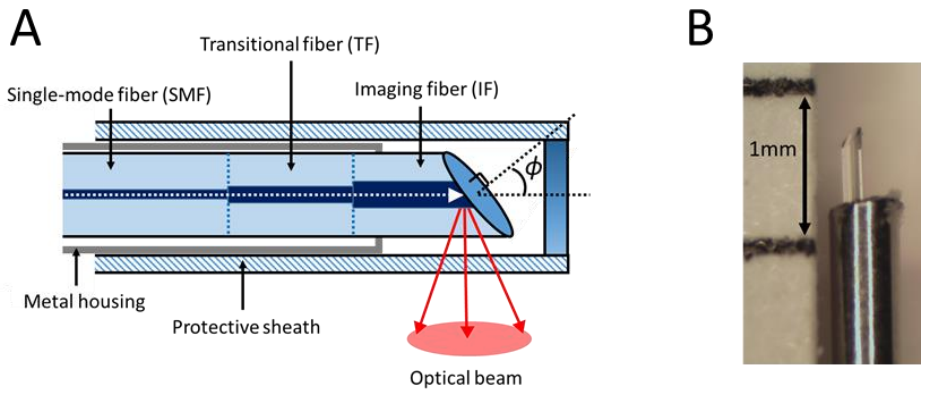

Figure 4.1 Bare-fiber OCT probe. (A) The probe is made of three optical fibers with core sizes of 9, 12, and 20um to decrease light divergence and increase imaging range and lateral resolution. The imaging fiber is polished at a 49-degree angle (ϕ) to reflect the optical beam. Metal housing is placed around the fiber to reduce the friction during rotation, and a transparent 49tects the probe and the tissue. (B) The diameter of probe is 0.4 mm and placed in a 24G protective sheath (not shown) with 0.6 mm outer diameter.

4.3.4 Reconstruction of airway structure and visualization of obstruction

In order to reconstruct the three-dimensional structure of the airway lumen inner surface, an automated segmentation algorithm was applied to each OCT B-scan image. Afterwards, the 3D surface inner lumen of the airway structure was reconstructed based on the spacing between each frame. The automated segmentation program consists of 3 steps: de-noising, feature extraction, and edge detection. In the de-noising step, noise and artifacts are removed as much as possible to optimize segmentation results. A median filter is applied to suppress speckle noise. In addition, the summation of the pixel intensity in a single A-line is normalized so that the strong reflection from the sheath can be reduced [**Figure 4.2(A)]**. In the feature extraction step, the general structure of the airway is identified, and the most inner (medial) surface is emphasized so that segmentation analysis of the intraluminal suerface can be performed. Binarization provides a general shape of the trachea wall [**Figure 4.2(B)**]. In the binary image, small objects are removed so that tissue can be distinguished from artifacts such as the sheath. Additionally, any pixels underneath the tissue are masked and de-emphasized so that only the most inner surface of the luminal wall will be

segmented in the following step [**Figure 4.2(C)]**. This prevents the program from detecting another tissue surface caused by luminal detachment. In the last step, the edge of the luminal surface is detected using a dynamic programming (DP) algorithm. Briefly, the gradient image is initially obtained by taking the 1st derivative of pixel intensity along the depth [**Figure 4.2(D)]**. Then, the DP algorithm is applied to the gradient image to detect the inner luminal surface [**Figure 4.2(E)]**. Since we apply a mask to emphasize the top layer of the tissue in the OCT image, the DP algorithm only identifies the intraluminal space in which the probe is placed. Once the intraluminal wall is segmented with edge detection, we create a stack of binary images with only the inner luminal space highlighted. Then, the stack of the binary images of the inner luminal area is reconstructed into a 3D volume [**Figure 4.2(F)]**.

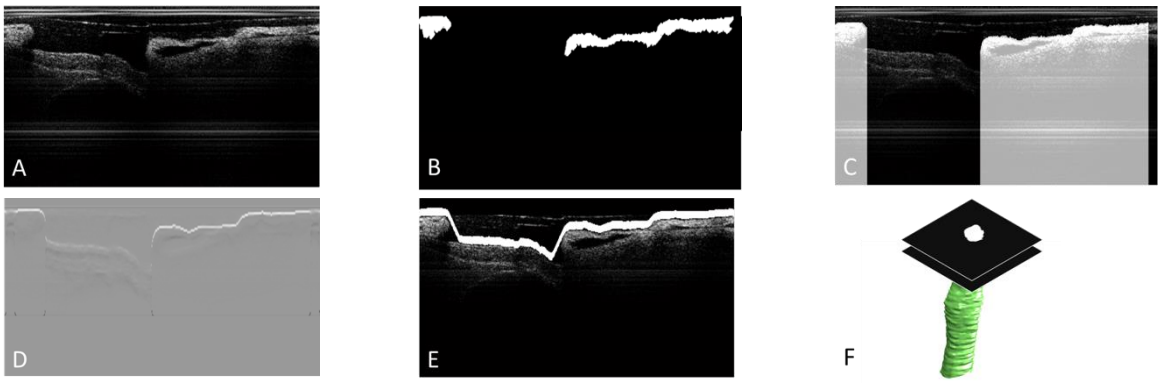

Figure 4.2 Endoscopic OCT images of MIC-exposed rat airway (A) after de-noising; (B) binarization reveals the general shape of lumen wall; (C) emphasizing the most inner lumen surface by creating large pixel intensity differences on the top surface; (D) first derivative of pixel intensity in the depth detection; (E) edge detection using dynamic programming; (F) 3D reconstruction of segmented image. The inter-frame distance is 0.2 mm.

4.4 Results

Airways of rats exposed in an MIC inhalation model were first visualized using an all-fiber miniature OCT probe. Then, the 3D structure of the intraluminal wall was reconstructed and analyzed from OCT images using the automated segmentation algorithm.

4.4.1 *Ex Vivo* OCT imaging of rat trachea.

Using the all-fiber miniature endoscopic probe, *ex vivo* OCT volumetric scanning of the rat airway was obtained. In order to maintain the original anatomical structure, the rat airway and lung were left intact within the body of the animal after euthanasia. In addition, the rat samples were kept in iced saline-soaked gauze and imaged immediately to prevent structural alteration. Despite the small probe size and simple optics design, our OCT probe captured the entire airway structural image with little attenuation in signal. The OCT probe was inserted into the anterior nasal airway and carefully guided to the trachea so that the probe would not damage the airway (**Figure 4.3**). The distal end of the probe was placed at the carina with scans being obtained continuously up to the nasal cavity at a pullback speed of 5 mm/s. The entire scan took less than 15 seconds to complete.

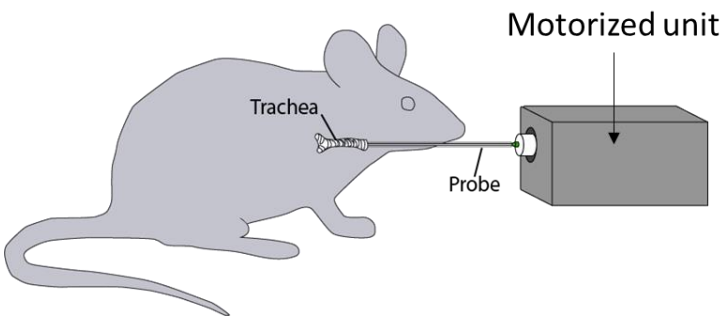

Figure 4.3 Endoscopic airway imaging of post-mortem rat trachea

OCT images of naive rat trachea without MIC exposure were first obtained as a control. As expected, the trachea had a hollow tubular shape with a smooth internal surface [**Figure 4.4(A)]**. Longitudinal scanning also demonstrated a relatively uniform luminal space across the trachea [**Figure 4.4(D)]**. Next, OCT images of trachea from an MIC-exposed rat were analyzed. The cross-sectional images revealed multiple compartments and false lumens within the trachea, which were formed by the partially detached tissue layers [**Figure 4.4(B)]**. In addition, multiple clear spaces were seen within the tracheal wall near the cartilage in some OCT images [**Figure**

4.4(C)]. Longitudinal sectioning of trachea from MIC-exposed rat clearly showed the obstructive tissue near the upper trachea [**Figure 4.4(E)]**.

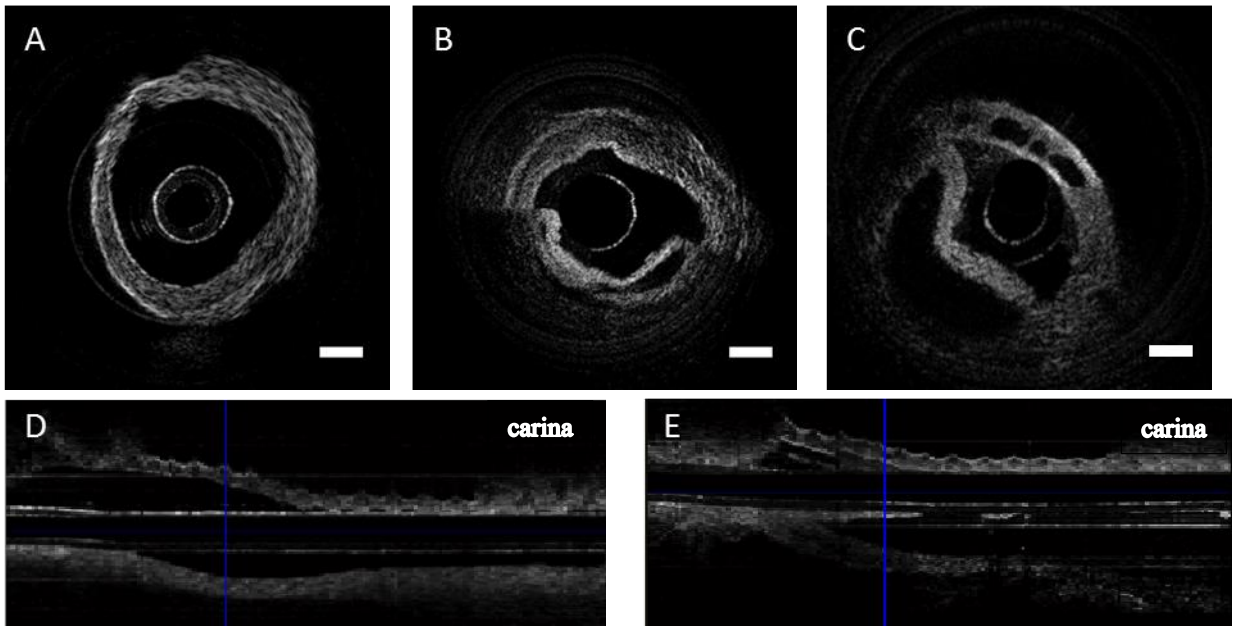

Figure 4.4 OCT images of rat trachea obtained with a bare-fiber OCT probe. (A) Normal rat trachea has relatively uniform thickness and approximates a circular shape. (B) MIC-exposed rat trachea has tissue detachment and sloughing. (C) Another MIC-exposed trachea shows the presence of open spaces within the airway wall. (D) Longitudinal sectioning of normal trachea shows mostly smooth airway structure. (E) Longitudinal sectioning of MIC trachea shows obstruction of lumen near the blue vertical line. Scale bar indicates 0.5 mm

4.4.2 3D model generation and structural analysis.

A 3D mesh and surface model of the tracheal structure, from the carina to the level of the epiglottis, was reconstructed from the OCT images. A total of 150 B-scan images were segmented to reconstruct a trachea of 3 cm in length for the control and MIC-exposed rat models. In the structural analysis, the volume and cross-sectional area of the intraluminal space across the airway were quantified. The control shows a relatively uniform luminal area across the trachea with an unobstructed air pathway. In contrast, the MIC-exposed rat trachea shows substantial regions of airway narrowing at the level of the epiglottis compared to the control trachea (**Figure 4.5**). The total tracheal volume was estimated to be 115 mm^3 and 54 mm^3 for control and MIC, respectively.

This demonstrated that MIC caused considerable reduction in the airway cross-section area (-2.27 mm^2) and volume (-61 mm^3) that could lead to airway compromise.

Figure 4.5 3D reconstruction of rat trachea using automated segmentation. (A) Normal rat trachea has a relatively uniform diameter with a tubular structure (**A**). The epiglottis opening can be located at the top of the reconstructed trachea. (B) MIC-exposed rat trachea shows airway narrowing, especially at the upper trachea.

4.5 Discussion

The airway is sensitive to toxic chemicals, and the inhalation of methyl isocyanate (MIC) can cause edema, fluid exudation into airways, airway obstruction, deformity or stenosis, and lead to death [91, 92]. Animal models have been developed and evaluated in order to understand the effect of this toxic gas and for development of new therapeutic agents. The toxic-inhaled rat model has especially been commonly utilized to conduct inhalation toxicity studies and investigate variable exposure periods and concentrations [107, 108]. Costs can be substantially reduced in the rat model versus other medium- and large-sized animal models, making it easy to screen and compare several potential countermeasures or drug interventions at once. Since MIC directly affects airway lumen tissue and causes obstruction, it is critical to investigate the extent and

location of injury and to be able to assess potential aerodynamic changes during and after exposure. Beckett investigated the respiratory effects caused by MIC in Bhopal patients with simple lung function measurements [109]. Stevens et al. demonstrated severely compromised lung function and persistent airway obstruction in rats using the nitrogen washout method [110]. However, direct and three-dimensional visualization of the airway structure is required to fully understand the site(s) and aerodynamics of airway obstruction and obtain accurate, quantitative measurements to facilitate development of effective treatments. Tracheal structure of small animals with MIC-induced injury has not been characterized *in situ* mainly due to the size restriction of the probe. In this study, we were able to successfully perform 3D structural analysis of rat trachea after exposure to inhaled MIC gas using a miniature probe design and an automated segmentation algorithm.

A fully fiber optic endoscopic probe was first designed so that the probe could scan rat trachea with MIC inhalation-induced injury. Our endoscopic probe provides high enough spatial resolution to reveal the morphological abnormalities in the tissue structure of rat airway and is small enough to cause no apparent tissue alteration during the probe insertion. Cross-section and longitudinal section of OCT images clearly demonstrated the obstruction and tissue detachment in MIC-exposed rat trachea. The detachment of tissue was not induced by the probe insertion but by the MIC exposure, as we can see from the histological examination in the MIC-exposed rat trachea without probe insertion (**Figure 4.6**). In addition, repeated OCT scanning of the same MIC-exposed trachea shows no apparent structural alteration, suggesting that it is not likely itself to cause further obstruction. We imaged the rat tracheas without any fixation to avoid structural and volume changes due to chemical treatment [111]. Prior to imaging, the trachea was kept intact with the rest of the body in cold saline-soaked gauze so that the sample was close to *in vivo*. We have

demonstrated this imaging technique is minimally invasive and can be applied to facilitate large-scale *in vivo* testing or longitudinal evaluation of airway obstruction.

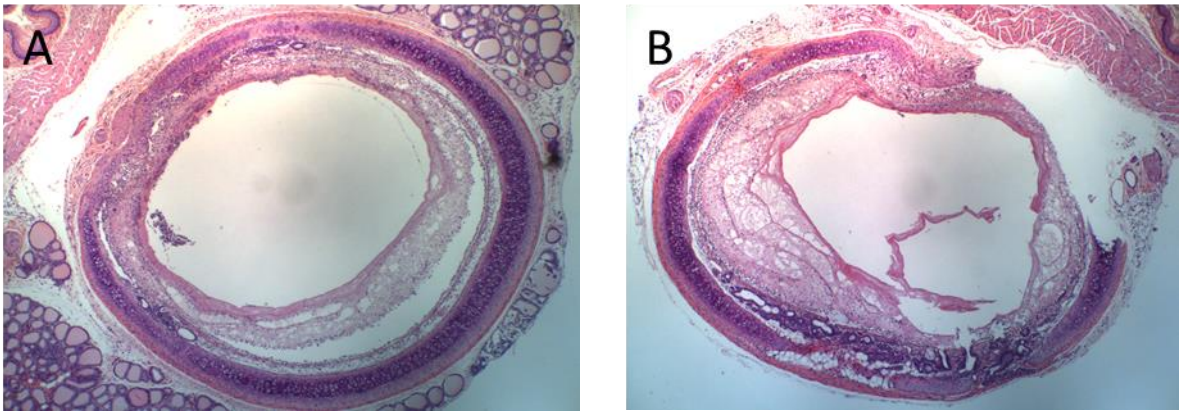

Figure 4.6 Histological sectioning of rat trachea exposed to MIC gas shows (A) the detachment of lumen from cartilage and (B) erosion of cartilage and stenosis.

The 3D reconstruction results from MIC-exposed rat trachea revealed differences in the degree of obstruction between the upper trachea and lower trachea. The upper trachea in the MIC-exposed animal showed significant narrowing compared to the normal trachea while the lower trachea only showed moderate airway narrowing (**Figure 4.7**). It is possible that the upper trachea and lower trachea near bronchi react to the chemicals differently, and exposure to MIC, a highly reactive and readily absorbed molecule, would be expected to impact more proximal airways to a greater extent [7]. It could also be due to other differences in the deposition or sensitivity of airway regions to specific chemicals. Our previous study showed that there are differences in the degree of smoke inhalation-induced airway injury between upper and lower trachea in a rabbit model [18]. However, large-scale animal studies are needed to substantiate the biological mechanisms of MIC injury, which will be conducted in the our future studies.

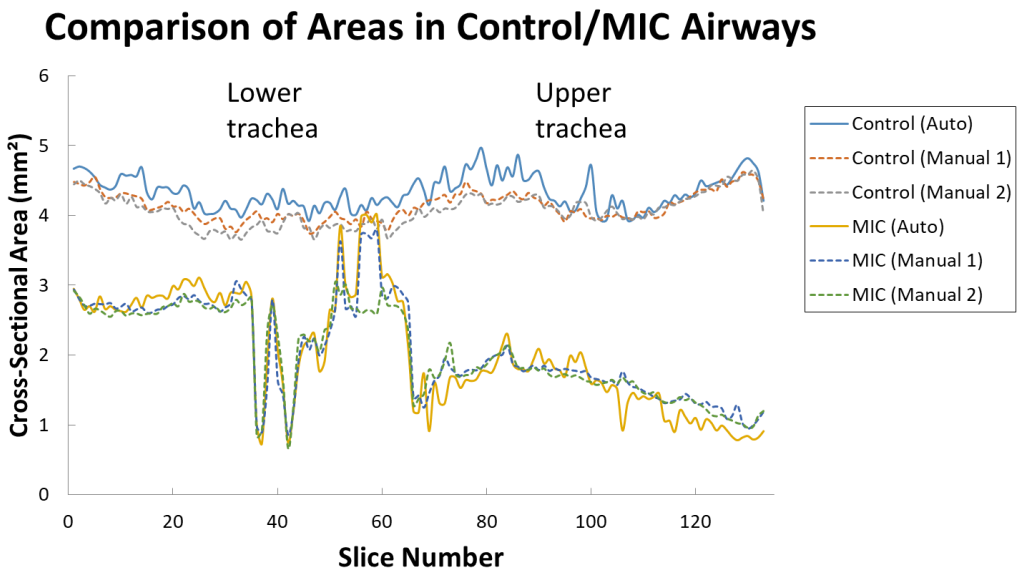

Figure 4.7 The plot of cross-section area from carina (slice 0) to epiglottis opening (slice 130). While the control shows consistent cross-section area, the MIC-exposed trachea shows significant narrowing near epiglottis. The OCT slices are 0.2 mm apart.

In this study, we have evaluated a fully fiber optic miniature OCT probe for scanning the airway in small animal models and developed an automated 3D segmentation algorithm for reconstructing a 3D airway structure with minimum human intervention. We demonstrated that *ex vivo* rat trachea with MIC inhalation induced injury can be analyzed in 3D, and physiological parameters, such as tracheal volume and the cross-sectional area, can be obtained. If performed immediately upon procurement of the sample, the technique also could be used to quantitate airway obstruction without lung fixation. We are now prepared to use this approach for screening chemical countermeasure effectiveness that will have more focus on the biological mechanisms of MIC injury. Furthermore, this approach should provide enabling technology for additional study directions. For example, functional information could then be obtained from computational simulation such as computational fluid dynamics analysis. Since the probe is less than 0.5 mm in diameter, this technique should be applicable to investigating small animal models *in vivo* without necessitating sacrifice of the animals. Investigating the animals serially at different time points

without sacrificing has many advantages since the toxic substances usually affect the airway in a time-dependent manner, and recovery may be slow or delayed, and late phase complications can occur. However, airway motion due to breathing as well as cardiovascular pulsation could both cause motion artifacts. In addition, animals in this study, following inhalation of high levels of MIC, have substantial respiratory distress and hypoxemia. Introducing even a small endoscopic probe can cause profound obstruction, severe distress, and even greater motion artifacts. Therefore, additional effort, practice, and, possibly, an even thinner probe are required to complete the study such that the rat can be re-awakened and studied again subsequently. This imaging technique could also be combined with other techniques used in OCT to open up areas for functional information investigations of the trachea in small animal models. OCT could potentially be combined with fluorescence imaging to investigate depth of injury, epithelial regeneration and healing, and inflammatory response [112, 113]. Compliance and viscoelasticity of airway tissue also could be investigated with optical coherence electrography. Different light sources can be utlized to invest rat airway with higher resolution [114] or deeper penetration depth [115]. In addition, ultrasound could be used for displacement in the tissue from external sites to investigate its material properties [116, 117].

Chapter 5 – PROXIMAL AIRWAY VOLUME SEGMENTATION PREDICTS ACUTE RESPIRATORY DISTRESS SYNDROME (ARDS) RISK IN INHALATION INJURY

5.1 Overview

Acute respiratory distress syndrome (ARDS) is a severe form of acute lung injury with a mortality rate of up to 40%. Early management of ARDS has been difficult due to the lack of sensitive imaging tools and robust analysis software. We previously designed an OCT system to evaluate mucosa thickness (MT) post smoke inhalation, but the analysis relied on manual segmentation. The aim of this study is to assess in vivo airway volume (AV) after inhalation injury using automated OCT segmentation and correlate the AV to lung function for rapid indication of ARDS. Anesthetized female Yorkshire pigs (n=14) received smoke inhalation injury (SII) and 40% total body surface area thermal burns. Measurements of PiO2-to-FiO2 ratio (PFR), peak inspiratory pressure (PIP), dynamic compliance, airway resistance, and OCT bronchoscopy were carried out at baseline, post-injury, 24, 48, 72 hours after injury. A tissue segmentation algorithm based on graph theory was employed to reconstruct a 3D model of lower respiratory tract and estimate AV. We found AV was correlated with PFR, PIP, compliance, resistance, and MT measurement using a linear regression model. In addition, AV decreased after the SII: the group mean of airway volume at baseline, post-injury, 24, 48, 72 hours were 20.86 cm^3 (±1.39 cm^3), 17.61 cm^3 (±0.99 cm^3), 14.83 cm^3 (±1.20 cm^3), 14.88 cm^3 (±1.21 cm^3), and 13.11 cm^3 (±1.59 cm^3), respectively. The decrease in the AV was more prominent in the animals that developed ARDS after 24 hours after the injury. AV was significantly correlated with PIP ($r=0.48$, p <0.001), compliance ($r=0.55$, p <0.001), resistance ($r=0.35$, p <0.01), MT ($r=0.60$, p <0.001), and PFR

($r=0.34$, p <0.01). This study demonstrates OCT is a useful tool to quantify changes in MT and AV after SII and burns, which can be used as predictors of developing ARDS at an early stage. This chapter is adopted from [118] © The Journal of Trauma and Acute Care Surgery.

5.2 Background and Motivation

Diagnosis and early management of acute respiratory distress syndrome (ARDS) is an unresolved clinical problem in modern burn care [119]. In the new ARDS definition, ARDS is defined as an acute inflammatory syndrome that accompanied with increased permeability of the alveolar-capillary membrane [120, 121]. ARDS severity is classified based on hypoxia levels as characterized by PiO_2-to-FiO_2 ratio (PFR): mild (PFR of 201-300mmHg), moderate (PFR of 101-200mmHg), and severe (PFR of less than 100 mmHg) [120]. After a burn and smoke inhalation, the patient can develop ARDS via direct lung injury, smoke or inflammatory response from the burn, and complications such as infection [122]. As shown by Belenkiy et al. and others, about 30% of mechanically ventilated burn unit patients incur ARDS leading to high mortality depending on the degree of ARDS severity [123–126]. ARDS is associated with high short-term mortality (11-46%), [127, 128] prolonged mechanical ventilation,[127] and increased treatment cost [129]. Hence, delayed diagnosis of ARDS and late intubation can lead to worsening conditions [130, 131]. We propose that proximal airway permeability and responsiveness in inhalation exposures will correlate alveolar permeability during ARDS development, and therefore, direct assessment of physiological changes in proximal airway can potentially improve early diagnostic capabilities. Several studies have demonstrated the correlation between airway dimension measured from a chest computed tomography (CT) and pulmonary function in chronic obstructive pulmonary disease patients [132–135]. However, CT is generally costly and employs bulky and non-portable

imaging device. In addition, a standard CT does not provide enough spatial resolution to visualize tissue changes below 0.5 mm [136]. Optical imaging is generally cheaper and has higher spatial resolution than CT and magnetic resonance imaging (MRI). However, only a few studies with a limited number of animals have been conducted to investigate whether the histopathology and anatomical changes in the proximal airway measured by an optical imaging technique can be used clinically to assess the airway and lung injury after smoke inhalation [17, 20, 137, 138].

OCT is a high-resolution non-destructive imaging tool that can provide information on tissue morphology and substructure at near histopathological resolution. Utilizing the long-coherence length infrared vertical-cavity surface-emitting laser, volumetric scanning of OCT is capable of capturing micron level tissue imaging over a large area [139]. Previous studies have demonstrated that mucosa thickness (MT) changes in animal models after smoke inhalation and burn using OCT performed during bronchoscopy [17, 137, 138]. Additionally, *in vivo* visualization of airway structure in humans was demonstrated [22, 26, 140]. However, the analysis of the OCT data mostly relies on manual segmentation, which is time-consuming, labor-intensive, and subject to observer errors. Previously, we demonstrated an automated segmentation method for OCT to segment the MT and airway structure after exposure to smoke [105] and industrial toxic chemicals [12]. However, a longitudinal study that follows the changes in the proximal airway volume (PAV) after SII has not been reported. In addition, airway segmentation of a large number of animals with different severities of injury has not been performed. Therefore, in this study, we monitored the changes in proximal airway using a porcine SII and burn model established in our lab and an airway segmentation algorithm following injury progression up to 72 hours post-exposure. Then, we compared the PAV measurement with pulmonary physiologic and ventilator data [peak inspiratory pressure (PIP), compliance, and resistance], PFR, and MT. We hypothesized

that 1) inhalation injury leads to the changes in the PAV, 2) PAV is correlated to the changes in airway function and histopathology indicative of ARDS severity, and 3) there is a difference in the degree of airway narrowing for the animals that develop ARDS.

5.3 Methods

All experiments were carried out at the U.S. Army Institute of Surgical Research (USAISR), Joint Base San Antonio, Ft. Sam Houston, Texas, and were approved by the USAISR Institutional Animal Care and Use Committee (USAISR Protocols A-13-013-TS2, A-14-001, A-16-026). The study was conducted in compliance with the Animal Welfare Act, implemented Animal Welfare Regulations, and was in accordance with the principles of the *Guide for the Care and Use of Laboratory Animals*.

5.3.1 Porcine Smoke Inhalation and Burn Model

The 3D reconstruction and mucosa measurement were conducted on 14 female Yorkshire pigs from an ongoing study based on the availability of the OCT images. All animals were instrumented and transported to a procedure room to induce airway injury using the SII and burn injury model previously described [125, 141]. In this model, cooled smoke was administered through an endotracheal tube at 30 mL/kg per breath to yield a total of 28 -30 L of smoke. This led to arterial carboxyhemoglobin (COHb) levels of 80-90% at the end of injury. Following SII, a 40% total body surface area third-degree burn was induced by a Bunsen burner. Post-injury, animals were observed in a round-the-clock animal intensive care unit (IUC) for 72 hours. Airway suctioning was performed as needed before OCT imaging. PFR was calculated from the arterial blood gas level using an iSTAT blood analyzer (Abbott Point of Care, Princeton, NJ). PFR of

under 300 is considered as ARDS according to the consensus definition [120]. At the end of the study, the animals were euthanized with an intravenous dose of veterinary euthanasia solution.

5.3.2 Optical Coherence Tomography Measurement

MT and airway structure were obtained from OCT images acquired at baseline (BL), post-injury (PI), 24, 48, and 72 hours after the injury. A previously described long-range OCT system was utilized to image the lower respiratory tract (see supplemental information for details) [142]. During the image acquisition, a flexible OCT imaging probe was placed at the right bronchi through a working channel of a fiber bronchoscope in order to repeatedly scan the same area. In this study, OCT was used to obtain a 3-dimensional anatomical structure of proximal airway, from terminal bronchiole to carina, as well as tissue substructure features, such as mucosa and submucosa layer, cartilage, and signs of tissue damage. The total image acquisition time was less than 1 minute including the placement of the bronchoscope. Mucosa layer can be identified as a high-intensity superficial layer in the OCT images (**Figure 5.1**). At the same time points, measurements of ventilation data (PIP, dynamic compliance, and airway resistance) and blood gas level (PFR) were conducted.

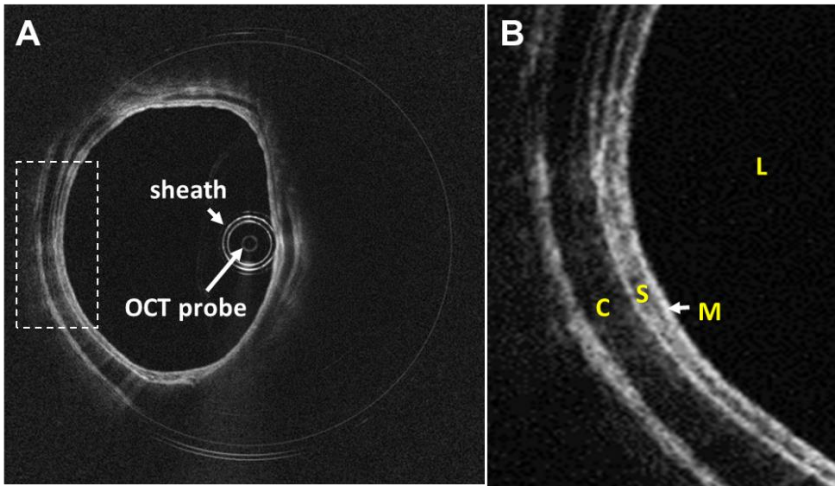

Figure 5.1 Mucosa thickness assessed from an OCT image. (A) Original OCT image and (B) enlarged detail of the white box portion. L: lumen, M: mucosa, S: submucosa, C: cartilage.

5.3.3 Tissue Segmentation Algorithm

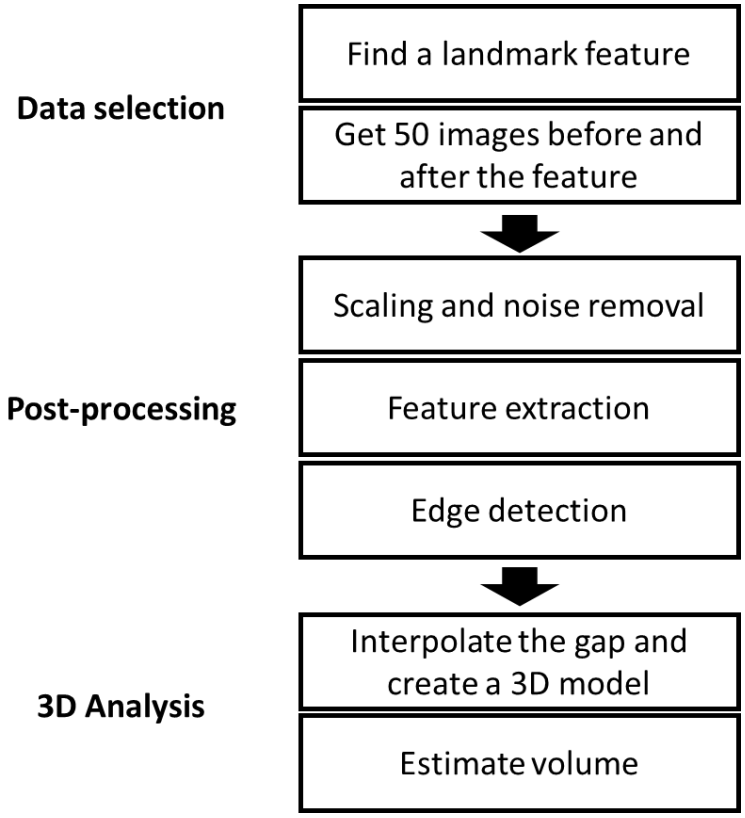

Figure 5.2 Flowchart of automated airway volume assessment process

A 3D model of the lower respiratory tract (5 cm portion) was reconstructed (localized as described below), and the lumen area and PAV were assessed using a semi-automated segmentation algorithm. The workflow of the automated volume assessment is illustrated in **Figure 5.2**. Since the OCT scanning range varies across the different data set, 100 consecutive OCT images were selected for the volume assessment, which corresponds to 5 cm in length. To uniformly select the same anatomical position, bifurcation at the carina was used as a landmark feature to select OCT imaging analytical site location midpoint. In this study, the 50 images before (distal) and after (proximal) the second bifurcation were selected. The tissue segmentation method is based on the dynamic programming algorithm [12, 72, 105] and detailed in Chapter 3. Based on the segmented tissue surface, a binary image of intra-lumen space is created. A 3D airway model

is reconstructed by interpolating the 2D binary images. **Figure 5.3** shows an example of lumen segmentation.

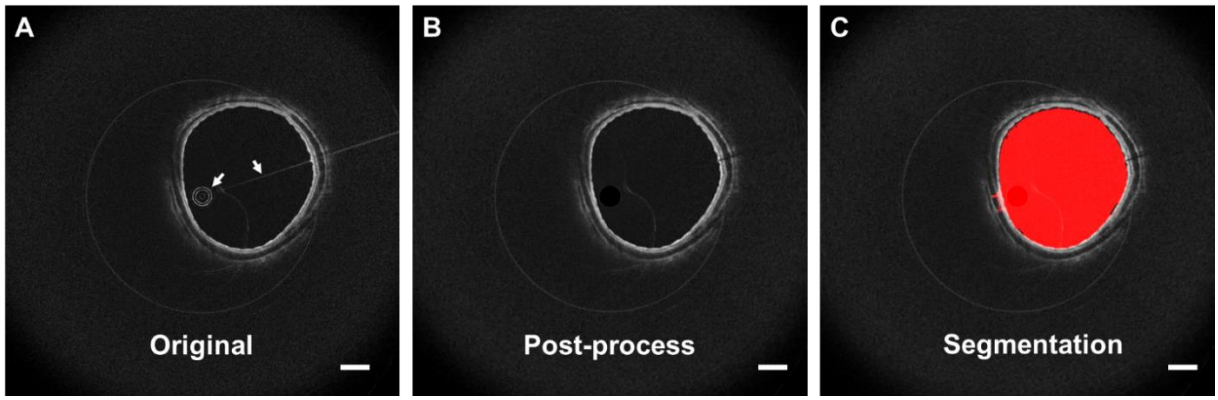

Figure 5.3 Example of lumen segmentation. A) Original OCT image. Artifacts from the sheath surface and reflection were indicated by white arrows. B) Image after post-processing. Sheath artifacts were removed, and the image was scaled based on the sheath diameter. C) Segmentation of lumen indicated by red area. Scale bar is 1mm.

Each OCT image takes 2.2 seconds to process, which is much faster than manual tracing. The segmentation accuracy was evaluated with manual tracing. An experienced OCT reader was recruited to trace the tissue surface from OCT images, and the amount of spatial overlap was calculated using the Dice similarity coefficient (DSC), described in equation (1). X and Y indicate the area of a binary image segmented from the corresponding OCT image with the automated algorithm and manual tracing, respectively.

$$\mathrm{DSC} = 2|\mathrm{X} \cap \mathrm{Y}|/(|\mathrm{X}| + |\mathrm{Y}|) \tag{5.1}$$

5.3.4 Statistical Analysis

All the statistical analyses were performed in a statistical software, *R* [143]. PAV was correlated with MT, PFR, and ventilator data (PIP, dynamic compliance, and resistance) using a Spearman's rank correlation coefficient (r) and linear regression model (p). Statistical significance was established at $p<0.05$.

5.4 Results

Of 14 animals, 7 pigs developed ARDS and 7 pigs did not develop ARDS (non-ARDS) based on the PFR measurement. **Figure 5.4** shows an example of reconstructed 3D models of pig airways acquired using the OCT bronchoscopy system at different time points. A 3D model was reconstructed from 100 OCT B-scan images which were equal to 5 cm of the lower respiratory tract. The computing time for each segmentation was less than 4 min. Both 2D cross-sectional images and 3D airway models show the constriction in the airway after SII. Two bifurcations can be identified in the middle portion of all the 3D models, indicating an analysis at a consistent location. DSC showed a high overlay index between manual segmentation and automated segmentation at all the time points of the study (BL: 0.96, PI: 0.94, 24-hour: 0.95, 48-hour: 0.95, 72-hour: 0.88).

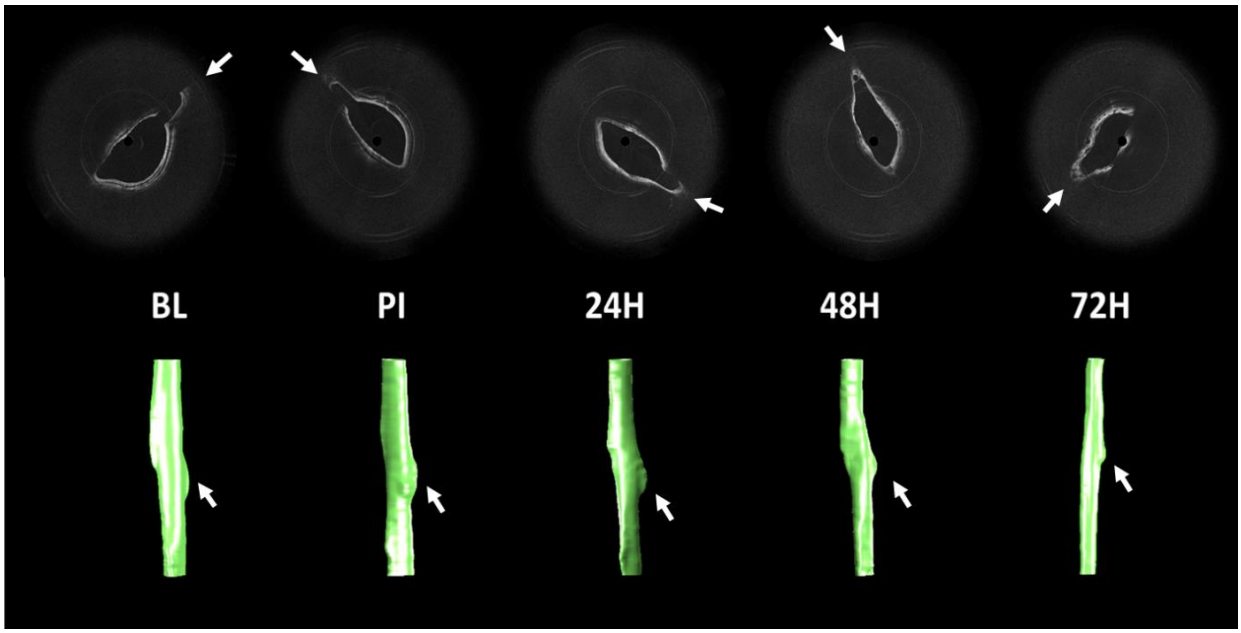

Figure 5.4 2D OCT images (top) and reconstructed 3D airway models (bottom) at baseline (BL), post injury (PI), 24, 48, 72 hours after injury.2D OCT images are approximately from the same location. 3D models show two bifurcations in the airway. The reduction in the proximal airway volume can be observed in the 3D model after injury. Arrows indicate the bifurcation in the lower respiratory tract used as a landmark feature to select the OCT images.

PAV dropped immediately after the injury and continued to decrease after 24, 48, and 72 hours (**Figure 5.5**). Mean AV at baseline (BL), post-injury (PI), 24-hours, 48-hours, 72-hours are 20.86 cm3 (±1.39 cm3), 17.61 cm3 (±0.99 cm3), 14.83 cm3 (±1.20 cm3), 14.88 cm3 (±1.21 cm3), 13.11 cm3 (±1.59 cm3), respectively. In addition, linear regression indicated AV is significantly correlated with MT ($r=0.60, p<0.001$), PFR ($r=0.34, p<0.01$), PIP ($r=0.48, p<0.001$), compliance ($r=0.55, p<0.001$), and resistance ($r=0.35, p<0.01$), as shown in **Figure 5.6**. Especially, MT had the highest correlation coefficient and compliance had the second highest correlation coefficient. Additionally, animals diagnosed as ARDS had lower PAV after 24 hours although they initially had a higher PAV than the non-ARDS group. Similarly, PIP, dynamic compliance, MT, and PFR showed more drastic changes after 24 hours of injury in ARDS animals. On the other hand, resistance did not differ until 48 hours of injury.

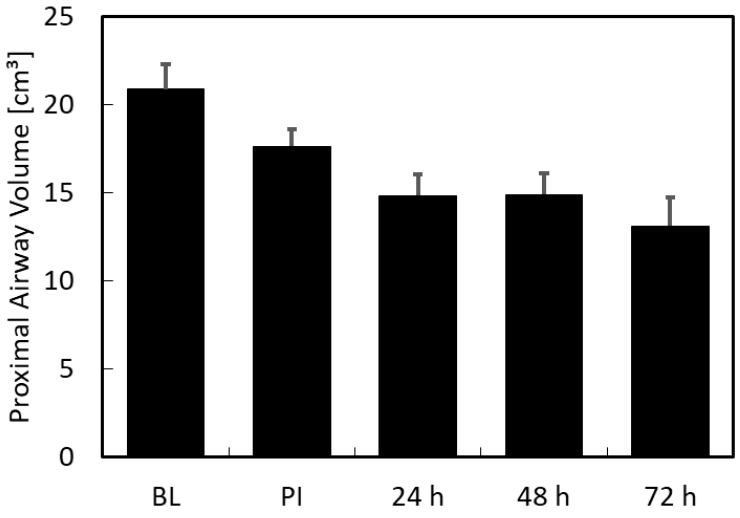

Figure 5.5 Changes in the proximal airway volume (PAV) due to SII.

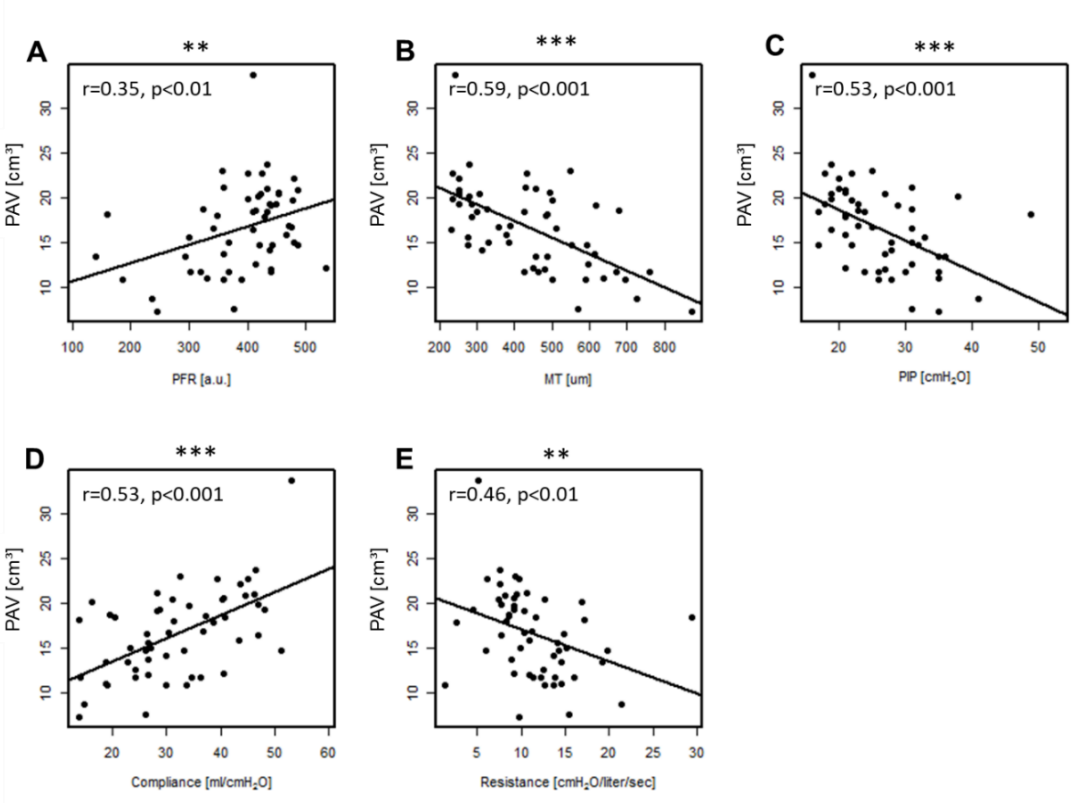

Figure 5.6 Linear regression analysis. Linear regression model shows a significant correlation between (A) PiO_2-to-FiO_2 ratio (PFR) and volume, (B) mucosa thickness (MT) and volume, (C) peak inspiratory pressure (PIP) and volume, (D) compliance and volume, and (E) resistance and volume. ** $p<0.01$, *** $p<0.001$.

5.5 Discussion

This study demonstrated the capability of a proposed long-range OCT bronchoscopy system to assess PAV after SII and burn in a pig model in addition to the previously shown MT measurement [17, 138]. The main contributions of this work are as follows: 1) an automated segmentation method was established for SII monitoring, and we validated that OCT can assess the PAV changes due to airway injury; 2) we demonstrated that changes in PAV in the lower respiratory tract are correlated with the ventilation data, PFR, and the MT measurement; 3) we demonstrated the possibility of using PAV changes to detect changes that correlate with development of ARDS as early as 24 hours.

An advantage of OCT is that we have been able to adapt it to provide direct, quantitative epithelial swelling information and anatomical changes in the airway with micron-meter resolution rather than with indirect function measurement. Therefore, compared to other pulmonary function and blood measurements, OCT may capture early subtle physiological changes and aid early diagnosis of airway injury. Prior studies have demonstrated the diagnostic capability of OCT in detecting micro-meter MT changes due to edema and inflammation after SII, which were correlated with the severity of the injury [17, 138]. In this study, we showed the group average PAV of the ARDS group decreased by 8.32 cm^3 (-38.4%) after 24 hours of injury, which is a much greater decrease than the PAV of the non-ARDS group (3.44 cm^3 or -17.3%) considering the mean baseline PAV was 20 cm^3. In addition, the correlation between PAV and other airway function measurements suggests that OCT can obtain information about the microenvironment and physiological response in the airway and lung by scanning the 3D anatomical structure. Further investigation is required to reveal if changes in the airway and pulmonary physiology directly leads to the proximal airway constriction. While airway resistance and dynamic compliance are known to be associated with airway physiology, it is unclear if the pulmonary functions such as PIP and PFR directly affect airway volume. If we show the proximal airway physiology indicate the pulmonary functions, OCT airway measurement will be a good predictor of ARDS.

However, there are several current limitations to consider: since the bronchoscopic probe has to be inserted and scanned across the lesions, the obtained OCT data represent only one part of the airway, namely the proximal airway. We need to be aware that bronchoscopic OCT does not represent the entire airway and lung. Therefore, we need to supplement with other measurements. In addition, motion and breathing artifacts of the subject can affect the airway volume measurement. Since the airway has an elastic structure, airway volume can fluctuate

depending on the breathing cycle. Currently, we scan the proximal airway multiple times and average the PAV to reduce the breathing artifact. However, this increases the procedure length and potentially poses a risk to the patient's health. One solution to this problem is to apply end-respiratory breath-hold technique using a ventilator during the probe scanning, which typically is no more than 8 seconds. Another solution is to implement a pressure sensor to the endoscope tip and record the respiratory pressure during the image acquisition to keep track of the breathing cycle. Finite element models and other simulation software can be utilized to "calibrate" airway volume. The pressure sensor also allows us to directly measure the airway compliance, which can be useful in detecting the injury and monitoring recovery [30]. In addition to the technical limitations, a question remains whether the airway constriction assessed from OCT is primarily due to external burns or chemical damage. Since both loss of chest wall elasticity due to thermal injury and pulmonary edema from smoke inhalation can contribute to the decreased lung volume and the airway narrowing [144], future study will address the differences in PAV between the animals received burn alone and the ones received both burn and smoke inhalation. In addition, in the future study, the airway measurements from the animals receive neither burn nor smoke inhalation should be simultaneously acquired to eliminate the external factors that can affect the measurements. Finally, our animal model is designed to cause smoke exposure and burn injury under anesthesia and intubation. Therefore, the response and damage to the airway may be different from conscious inhalation of smoke due to the lack of coughing and sneezing. The smoke deposition pattern in a pig would also be expected to have some differences from a human. Therefore, further investigation is required to extend our findings to human clinical trials.

Despite some limitations, OCT can be a useful tool to provide rapid assessment of an airway injury and may give some information on likelihood of extent of alveolar injury and ARDS

risk. The entire OCT system fits in a standard bronchoscopy cart ($300 \times 500 \times 800$ mm in this study) and can be transported to a remote area to provide point-of-care diagnosis when a CT scan and MRI are not available. OCT provides high quality of airway edema information that can be useful in identifying the disease when the patient is exposed to inhalation injury.

5.6 Summary

We showed that OCT bronchoscopy has a capability to assess changes in MT and PAV following smoke inhalation and burns. OCT may be used as an early diagnostic tool for burn and smoke injury at point-of-care settings. Further studies in humans will follow.

Chapter 6 – GRAPH BASED ROTATIONAL NONUNIFORMITY CORRECTION FOR REGIONAL COMPLIANCE MEASUREMENT

6.1 Overview

In this study, we present a method for correcting non-uniform distortion (NURD) in a micromotor imaging catheter to obtain an accurate airway compliance measurement. The method corrects the distortion in the image by first identifying the wire artifact and then segmenting the nonlinear surface profile of the plastic sheath through dynamic programming. Since the probe is positioned nonconcentric in relative to the sheath, the surface profile of the sheath appears nonlinear in the polar coordinate image which can be used to effectively correct the local distortion in the image. In addition, since the proposed method does not require correlating the tissue signal, real-time correction of the NURD can be performed without relying on the tissue contrast. To demonstrate the feasibility, we acquired dynamic OCT images of human nasopharynx during the respiratory cycle. Localized compliance of different tissue types within the cross-sectional image was quantified.

6.2 Introduction

Measurement of tissue mechanical properties can provide important information about the presence and status of disease [145]. In the upper airway, compliance can affect the flow behavior and the low compliance tissue can cause airway collapse [146]. Obstructive sleep apnea (OSA) is a common condition in both adults and pediatrics caused by the blockage of airflow in the upper airway during sleep. Most OSA cases in pediatrics arise from adenotonsillar hypertrophy [147] where inflammation and infection can contribute to the enlargement of adenoids. In some cases,

tonsils and adenoids may grow to be large relative to the airway, leading to obstruction in the airflow. Adenotonsillectomy is currently the first line of treatment for pediatric OSA patients, but it is associated with high post-surgical complication rates including mortality and morbidity. The post-tonsillectomy mortality rate in the United States is estimated to be 1 in 10,000 [148]. Alternatively, adenoidectomy can be performed with reduced complication risk. However, the efficacy of adenoidectomy alone as compared to the adenotonsillectomy has been controversial, partially due to the lack of quantification tools to systematically study flow dynamics in the upper airway.

Long-range OCT, or anatomical OCT, has been introduced to provide minimally invasive and high-resolution anatomical scanning of the airway [22, 25, 84, 149]. Since OCT is a non-contact fiber optic-based imaging technique, a flexible endoscopic can be used in combination with the clinical videoscope in awake or sedated patients. In addition, a long-range OCT system has an exceptionally long imaging distance of typically >10 mm to capture the entire lumen. Long-range OCT has been applied in numerous clinical studies to diagnose subglottic stenosis in newborn babies [22] , provide surgical guidance for OSA [23, 149, 150], and detect inhalation injuries early [17, 151]. Jing et al. demonstrated a long-range OCT imaging probe can be integrated with other sensors, including positioning sensors or pressure sensors, to obtain additional physiological parameters [25]. In the same study, computational dynamic analysis from the anatomical scan was used to provide insight on the location of high airflow resistance.

Airway compliance has been studied using endoscopic OCT by several groups [29, 152–154]. Compliance is typically defined as the volume changes at a given pressure change. However, in the upper airway, compliance can be simplified as the changes in the cross-sectional area (CSA) of lumen over changes in pressure. This is because the axial deformation of the upper airway is

negligible compared to the radial expansion in the lumen. Airway compliance can be described as follows:

$$C = \frac{\Delta CSA}{\Delta Pressure} \tag{6.1}$$

Furthermore, regional compliance can be obtained by dividing the lumen into smaller segments and assessing the contribution of each part to the total compliance based on the geometrical shape of the lumen [29, 153]. Although the localized compliance measurement has been demonstrated, motion artifacts and nonuniform rotation distortion (NURD) can significantly affect the accuracy of compliance measurement. While motion artifacts from heart-beat and breathing can be avoided by simply increasing the imaging speed, such as implementing a high-speed micromotor, NURD correction is typically more challenging and has to be corrected by an image registration algorithm once the images are acquired. In a micromotor-based imaging probe, the main cause of NURD is the instability in the motor rotation due to an imbalance in the motor weight or disturbance in the driving voltage. As a result, the acquired image will be either under-sampled or over-sampled. In terms of the compliance measurement, NURD will make the tracking of local tissue displacement difficult as it induces translation and nonlinear deformation of the image. Several NURD correction algorithms have been proposed. One common and effective technique for NURD correction is image registration based on structural landmarks such as the wire artifact or fiducial marker [155, 156]. However, a wire can cast shadows to the tissue of interest in the OCT images and limit the field of view. In addition, identification of the exact location of the under-sampled or over-sampled region is still challenging, and improper correction can distort the image further. Other methods rely on correlating the speckle contrast in adjacent A-scans to determine the rotation speed [157–159]. However, the region with weak image contrast will lead to incorrect NURD correction. Finally, Sun et al. proposed a method based on the phase

shift induced by the NURD in the sheath signal to correct distortion [160]. Although this method does not require information on tissue, high phase stability is required.

In this study, we developed a 2-step NURD correction method based on intensity thresholding and graph-based segmentation of the nonlinear surface profile of the catheter sheath. To demonstrate the feasibility of the method, we captured the dynamic deformation in the upper airway under negative pressure in an adult volunteer. Imaging of a fixed cross-sectional plane in the nasopharynx was obtained during a respiratory cycle. Once the NURD correction algorithm was applied, an automated-edge detection algorithm was applied to the lumen to measure the regional compliance changes. To the best of our knowledge, this is the first demonstration of an OCT compliance measurement in an awake human patient.

6.3 Methods

6.3.1 High-speed micromotor imaging system

The long-range OCT imaging system and micromotor imaging probe used in this study have been previously described [25]. Briefly, the imaging system employs a 100 kHz VCSEL with a center wavelength of 1300nm and a bandwidth of 100 kHz. A high-speed balanced detector (PDB480C-AC, Thorlabs Inc., NJ) and a high-speed acquisition card (ATS9373, AlazarTech, Canada) are utilized to sample the high-frequency interference signal. Due to the narrow instantaneous linewidth of the VCSEL source, the coherence length is larger than 1-meter. The sensitivity roll-off in the acquired signal is predominantly due to the limited bandwidth of the acquisition devices. In this study, we achieved an imaging range of 25 mm. The imaging probe consisted of a commercial 0.9 mm micromotor (Kinetron, Netherlands), a micromirror, and a focusing optic which were placed into an 8 mm long, 1.2 mm diameter glass capillary. A 45-degree

mirror with a 0.9 mm outer diameter (OD) was positioned onto the shaft of the motor to reflect the light in the orthogonal direction with respect to the catheter. The imaging probe was further protected by a 1.8 mm diameter transparent sheath. Imaging was performed at 200 frame-per-seconds (500 A-scan/frame) during a respiratory cycle to capture the dynamic movement of the nasopharynx.

6.3.2 Dynamic airway imaging of a human patient

Before OCT imaging, the upper airway of the patient was locally anesthetized and decongested with a 4% lidocaine/oxymetazonline HCl nasal spray. After approximately 5 minutes when the nasal cavity was reported to be numb, the imaging probe was inserted into the nose and guided through the nasopharynx using patient feedback as well as OCT imaging (**Figure 6.1**). During the dynamic compliance measurement, the patient was asked to inhale and exhale air at approximately 60 breaths-per-minute. In addition to OCT, pressure measurement was simultaneously performed at the nasal cavity using a commercial 3.5F pressure catheter (Mikro-Cath, Millar, BA). The patient reported minimal discomfort during the measurement.

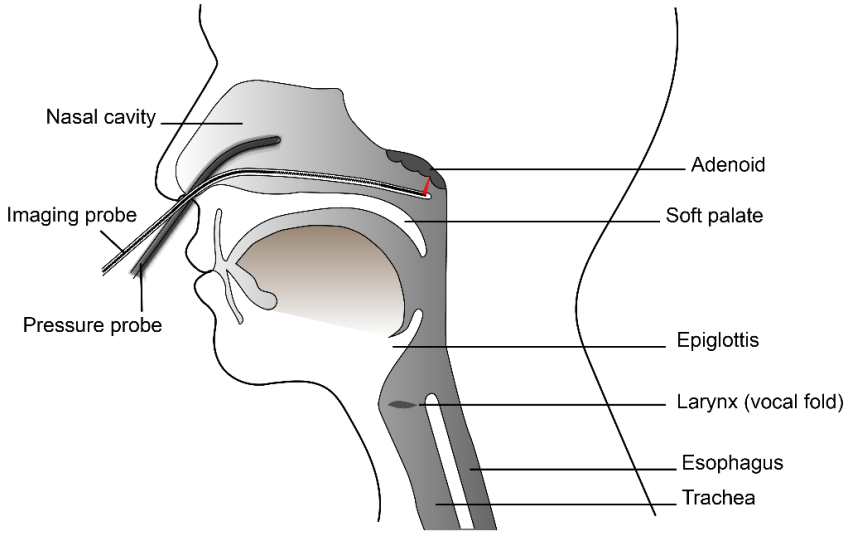

Figure 6.1 A schematic diagram showing the sagittal plane of airway anatomical structure and the placement of the imaging probe.

6.3.3 Nonuniform distortion (NURD) correction algorithm

In our study, a cross-section of the lumen is acquired as a series of polar OCT images. In the polar coordinate, the x-axis indicates the angle of the probe rotation and the y-axis indicates depth. **Figure 6.2** shows the center portion of OCT images that contains the catheter sheath displayed in polar and Cartesian coordinates. The proposed NURD correction algorithm is a 2-step process that uses the structural landmarks from the wire and the surface profile of the catheter sheath to correct local distortion.

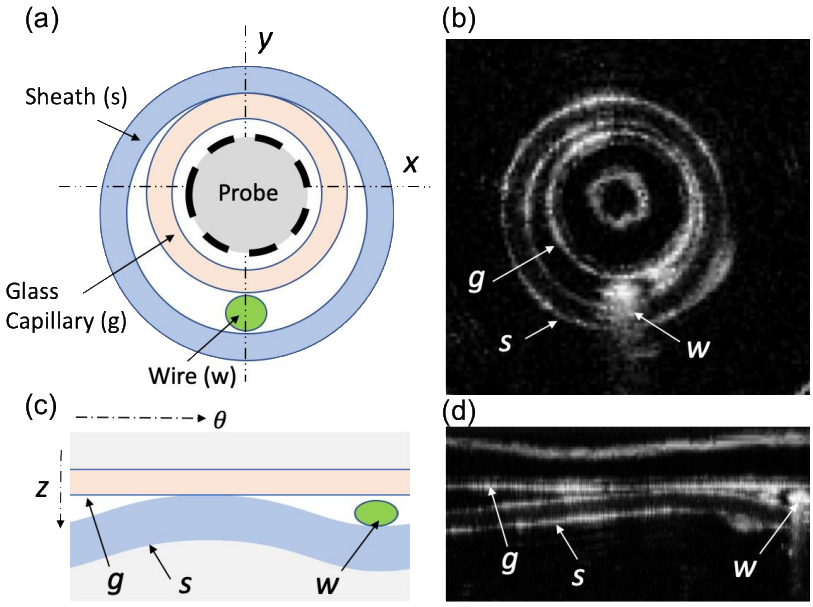

Figure 6.2 Center portion of the OCT image that contains the catheter sheath and the metal wire. (a,c) Schematics represented in Cartesian and polar coordinates. (b, d) OCT images represented in Cartesian and polar coordinates.

First, the location of the metal wire is identified, and the images are resampled so that each side of the image is aligned with the wire in the linear image. This ensures each image contains complete information in one rotation cycle. In other words, the wire artifact acts as an image-based triggering signal for each B-scan. Before post-processing, the polar images are stitched together horizontally based on the processing window size to create one continuous image [**Figure 6.3(a)]**.

Then, the location of the wire for the micromotor is identified using image thresholding [**Figure 6.3(b)**]. The wire creates higher reflection compared to the sheath and image artifacts. The remaining noise in the resulting binary image is then removed using a series of low-level operation to ensure robust operation.

1) Noise reduction: we applied a median filter to reduce the speckle noise.
2) Morphological operation: morphological erosion and dilation with a vertical structural element operation can be applied to reduce or eliminate the signal from glass capillary and sheath. The wire signal appears to be vertically elongated due to the tail artifact. [**Figure 6.3(c)**]
3) Area filtering: once the thresholding and morphological open operation is applied, any connected regions smaller than a certain pixel are removed to reduce the noise.

Once the binary images of the metal wire were created, the centroid of each wire is identified using a peak detection algorithm [**Figure 6.3(d)]**. Here, the minimum and maximum pixel interval is used to guide the peak detection. This first step applies a linear transformation to the image; however, the local distortion within each frame needs to be corrected.

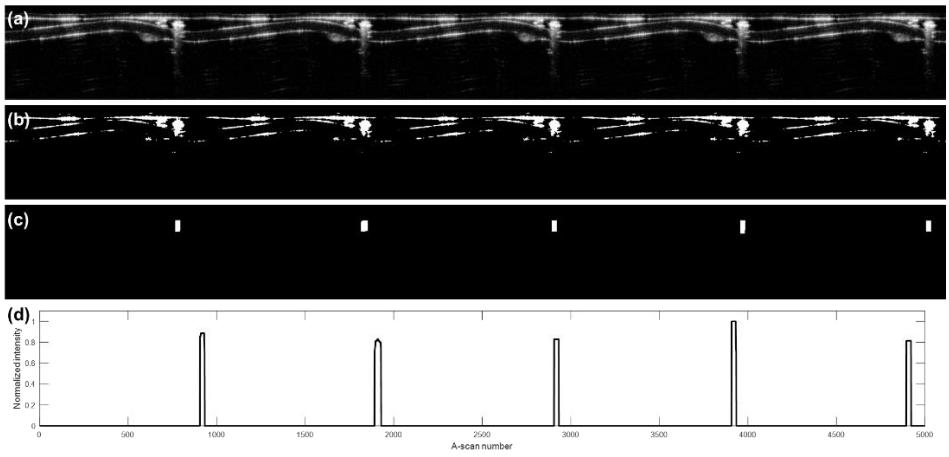

Figure 6.3 Image-based trigger generation in the proposed NURD correction algorithm. (a) Stitched OCT image of the sheath portion and after (b) binarization, (c) morphological operation. (d) The mean A-line intensity of the binarized image.

In the second step of the NURD correction algorithm, undersampled or oversampled regions within the image are identified based on dynamic programming (DP) segmentation of the sheath surface profile [105]. Then, a non-linear transformation is applied to correct the local distortion. This step takes advantage of the off-center positioning of the probe with respect to the outer sheath. As shown in **Figures 6.2(b) and (d)**, the resulting sheath surface profile in the polar image will follow a non-linear profile which can be used to identify and correct local image distortion. In this study, we defined a cumulative function S_i of i-th angular position as below:

$$S_i(\theta) = \sum_{i=1}^{\theta} (z_i(\theta) + \tau) \tag{6.2}$$

where $z(\theta)$ is the height position of the sheath surface at i-th angular position and τ is an arbitrary offset. In **Figure 6.4**, we describe two cases of image distortion. In the case described in the blue line, the motor rotates faster at first and then slower at the end. This will distort the image and the S(θ) function towards the left side. In the other case described in the red line, the motor rotates slower at the beginning and faster at the end. This will distort the image and the S(θ) function towards the right side. To correct the nonlinearity, the obtained plot is resampled to match the reference curve using linear interpolation. Offset is varied experimentally to adjust the amount of correction to apply. If the offset is too small, the algorithm will fail to scale the edge as the slope of the function will be close to zero. If the offset is too large, the algorithm will make less correction to the image since the cumulative plot will approach a linear function.

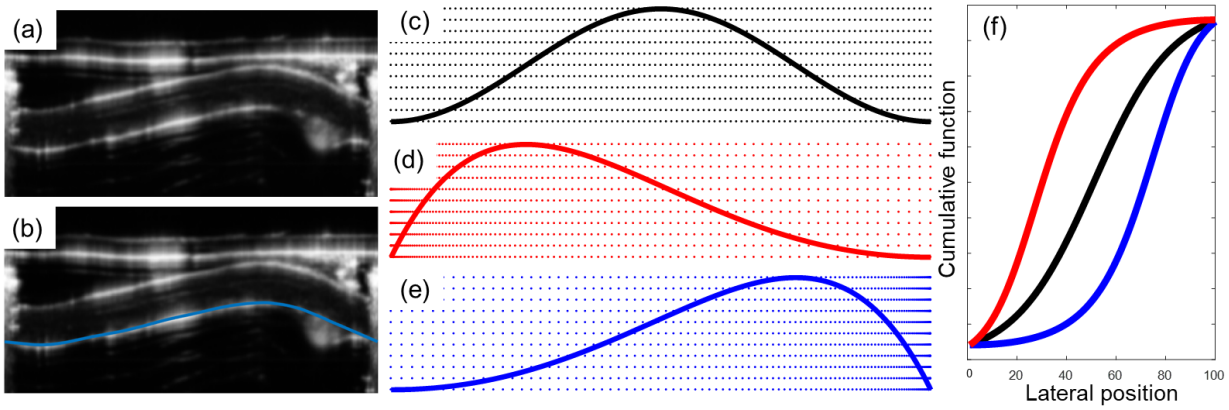

Figure 6.4 Characterization and correction of distortion through the nonlinear surface profiled of the sheath. (a) OCT image of sheath location, (b) segmentation of the sheath surface, (c) sheath surface profile without image distortion, (d,e) sheath profiled under NURD distortion, (f) cumulative function of the sheath profile without image distortion (black) and with image distortion (red and blue).

6.3.4 Evaluating the performance of the correction

To evaluate the effect of the NURD correction, we performed quantitative analysis on the M-B mode of the dynamic airway images. The M-B mode was created by resampling the 3D data set of polar OCT images so that the x-axis was the scanning angle and the y-axis was time in each image. Then, intensity projection was performed in the depth direction to obtain the summation of the pixel intensity. The M-B mode contained distinct edges created by the shadow cast on the tissue. Motion artifacts and NURD made the edge features discontinuous and deviate from a straight line. To obtain a quantitative assessment of the amount of image distortion, the deviation in the edge in time was calculated.

In addition, we estimated interframe intensity variance to assess the amount of motion in the B-scans. For this study, we selected 20 dynamic airway images during the resting state when there is no tissue movement. High interframe variance indicates the mismatch between the frames due to the image distortion or the motion artifacts. Here, the difference index is defined as follows:

$$D(\theta) = \frac{1}{M-1}\sum_{z=1}^{M}\left[\frac{1}{N-1}\sum_{i=1}^{N}(I_i(z,\theta) - \overline{I(z,\theta)})^2\right] \quad (6.3)$$

where M is the number of pixels in A-scan, N is the total number of B-scans, $I_i(z,\theta)$ is the pixel intensity at *i*-th frame, and $\bar{I}$ is the mean pixel intensity. Finally, the mean of the difference index at each A-line was evaluated.

6.3.4 Regional Compliance measurement

Dynamic OCT images contain information on temporally varying tissue deformation during a respiratory cycle. In this study, the variance of the tissue displacement at each angle position in the polar OCT image was calculated as regional airway compliance. A dynamic programming segmentation algorithm was used to identify the lumen-air boundary in each image and to track the tissue displacement movement. Here, we assumed the probe stayed in the same position during the dynamic airway measurement. The final regional compliance index (RCI) is defined as:

$$RCI(\theta) = \sum_{t=1}^{T}\left(u(t,\theta) - \overline{u(\theta)}\right)^2 \quad (6.4)$$

where T is the number of B-scans within the pre-set time window and w is a weight factor. In this study, T=200 since we processed 200 B-scan images.

6.4 Results and Discussion

6.4.1 Evaluation of NURD correction algorithm

We evaluated the effect of the NURD correction algorithm using the M-B mode projection view of 200 dynamic OCT images during a respiratory cycle (**Figure 6.5**). NURD distorts the polar images and shifts the lateral position of the tissue in the image as indicated by the red arrows. In the M-B mode projection, we found the edges near the adenoid portion can be easily

distinguished due to the shadows cast by the metal wire and the nasal hair. Therefore, we used this section of the image for evaluating the NURD correction. After the alignment process, the lateral motion is reduced. However, the first correction does not improve, if not worsen, the distortion in the center of the image. This confirms the necessity to apply the second NURD correction. After applying the nonlinear scaling based on the graph cut theory, the variance in the images was minimized in both the center and the edge.

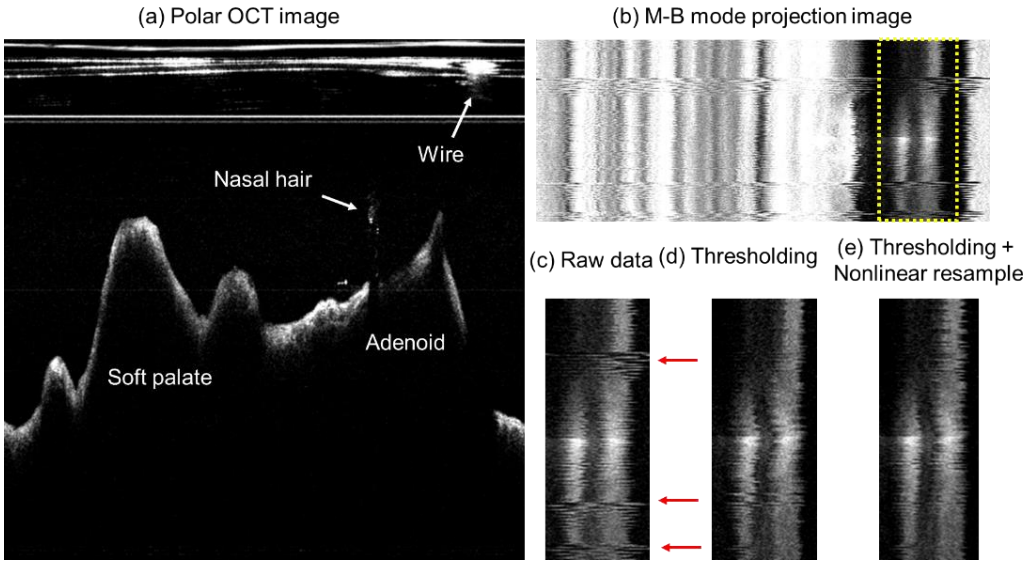

Figure 6.5 The effect of the NURD correction on the dynamic OCT images. (a) Polar OCT images, (b) M-B mode projection of the 200 dynamic OCT B-scan, (c) zoom in view of the yellow box in M-B mode, (d) after applying thresholding to align the image, and (e) after applying both thresholding and nonlinear resampling correction.

Next, we evaluated the accuracy using the interframe intensity variance method. The raw OCT B-scans before the NURD correction shows broadening in the edge features as well as the ghost image formed by the image distortion as indicated by the white arrow in **Figure 6.6(a)**. After applying the thresholding method and realignment of the images, the ghost image in the adenoid in the original image has improved. However, the image distortion of the center part of the image has become worse as indicated by the broadening in the edge features near the center region

[**Figure 6.6(b)**]. After realignment and nonlinear resampling, the image distortions are significantly reduced in both the center and peripheral part of the image [**Figure 6.6(c)**]. The improvement in the image distortion can also be confirmed from the decrease in the mean difference index over all the theta where $D_{raw} = 75 \pm 129$, $D_{threshold} = 58 \pm 74$, $D_{threshold} = 44 \pm 57$ [**Figure 6.6(d)**].

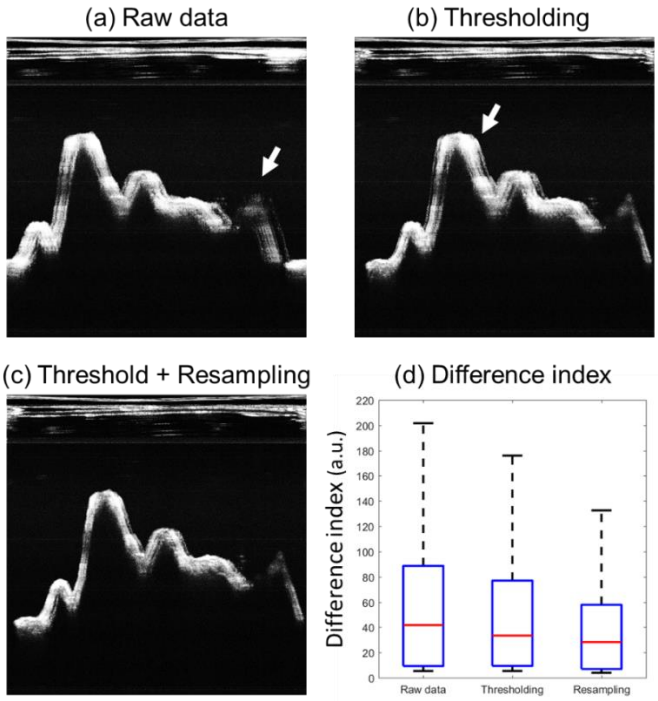

Figure 6.6 Projection view of pixel intensity variance across B-scan. (a) Raw data and after applying (b) thresholding and (c) nonlinear resampling. White arrows show the regions of image distortion. (d) Box plot of difference index.

6.4.2 Tissue displacement map and local compliance

Dynamic OCT imaging of a human nasopharynx was obtained during the inspiration of a respiratory cycle. **Figure 6.7** shows the intranasal pressure measurement from the pressure catheter placed in the nasal cavity. During inhalation, negative pressure will be generated in the airway and partially collapse the lumen. Since the anterior segment (soft pallet) consists of low elasticity material, there is little movement in response to the pressure changes. On the other hand, the

posterior segment (adenoid) in the nasopharynx consists of soft tissue and, thus, shows larger displacement.

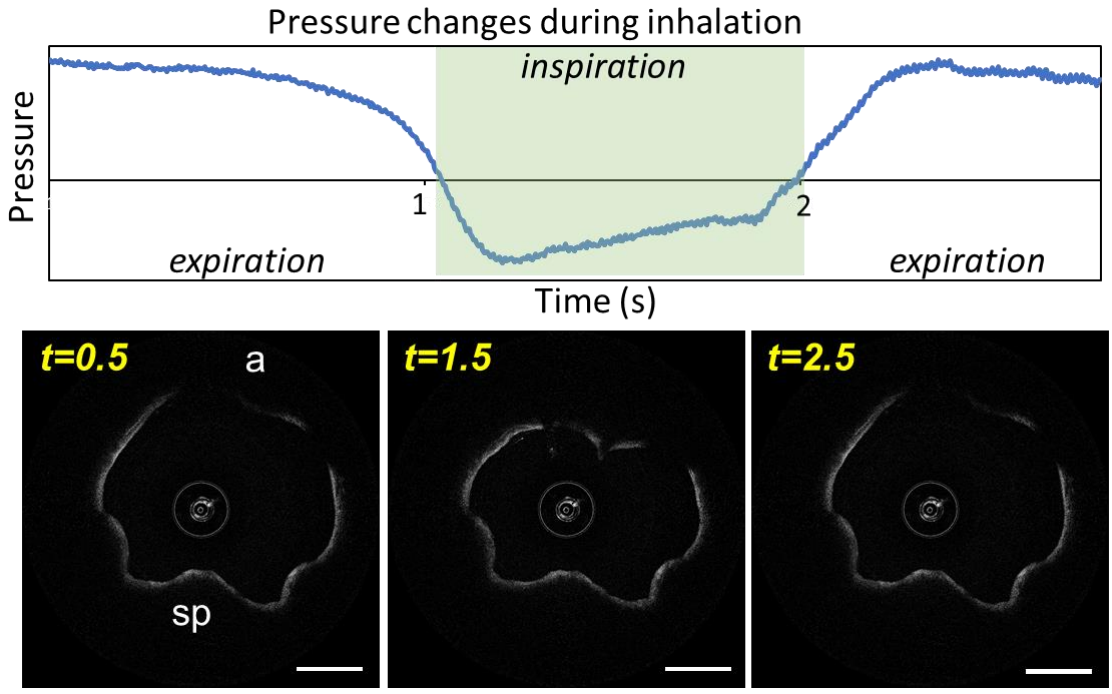

Figure 6.7 Pressure measurement and Cartesian OCT images of nasopharynx during a respiratory cycle. a: adenoid; sp: soft palate. Scale bar indicates 5 mm.

The intensity projection of the OCT images during inspiration shows tissue displacement. The displacement in the axial direction (red arrow) is caused by the airway deformation during pressure decrease. On the other hand, displacement in the lateral direction (blue arrow) is caused by the instability of the imaging probe rotation. In this paper, we corrected probe instability in post-processing and measured the angle-resolved airway compliance and the local tissue displacement towards the probe during a respiratory cycle.

Tissue surface was segmented using the same graph cut algorithm and plotted during inspiration. The 3D spatiotemporal map of the tissue surface shows the displacement in the tissue height from 800 to 1000 A-line location indicated by the arrow in **Figure 6.8(a)**. This location corresponds to the adenoid. The regional compliance index is calculated at each A-line location

by taking the variance of the axial displacement [**Figure 6.8(b)]**. As expected, the adenoid had high compliance compared to the surrounding tissue. Surprisingly, the compliance was not symmetric as the left side of the adenoid seemed to have higher compliance than the right side.

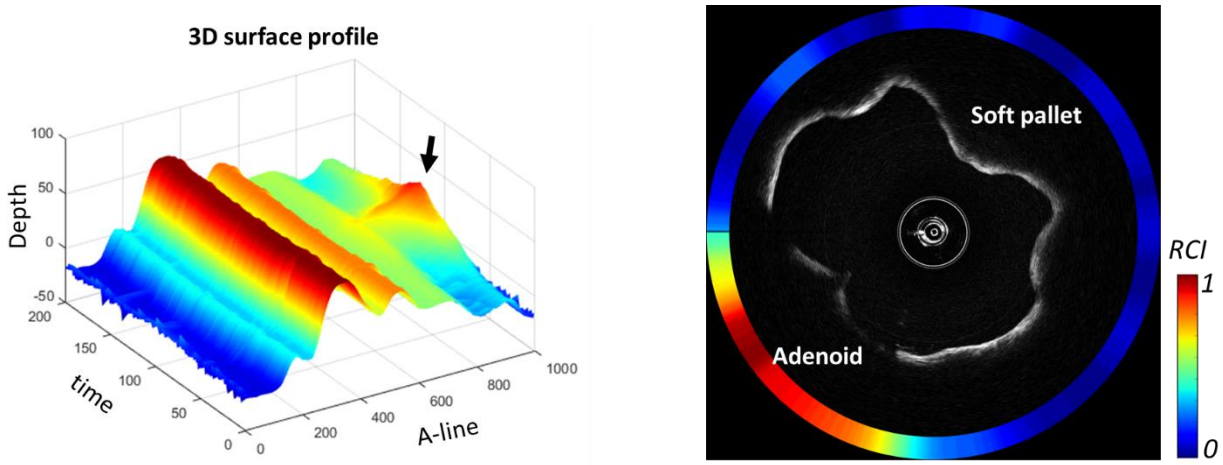

Figure 6.8 Regional compliance of Nasopharynx. (a) Displacement map and (b) relative regional compliance at each angle position.

5.5 Summary

We presented a new NURD correction technique that allows the correction of image distortion in a micromotor imaging probe. This technique does not rely on tissue contrast and only uses the information from the motor wire and the catheter sheath. The M-B mode projection view demonstrates the effectiveness of the proposed NURD correction technique. Furthermore, we constructed a regional compliance map based on the corrected images in the human nasopharynx. To the best of our knowledge, this is the first demonstration of *in vivo* elasticity measurement of the adenoid in an awake human using endoscopic OCT.

Chapter 7 – VISULIZATION OF CILIA SYNCHRONICITY AND BEATING FREQUNECY USING SPECTRALLY ENCODED INTERFEROMETRIC MICROSCOPY

7.1 Overview

Spectrally encoded interferometric microscopy (SEIM) is capable of detecting nanometer displacement at kilohertz frame rates by employing a rapidly wavelength-sweeping laser and a spectral disperser. In this study, we compared different SEIM processing algorithms based on Doppler shift and decorrelation for visualizing dynamic cilia movement. The effect of the frame acquisition rate was investigated to minimize the shot noise while maintaining sufficient imaging speed since SEIM has intrinsically low illumination power. We found that the Doppler method after the phase stabilization and the bulk motion correction provides the highest sensitivity for cilia beating measurement compared to the phase-resolve Doppler variance (PRDV) and intensity-based Doppler variance (IBDV) methods. The feasibility of the method was tested on a freshly excised rabbit trachea immersed in cell culture medium under a temperature-controlled environment. In addition to the cilia beating cycle, traveling waves caused by the coordinated cilia motion in an excised tissue were visualized for the first time. The results collectively demonstrate the potential clinical utility of this technique to monitor respiratory function and therapeutic effects.

7.2 Introduction

In the upper airway, healthy mucus and proper mucociliary transport are critical defenses

against airborne and aerosol transmissible pathogens. Being the most superficial layer in the upper airway, the mucus creates the first barrier that traps viruses, bacteria, and other foreign particles, preventing these pathogens from invading the lungs. Beneath the mucus are the cilia, surface organelles with a length of approximately 5-7 μm, and a diameter of less than 1 μm in the human airway [161, 162]. The motile cilium beats at 7-11 Hz in a healthy adult and is the primary mechanism that provides the kinetic force to proximally propel the mucus in order to expel the trapped pathogens out of the airway. Ciliary dysfunction can be from genetic defects or as a result of external trauma, such as toxic inhalation, leading to decreased ciliary beat frequency, irregular beat pattern, desynchronized metachronal wave. This can quickly develop into a vulnerability for both acute and chronic diseases, including cystic fibrosis (CF), asthma, chronic obstructive pulmonary disease (COPD), and primary cilia dyskinesia (PCD). Despite playing a crucial role in immune response, the clinical imaging tool that can accurately and effectively capture the structure and function of respiratory cilia is currently lacking. The main challenge with visualizing cilia motion is that it requires both micrometer spatial resolution and high imaging speed. In addition, the imaging tool needs to be in reflectance mode to capture the intact cilia attached to the tissue.

OCT is an interferometric-based imaging technique that uses reflected light from a sample to reconstruct a high-resolution cross-sectional image [163]. Since the contrast in OCT imaging is derived from backscattered photons, the imaging technique offers an ideal solution to the noninvasive visualization of cilia in a native airway. Due to these attractive features, there is considerable interest in quantifying functional image-based metrics relevant to mucus transportation dysfunction using OCT [164–170]. OCT was used to visualize flow profile generated by motile cilia by introducing polystyrene beads and tracking their trajectory, which provided insight to the clearance of mucus [171, 172]. Oldenburg et al. described a method to

characterize cilia beating frequency (CBF) by decorrelating the speckle pattern in time using cultivated primary human bronchial epithelial (hBE) cells [173]. Wang et al. further expanded the speckle decorrelation approach and characterized CBF in *in vivo* mouse oviduct [174]. Liu et al. developed a technique called micro-optical coherence tomography (μOCT) that uses an ultrawideband supercontinuum source to visualize the ciliary stroke pattern at a 1-um axial resolution [175]. The μOCT has recently been utilized in a clinical study to determine imaging-related metrics for the pathophysiology of cystic fibrosis through the nasal passage of awake humans [164]. Although all of these methods have their merits, the clinical utility of these approaches is limited as no single method can characterize the complete characteristics of cilia dynamics. The beads tracking method requires exogenous contrasts, which limits the *in vivo* application. The speckle decorrelation method, although providing a semi-quantitative CBF information, does not provide information on cilia synchronicity. Finally, μOCT is hard to implement in the clinic since the ultra-broadband supercontinuum source is expensive and bulky compared to other OCT light sources. In addition, μOCT often suffers from chromatic aberration from the wide bandwidth of the light source.

The phase-resolved Doppler approach has been recently proposed by our group to quantitatively assess the ciliary motion [168–170]. In the phase-resolved Doppler method, the Doppler shift in the back-scattered light during the cilia stroke cycle is detected as a phase shift in the interferometer. Then, the spectral interferogram can be analyzed to quantify the cilia beating pattern and CBF at each scanning location. Jing et al. first implemented a swept-source OCT microscopy system for visualization of CBF and the directionality of the ciliary beating from the Doppler phase shifts in an *ex vivo* rabbit trachea. Taking advantage of the fast imaging speed of a swept source OCT system, Doppler signals from tracheal cross-sectioning containing ciliated

epithelium can be acquired at up to 400 frames-per-second. In addition, a large portion of the acquired image is background since the ciliated layer is typically less than 10 μm in thickness [176]. To overcome this limitation, He et al. expanded the Doppler-based cilia visualization by applying the concept of spectrally encoded confocal microscopy proposed by Tearney in 1998 [168, 170, 177]. In this approach, the fast scanning axis is replaced by a series of focused light where each point corresponds to different wavelengths, as illustrated in **Figure 7.1**. This allows the scanning of the two-dimensional space at 2-3 orders of magnitude faster than conventional OCT scanning by sacrificing the depth scanning. The phase-resolved spectrally encoded interferometric microscopy (SEIM) approach revealed the two-dimensional spatial mapping of the CBF as well as the beating synchronicity [168, 170]. However, the effect of different processing algorithms on the ciliary motion detected by SEIM has not been previously investigated.

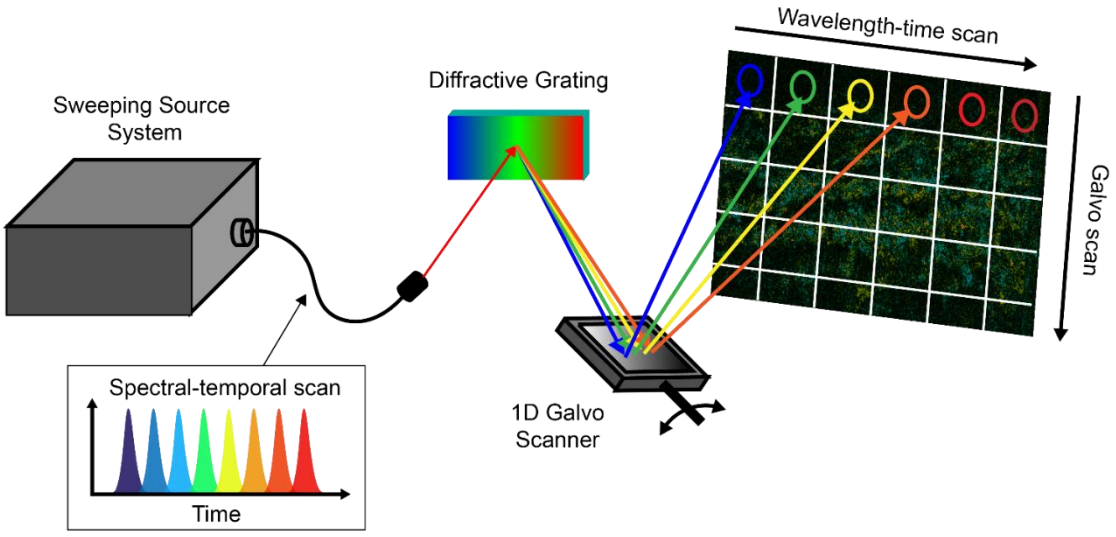

Figure 7.1 Principle of spectrally encoded imaging using a rapidly wavelength sweeping laser and a diffractive grating.

In this study, the beating pattern of cilia was quantified through the interframe phase-resolved Doppler (PRD), phase-resolved Doppler variance (PRDV), and intensity-based Doppler

variance (IBDV) approaches. The effects of frame acquisition speed were investigated. To demonstrate the feasibility of our method, we evaluated the healthy cilia and fixed cilia as a negative control.

7.3 Methods

7.3.1 Spectral-encoded Interferometric Microscopy (SEIM)

An SEI microscope was constructed using a vertical-cavity surface-emitting laser (VCSEL) as the light source, as illustrated in **Figure 7.2**. The VCSEL has a center wavelength of 1,310 nm, a bandwidth of 100 nm, and a repetition rate of 100 kHz. In the fiberoptic-based Mach-Zehnder interferometer, a 90:10 coupler splits the laser output into the sample and the reference arm, respectively. A circulator is used in each arm to direct the illumination light to the sample or reference mirror and the returning light to a 50:50 coupler, which generates the interferogram. In the sample arm, once the light from the optical fiber is collimated, a transmission diffraction grating spatially disperses the illumination light into different wavelengths where each wavelength encodes a successive location on a transverse line (x-scan). *En face* scanning is achieved by using a galvanometer mirror interposed between the first 4F (L1 pair) relay lens to move the spectrally dispersed line illumination across the imaging field in the slow axis. The L1 pair consists of achromatic doublets with a focal length of 35 mm. The second 4F (L2 pair) acts as a beam expander as the focal length of L2 is 35 mm and L2' is 50mm, which fills the entrance pupil of the objective lens to achieve high lateral resolution. Driven by a sawtooth waveform, the galvanometer operates at either 50, 100, or 200 Hz. A 20 × apochromat objective lens with a 0.40 numerical aperture (MY20X-824, Mitutoyo Corporation, Japan) is used for providing a high lateral resolution necessary to visualize the micromotion induced by cilia. The reference arm consists of

compensating windows for offsetting dispersion and a gold mirror. The interferograms generated by the returning reference and sample signals were converted into electrical signals via a balanced photodetector and then detected using a waveform digitizer. The digitized signals were transferred into a computer for processing. The system had a 550×550 μm field of view and a lateral resolution of 1.7 μm. An image of a 1951 USAF resolution target is shown in **Figure 7.3** where Element 2 of Group 8 can be resolved. The sample illumination power was 3 mW.

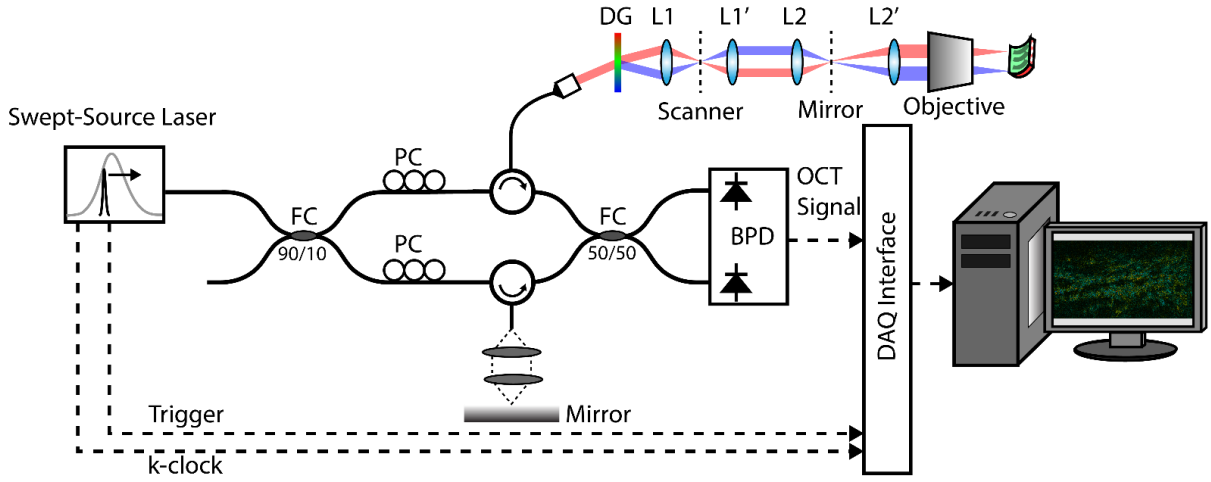

Figure 7.2 Schematic of SEIM system and the sample arm configuration. PC: polarization controller; FC: fiber coupler; BPD: balanced photodetector; L: lens.

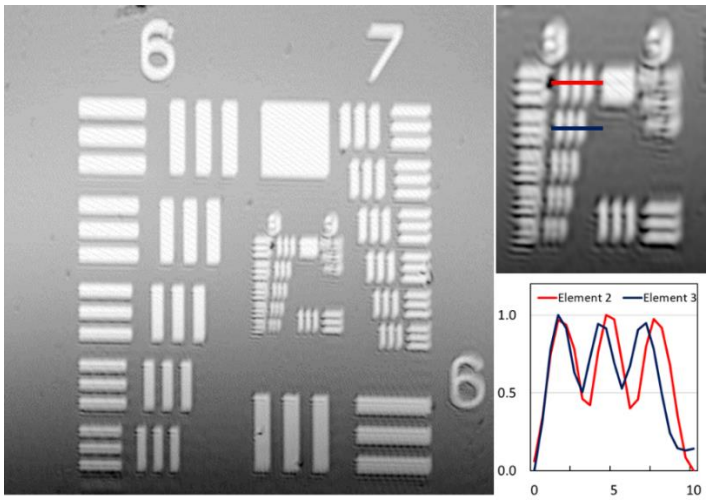

Figure 7.3 1951 USAF resolution target imaged with our SEIM system.

7.3.2 Tracheal Sample Preparation

Using a rabbit model, we obtained the tracheal sample from a healthy New Zealand white rabbit (male, 4 kg). The tracheal sample was excised immediately after the animal was euthanized with Euthasol injection. All procedures were reviewed and approved by the Institutional Animal Care and Use Committee at the University of California, Irvine prior to the experiment. The excised trachea was dissected into ~5-mm segments then sectioned diametrically to expose the mucosa. For microscopy, the sectioned tissue was mounted onto a silicone-filled petri dish with the center area depressed. The depressed region provided the chamber for housing the tissue and allowed for submersion of CO_2 independent phosphate-buffered saline solution. A microscope cover glass was placed on top of the silicone to ensure a flat sample surface for SEI imaging and to also minimize the motion from the water surface. This setup is illustrated in **Figure 7.4**. SEI imaging was performed under room temperature and on an anti-vibration optical table.

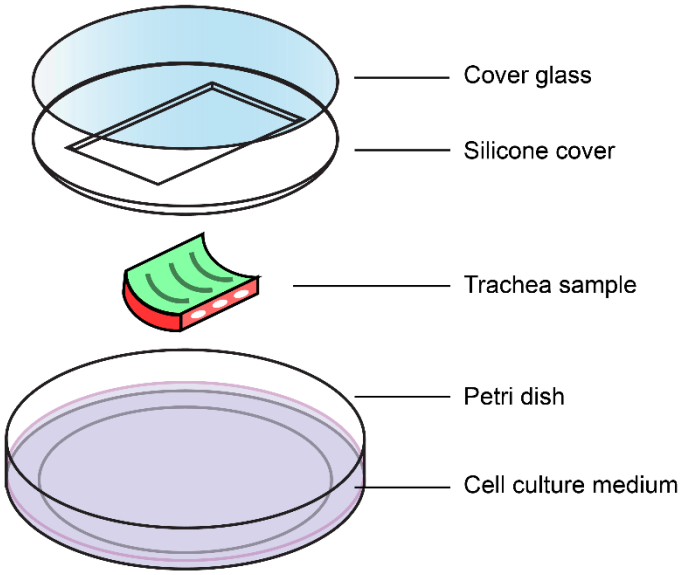

Figure 7.4 Sample setup for SEIM imaging. The excised tissue is placed inside a custom-designed petri dish chamber.

7.3.3 Doppler and decorrelation algorithms

Processing algorithms based on phase-resolved Doppler (PRD), phase-resolved Doppler variance (PRDV), and intensity-based Doppler (IBD) variance methods were systematically compared for OCT angiography [178]. In this study, we compared the three processing methods for characterizing cilia functions. Briefly, PRD can be described through the autocorrelation:

$$f' = \frac{1}{T}\arctan\left[\frac{\mathrm{Im}\left(A_{j+1,z}\right)\mathrm{Re}\left(A_{j,z}\right) - \mathrm{Im}\left(A_{j,z}\right)\mathrm{Re}\left(A_{j+1,z}\right)}{\mathrm{Re}\left(A_{j,z}\right)\mathrm{Re}\left(A_{j+1,z}\right) + \mathrm{Im}\left(A_{j+1,z}\right)\mathrm{Im}\left(A_{j,z}\right)}\right] \tag{7.1}$$

where f' denotes the Doppler frequency, T represents the time interval between adjacent A-lines, and A is the complex OCT data at j^{th} A-line and z^{th} depth point. PRD is most sensitive when the flow direction is the same as the detection beam whereas the variance approaches are ideal for evaluating flow direction that is near perpendicular to the detection beam. PRD variance can be calculated by taking the square of σ, the standard deviation of the Doppler spectrum:

$$\sigma_{PRD}{}^2 = \frac{1}{T^2}\left[1 - \frac{\left|A_{j,z}A^*{}_{j+1,z}\right|}{\frac{1}{2}\left(A_{j,z}A^*{}_{j,z} + A_{j+1,z}A^*{}_{j+1,z}\right)}\right] \tag{7.2}$$

where A^* is the complex conjugate of A. By only taking the amplitude information, which is particularly advantageous when the imaging system experiences phase instability, IVD variance can be determined:

$$\sigma_{IBD}{}^2 = \frac{1}{T^2}\left[1 - \frac{\left|A_{j,z}\right|\left|A_{j+1,z}\right|}{\frac{1}{2}\left(\left|A_{j,z}\right|^2 + \left|A_{j+1,z}\right|^2\right)}\right] \tag{7.3}$$

Practically, averaging between neighboring pixels can be performed to improve the signal-to-noise ratio (SNR) such that:

$$\bar{f}' = \frac{1}{T}\arctan\left[\frac{\sum_{j=1}^{J}\sum_{z=1}^{Z}\mathrm{Im}\left(A_{j+1,z}\right)\mathrm{Re}\left(A_{j,z}\right) - \mathrm{Im}\left(A_{j,z}\right)\mathrm{Re}\left(A_{j+1,z}\right)}{\sum_{j=1}^{J}\sum_{z=1}^{Z}\mathrm{Re}\left(A_{j,z}\right)\mathrm{Re}\left(A_{j+1,z}\right) + \mathrm{Im}\left(A_{j+1,z}\right)\mathrm{Im}\left(A_{j,z}\right)}\right] \tag{7.4}$$

for PRD variance

$$\bar{\sigma}_{PRD}{}^{2} = \frac{1}{T^2}\left[1 - \frac{\left|\sum_{j=1}^{J}\sum_{z=1}^{Z}A_{j,z}A^{*}{}_{j+1,z}\right|}{\frac{1}{2}\left(\sum_{j=1}^{J}\sum_{z=1}^{Z}A_{j,z}A^{*}{}_{j,z} + A_{j+1,z}A^{*}{}_{j+1,z}\right)}\right] \tag{7.5}$$

and for IBD variance

$$\bar{\sigma}_{IBD}{}^{2} = \frac{1}{T^2}\left[1 - \frac{\sum_{j=1}^{J}\sum_{z=1}^{Z}\left|A_{j,z}\right|\left|A_{j+1,z}\right|}{\sum_{j=1}^{J}\sum_{z=1}^{Z}\frac{1}{2}\left(\left|A_{j,z}\right|^{2} + \left|A_{j+1,z}\right|^{2}\right)}\right] \tag{7.6}$$

where J and Z denote the number of A-lines and depth points, respectively, that are averaged. Here, to obtain the optimal SNR while maintaining reasonable computing time and resolution, we empirically used the window size of $J = 9$ and $Z = 9$ for processing the 2000 × 2000 complex matrix.

7.3.4 Data Processing Flow

Figure 7.5 shows the workflow of data processing. The spectral interferogram data was processed using a MATLAB code to obtain either the phase or decorrelation images. The DC terms were first subtracted from the fringe signal. After the background subtraction, the signals were converted to an analytical signal by performing Hilbert transformation. The amplitude values of the complex analytical signals were used to calculate the reflectivity image, which is analog to *en face* OCT images. For phase-resolved Doppler, Eq. (7.4) is used to calculate the interframe phase differences. Then, the bulk motion is corrected by performing A-line normalization of phase value and the moving average of the temporal phase as shown in the equation below:

$$\Delta\varphi' = \sum_{i=0}^{M-1} (\Delta\varphi_{j,z}(t + i \cdot \Delta\tau) - |\overline{\Delta\varphi_j}|) \tag{7.7}$$

where M is the number of frames for temporal averaging, $\Delta\tau$ is the time interval between each frame, and $\overline{\Delta\varphi_j}$ is the mean phase at *j-th* A-line. For PRDV and IBDV methods, Eq. (7.5) and Eq. (7.6) were used to calculate the decorrelation signals. For all the methods, an intensity thresholding was applied based on the amplitude values to eliminate noise. Once the PRD or decorrelation images are reconstructed, they can be converted into spatial-temporal images from the *en face* images in order to visualize the cilia beating pattern [169].

Finally, the shift in the phase can be converted to the distance, Δz, using Eq. (7.8):

$$\Delta z = \frac{\Delta\varphi \cdot \lambda_0}{2\pi \cdot n} \tag{7.8}$$

where $\Delta\varphi$ is the phase shift, λ_0 is the center wavelength of the laser, and $n = 1.33$ is the refractive index of the mucosal layer. By taking the variance of the intensity and the phase shift, the local fluctuation caused by the ciliary motion can be identified. The dominant frequency at each pixel within the field of view was determined, allowing the mapping of ciliary beat frequency across the tissue.

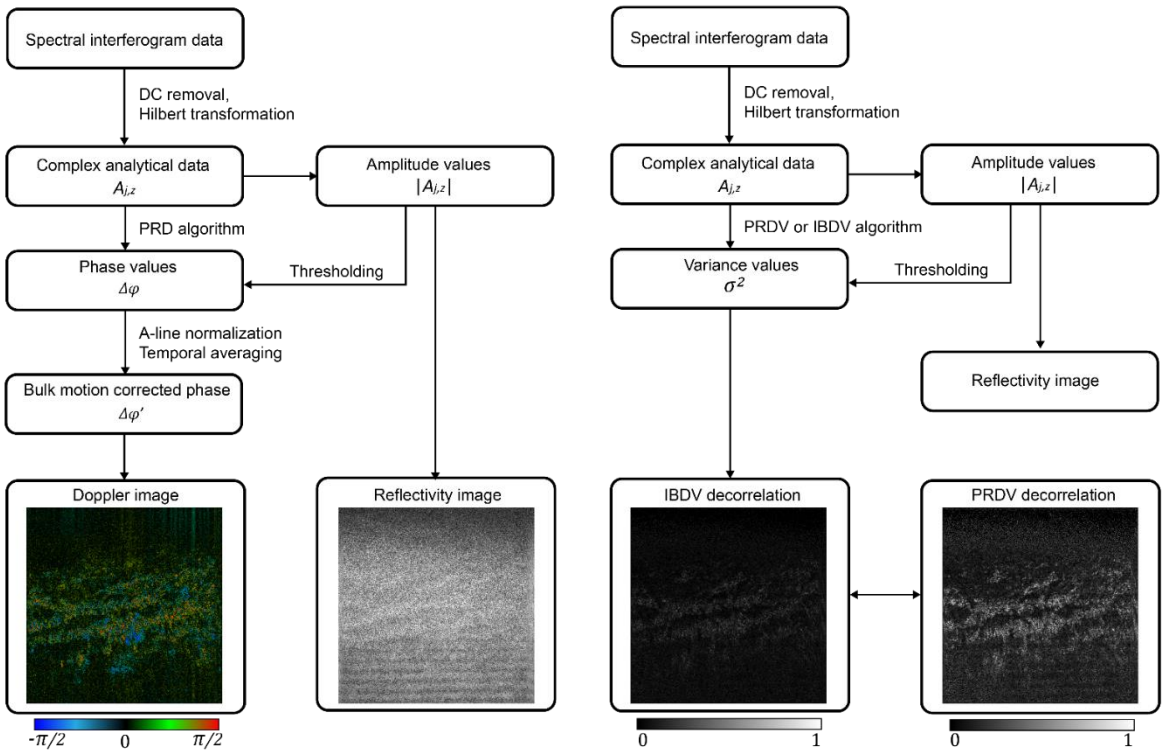

Figure 7.5 Data processing flowchart for SEIM imaging.

7.4 Results

7.4.1 Phase stabilization

To characterize the phase stability of our SEIM system, a static mirror was placed at the sample position, and the phase differences between the adjacent A-line scan were obtained. A total of 500 A-lines was obtained at the same scanning location in order to separate the stability caused by the galvo scanner. In this study, a wavelength trigger was used to synchronize the laser sweeping. However, edge collision between the k-clock and the trigger signal could cause instability in the phase as described in our previous study [179]. The effect of edge collision can be visualized as a sudden jump in the phase value [**Figure 7.6(a)**]. The first 2000 points can be identified as a valid sampling region since the sample beam was being partially cut off by the

entrance pupil of the objective lens. The histogram of phase difference distribution within the valid region shows a Gaussian-like profile with side lobes before phase stabilization. The phase stability was improved by adding a small delay to either the trigger or k-clock signal using a short coaxial cable. After the phase stabilization, the phase map shows a clean background signal without sudden phase jittering and the histogram shows a Gaussian-like profile without side lobes [**Figure 7.6(b)]**. Typically, the phase stays stable for at lease 4~5 hours before the calibration is needed.

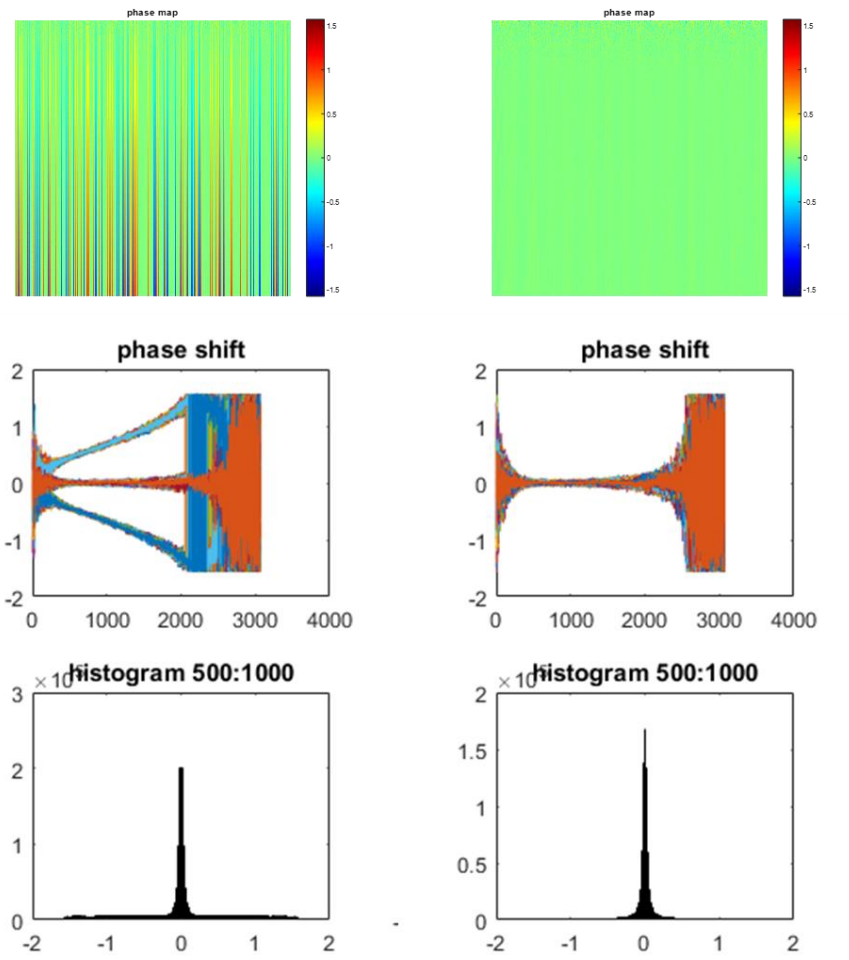

(a) Before phase stabilization (b) After phase stabilization

Figure 7.6 Phase stabilization by avoiding edge collision of the k-clock signal.

7.4.2 Effect of image acquisition speed

To characterize the effect of image acquisition speed, the variance of the reflectance images

is used to compare the signal-to-noise ratio when the images are acquired at 50 Hz, 100 Hz, 200 Hz, and 400 Hz. The main reason for the signal degradation at a higher acquisition rate in the SEIM system is the shot-noise due to the low photon collection efficiency. We found more than a 3 dB signal attenuation from the transmission grating and the objective lens. Increasing the source power by optical amplifier can reduce the shot noise but the intensity noise will be increased. Since amplitude is less sensitive to the bulk motion, we used the decorrelation image from the reflectance image as a metric to quantify the amount of shot noise at different image acquisition rates. This processing can be considered as the temporal variance of the IBDV images when the processing window size is a 1-by-1 pixel and is the fastest way to obtain contrast from the speckle fluctuation.

We acquired 100 reflectance images at different image acquisition rates. Then, 10 reflectance images were selected based on the constant time interval of 25 ms for processing the speckle decorrelation. For example, we selected the first 10 data for the 400 Hz image acquisition rate. For the images acquired at 200 Hz, every other image in the first 20 data were selected for the calculation. Then, the variance of the 10 images was calculated to create a single projection image of 800-by-800 pixels. As shown in **Figure 7.7(a)**, the imaging region contains motile cilia that have a higher variance; 100-by-100 windows of the signal and the background were used to estimate the SNR. The location of the window was kept constant for all the data sets for consistency. Here, SNR is defined by:

$$SNR = \frac{\langle {\sigma_{signal}}^2 \rangle}{\langle {\sigma_{background}}^2 \rangle} \tag{7.8}$$

where $\langle \quad \rangle$ indicates the mean pixel intensity within the selected window. **Figure 7.7(b)** shows poor signal-to-noise ratio at high frame acquisition rates more than 100 Hz due to the low photon counts. We decided to use a 50 Hz frame rate in this study to obtain high SNR images while

maintaining the sufficient acquisition speed for visualization of cilia dynamics.

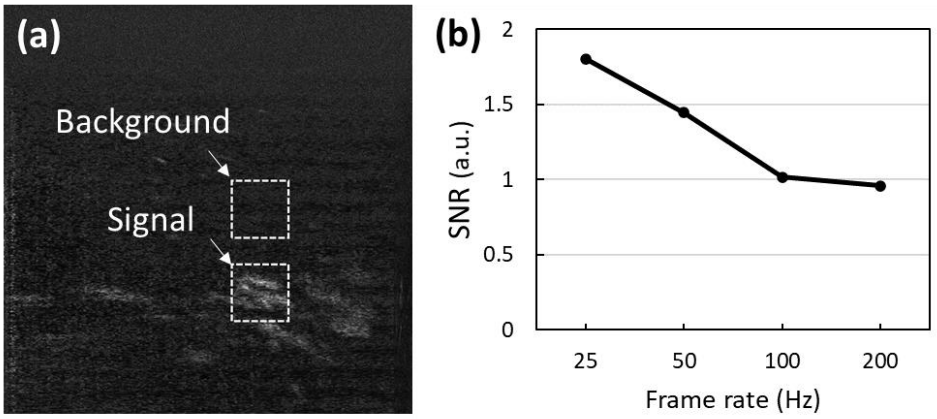

Figure 7.7 The effect of image acquisition rate on the image quality. (a) Intensity variance image showing the selected window for the signal and the background quantification. The image is the variance of 10 images acquired at a 200 Hz frame rate. (b) Signal-to-noise ratio at different frame rates.

7.4.3 *Ex vivo* tracheal tissue imaging

Figure 7.8 shows the representative results of motile cilia images from a healthy rabbit trachea. IBVD and PRDV images show the reflectance and phase fluctuation induced by the cilia motion. The PRD images reveal the beating direction of the cilia in addition to the regions of active cilia where the motion towards the detection beam is denoted as red and away as blue. **Figures 7.8 (e-h)** show the variance of 20 images processed with each method to characterize the sensitivity of the cilia detection. While IBVD and PRVD have similar contrast in the variance images, PRD images appear to show finer details in the image. Since the same window size was used in all the methods, PRD may provide higher specificity in terms of characterizing the trajectory of the cilia. Another possible reason is that IBVD and PRVD may contain the information of transverse cilia motion while PRD is most sensitive to the vertical cilia movement that aligns with the beam direction. **Table 7.1** shows that the PRD method has the highest signal-to-noise ratio of all the three processing methods.

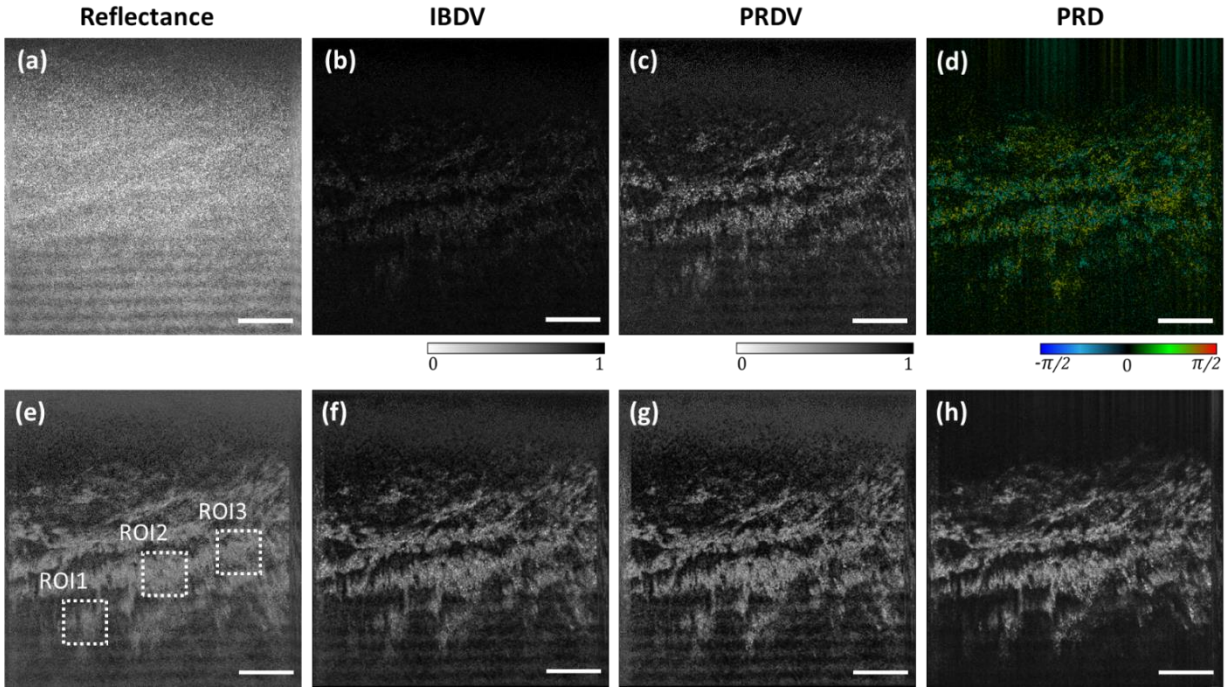

Figure 7.8 Doppler and decorrelation images of respiratory cilia: (a) reflectance image, (b) IBDV image, (c) PRDV image, (d) PRD image, and (e-h) the variance of 20 consecutive images using different processing techniques. Scale bar indicates 100 μm.

Table 7.1 Comparison of SNR

		IBDV	PRDV	PRD
SNR	ROI 1	1.59	1.71	1.81
	ROI 2	2.62	2.77	3.59
	ROI 3	2.17	2.20	2.99

7.4.4 Spatial-temporal analysis of cilia beating

The cilia beating pattern can be determined and mapped using spatio-temporal analysis of the time-series Doppler images at each pixel (or region of interest). In the spatio-temporal plot, the y-axis represents the wavelength and the x-axis represents time. **Figures 7.9 (a) and (b)** reveal the location dependency of ciliary beat frequency, ranging from 2.0 to 4.1 Hz. **Figure 7.9 (c)** shows the Fourier transformation of the blue and red lines in the spatio-temporal map after applying a fast Fourier transform. This finding is consistent with our previous finding that ciliary beat

frequencies may vary between patches[170]. In addition, it appears the frequency difference creates the directionality in the cilia movement which resembles the metachronal waves reported previously. The wave propagation speed can be estimated by measuring the slope as indicated by the yellow arrows in **Figure 7.9 (b)**. The speed of the wave was estimated to be ~270 μm/s, which matches well with the metachronal wave speed in the cell culture [180]. To the best of our knowledge, this is the first demonstration of metachronal waves in an excised tracheal tissue. Further investigation is needed to understand if the frequency mismatch observed here is the causation of the metachronal waves.

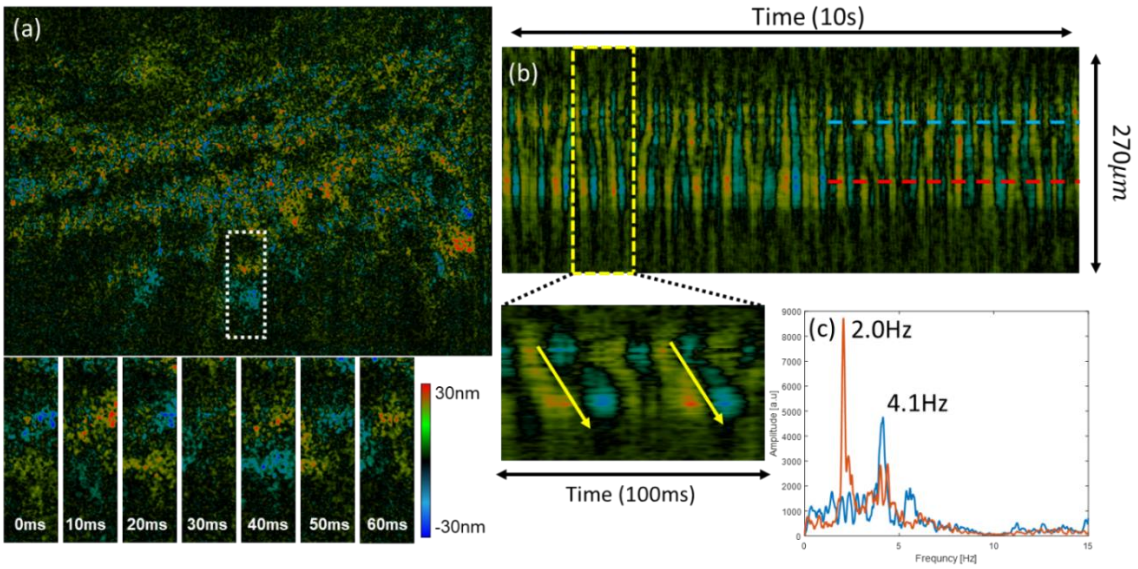

Figure 7.9 PRD image of an ex vivo rabbit trachea and the spatial-temporal analysis. (a) phase map, (b) spatio-temporal map of the white box region, (c) power spectrum of the upper and lower cilia.

6.5 Discussion

In this study, an SEI microscope was constructed to evaluate cilia dynamic movement. Since the SEIM system operates at a much faster imaging speed compared to the point-by-point scanning approach used in the conventional OCT and the confocal microscopes, it is able to visualize wide-field displacement at a few hundred-hertz frame rate. In addition, the Doppler shift

can be detected at nanometer sensitivity using the interferometric technique.

As Doppler shift and Doppler variance rely on phase measurement, the phase stability must be optimized to achieve high detection sensitivity. In our SEI system, data acquisition via the waveform digitizer is k-clocked such that the sample points are equally spaced in wavenumber. Additionally, the electrical and optical signals are properly delayed using our previously proposed method [179] to ensure the necessary phase performance. It is also possible to adopt a common-path detection approach by replacing the microscope cover glass which encloses the tracheal sample with a wedged window [181]. A common-path setup can scale down the footprint as well as ease of use of the device, making the clinical translation more feasible. Since practical applications of SEI will take place in a clinical environment, the development of SEI endoscopy will stimulate the translation. Quantification of ciliary beat frequency *in vivo* using OCT has been recently demonstrated[182], but it is limited to a one-axis scan and provides only cross-sectional imaging of the mucosa. The proposed SEI microscopy has the potential to be transformed into a rigid endoscope form factor.

In conclusion, in this report, we described an SEI microscope with a processing scheme for studying the beating frequency, direction, and pattern of collective cilia motion. While the imaging system cannot resolve individual cilium, it can detect the motion-induced signal fluctuation through interferometry. Compared to its OCT counterpart, the improved imaging speed enables functional extensions that provide additional information on cilia physiology. This has promising applications for investigating the effects of other common toxic gases and aerosolized agents on cilia health. As SEI microscopy may be further developed into the form of an endoscope, the ability of quantifying ciliary function *in vivo* would provide valuable measures for assessment and treatment of patients with cilia pathology.

Chapter 8 – VISUALIZING BIREFRINGENCE CHARACTERISTICS USING POLARIZATION SENSITIVE OCT

8.1 Overview

PS-OCT is another major function imaging technique based on OCT. PS-OCT is capable of visualizing and quantify the material birefringence. Birefringence is the property of a material to alter the polarization state of the light. Typically, PS-OCT requires complex setups with additional detector and careful calibration of the polarization state of the incident beam, which requires significant modification of the OCT system and high building costs. We present a very simple method of constructing a PS-OCT system. An ordinary fiber-based swept-source OCT system was reconfigured for PS-OCT by adding a long section of polarization-maintaining (PM) fiber in the sample arm. Two polarization modes of a large group-delay difference formed spatially distinguished polarization channels. The depth-encoded information on the polarization states could be retrieved by an amplitude-based analysis. We found our method provides an economic scheme of PS-OCT. It demonstrated that an ordinary OCT system can be easily reconfigured for PS-OCT imaging if it has sufficient margins in the imaging range. In addition, this chapter is adopted with permission from [183] © The Optical Society.

8.2 Background and Motivation

PS-OCT provides a variety of opportunities in tissue imaging with its unique capability of acquiring depth-resolved sample birefringence or other polarization properties [184–187]. However, difficulties in system implementation and management are major obstacles in clinical applications. Bulk-optic construction of PS-OCT, frequently used in earlier development [188], is

not compatible for a majority of fiber-optic technologies. Various techniques have been developed so far for fiber-based construction of PS-OCT systems with PM fibers or common single-mode (SM) fibers [33, 189, 190]. In one of the schemes [191, 192], a swept-source OCT (SS-OCT) system based on SM fibers equips a passive delay unit (PDU) which produces polarization-dependent delays of the OCT signal. The PDU is made of bulk-optic elements or simply a long section of PM fiber. Detected by a pair of balanced photodetectors for polarization-channeled signal acquisition, full polarization information can be obtained with two polarization states incident on the sample in the PDU-based PS-OCT system. With help from auto-calibration techniques, such a system is designed to operate robustly against systematic polarization variations. However, it requires a specialized design with added system complexity. There are several cost-effective approaches based on single cameras for spectral-domain OCT (SD-OCT)[193–195]. But they still require special configurations in the spectrometer designs or the synchronized operation of polarization modulators.

In many cost-sensitive applications, such an elegant but complicated approach is not available. There is a demand for low-cost and ready-to-use technologies that can take advantage of the present OCT systems while tolerating some incomplete features of simpler PS-OCT systems. Taking aim at those demands, we studied an economic scheme of re-configuring an ordinary OCT system to a PS-OCT variant. In our novel scheme, a long section of PM fiber is inserted at the sample arm of the OCT interferometer for polarization-dependent delays of a large retardation. The resulting OCT image contains a plurality of image replicas separated by the group delay difference of the polarization modes. The polarization-sensitive interference can be analyzed by the difference between the replicated images. By this scheme, any ordinary OCT system can be

easily upgraded to add a useful PS-OCT imaging function if it supports a sufficiently long imaging range.

Constructing depth-encoded polarized detection channels for PS-OCT is not a novel approach [196]. Use of a long PM fiber or any type of a passive delay unit can be considered instead of using a pair of photodetectors arranged for different polarization channels. This requires a means of polarization controls which manages the input polarization state. It may unexpectedly increase the system complexity. In Rivet *et al.*'s demonstration of a simple PS-OCT system [196], a bulk-optic module of a large retardation was utilized for depth-encoded polarization detection. Their scheme, however, employs a polarizer in their passive optical module for a controlled polarization state which complicates the optical design for non-reciprocal operation.

In this study, we report on a very simple method of PS-OCT system configuration based on a delay PM fiber.

8.3 Methods

8.3.1 Polarization-Sensitive OCT Design

Figure 8.1 shows the schematic diagram of our PS-OCT system. It was based on an ordinary SS-OCT system operating at a center wavelength of 1.3 μm. A MEMS-VCSEL (SL131090, Thorlabs Inc.) was used for the swept source. The full optical bandwidth was 100 nm. It provided a wide imaging range of 12 mm with low sensitivity roll-offs of less than 3 dB. The system was operated at an A-line rate of 100 kHz with a signal sampling rate of 4.0 GS/s. The only modification we made to the previously constructed ordinary OCT system was to add a 12-meter long PM fiber (PM1300-XP, Thorlabs Inc.) at the SM fiber's end of the sample arm. An SM fiber patch cable of the same length was inserted in the reference arm to match the optical path length.

A quarter-wave plate (QWP) was placed right before the objective lens. Not shown in the figure, the clock signal output of the swept source was also delayed with a 30-meter long coaxial cable. The purpose of using the long SM fiber patch cable and the coaxial cable delay was to match the overall signal delay. Those modifications of the system can be implemented with ease to any SS-OCT system. Note that the light of the swept source is assumed to be naturally polarized. Otherwise, a polarizer can be installed at the output of the light source.

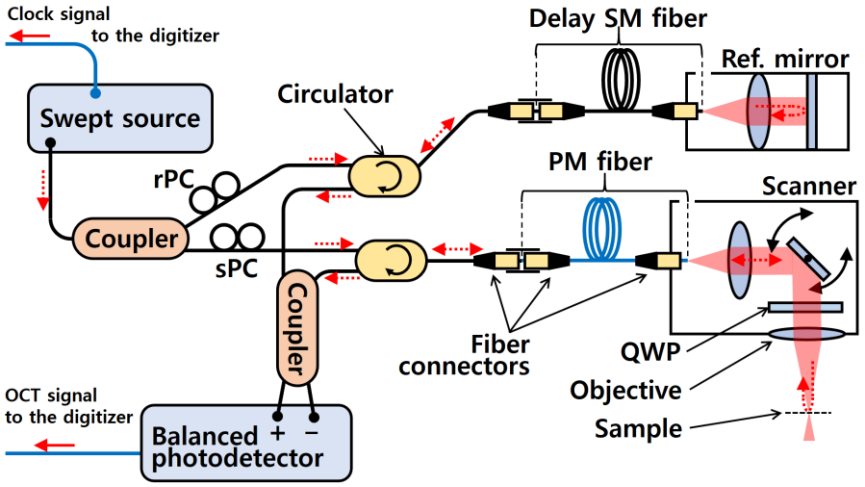

Figure 8.1 Schematic of our PS-OCT system. A long section of PM fiber is placed at the sample arm while an SM fiber section of the same length is added at the reference arm. The rest of the fibers are all SM fibers.

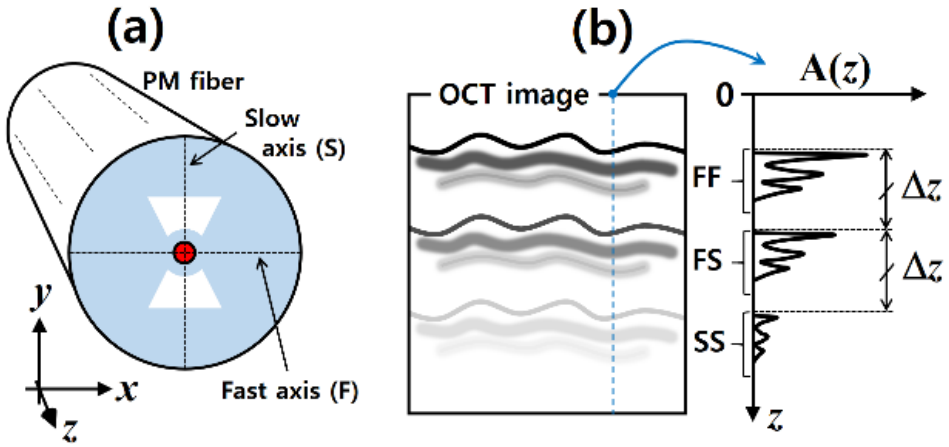

Figure 8.2 Definition of the coordinates with the PM fiber axes (a) and FF, FS, and SS image replicas obtained by our PS-OCT system (b).

The PM fiber utilized in our system is highly birefringent with two linearly polarized (LP) eigen-modes. As illustrated in **Figure 8.2(a)**, the light linearly polarized along the *x* axis (LP*x*) propagates faster than the light linearly polarized along the *y* axis (LP*y*) in the PM fiber. As a consequence, the OCT image obtained with the PM fiber in place produces repeated images. As depicted in **Figure 8.2(b)**, three replicated images can be generated by the roundtrip of the signal through the PM fiber. The fast-fast (FF) image is a result of the OCT signal delivered through LP*x* (fast) mode in the roundtrip. The slow-slow (SS) image is produced through LP*y* (slow) mode in the roundtrip. And the fast-slow (FS) image is obtained from the OCT signal which is delivered through LP*x* (fast) mode in one way and LP*y* (slow) mode in the other way. The axial separation between the FF, FS and SS images, denoted by Δz, equals one-way retardation of the PM fiber in the domain of axial delay, z. Here, Δz is determined by $\lambda \cdot L/B$ where B is the beat length and L is the fiber length of the PM fiber. In our system, Δz was measured to be 2.7 mm with L=12 m. In most cases, this amount of separation was sufficiently large enough to avoid spatial overlap of those three image segments.

The polarization composition of the signal returning from the sample can be analyzed if the polarization state input to the PM fiber is known. It is required to make the input state either LP*x* or LP*y*. In this letter, the case of LP*x* input will be mainly considered. Then, the amplitude ratio of two replicated images can be interpreted as that of the different polarization states for the returning light. This way provides a simple method of polarization-multiplexed detection with a single detection channel.

8.3.2 Calibration of polarization state

In our scheme, the polarization controls required for a known input polarization state are accomplished by our pre-operational setup procedure of the systematic polarization states. The

sample-arm polarization controller (sPC) and the reference-arm PC (rPC) in our system are aligned to produce certain image responses. In our polarization setup procedure, an optical reflector, such as a mirror, is placed at the sample stage since it exhibits no polarization dependence in its reflectance. Our alignment procedure involves the following steps:

Step 1 – Adjust the sPC for minimizing the amplitude of the SS image. Then, the input and the output of the PM fiber are completely in the LP*x* state. The FF image becomes the brightest.

Step 2 – Set the angle of the QWP to be 22.5° with respect to the *x* axis. Then, the reflected field recoupled to the PM fiber is equally distributed to the LP*x* state and the LP*y* state.

Step 3 – Adjust the rPC for equalizing the amplitudes of the FF image and the FS image. Then, the reference field interferes with the sample fields in both polarization states equally. Note that the roll-off characteristic of the signal amplitudes is neglected here.

Step 4 – Set the angle of the QWP to be 45° with respect to the *x* axis. Then, the sample-incident light is circularly polarized. From the reflector, the sample field recoupled to the PM fiber is completely in the LP*y* state. The FF image becomes the darkest while the FS image becomes the brightest. The system is ready to take PS-OCT images.

The angle of the QWP can be measured in reference to the geometry of the PM fiber. Or one can find the orientation of the *x* axis by which the QWP maximizes the amplitude of the FF image and minimizes that of the FS image after Step 1. Meanwhile, our polarization setup procedure discards the SS image by Step 1. The SS image has no chance to get non-zero intensity. One can take an alternative approach of discarding the FF image and setting the PM fiber output completely in the LP*y* state in Step 1. Then, the FF image must be replaced by the SS image in all the descriptions related to the polarization setup procedure.

8.3.3 Mathematical explanation

The effect of introducing a PM fiber section in our system can be described in simple algebra. The QWP acts as a transformer of polarization states. The LP*y* states at the PM fiber end are transformed to circularly polarized (CP) states before the sample. For a single sample reflection, the sample-reflected field generated from the sample-incident CP light is a vectorial field composed of two orthogonal bases of CP states, $\hat{e_1}$ and $\hat{e_2}$. Its interference with the reference field, which occurs at the coupler, can be equivalently taken at the exit of the QWP. The equivalent reference field, E_r, is expressed by

$$\overrightarrow{E_r}(z) = \hat{e_1} a_{r1} E(z) + \hat{e_2} a_{r2} E(z) \tag{8.1}$$

where a_{r1} and a_{r2} are the amplitude coefficients of the CP components. Here, $E(z)$ is the normal field that originates from the source light. Meanwhile, the sample field E_s is expressed in the same way by

$$\overrightarrow{E_s}(z) = \hat{e_1} a_{s1} E(z - z_0) + \hat{e_2} a_{r2} E(z - z_0 - \Delta z) \tag{8.2}$$

where a_{s1} and a_{s2} are complex amplitudes of the CP components. Δz is the one-way retardation of the PM fiber while z_0 is the common-mode delay of the sample fields to the reference which is the relative sample position. The detected signal intensity is taken from the sum of those two fields by summing up $|E_r+E_s|^2$ for the two vectorial components. In the complex notation, the interference term of cross-correlation intensity, I_{int}, is obtained by

$$\frac{I_{int}}{2} = Re\{a_{r1}^* a_{s1} E^*(z) E(z - z_0) + a_{r2}^* a_{s2} E^*(z) E(z - z_0 - \Delta z)\} \tag{8.3}$$

Here, the superscripted asterisk (*) denotes the complex conjugate and Re{} is the operation of taking the real part. The Fourier transform of I_{int} gives the spectral interferogram which is actually detected in SS-OCT. And its inverse-transform process gives the A-line profile of OCT imaging.

Eq.(8.3) suggests that it contains two replicated responses separated by Δz. For a large value of Δz, each can be spatially filtered for further processes without spatial overlaps.

The polarization evolution along the depth in a birefringent sample turns out to be a depth-dependent ratio of a_{s1} to a_{s2}. The first sample surface gives a_{s2}=0 by the polarization setup. The phase retardation of the sample field, δ, is found by

$$\delta = arctan(a_{s1}/a_{s2}) \tag{8.4}$$

for the signal roundtrip. As suggested by Eq. (8.3), the amplitude ratio of a_{s1} to a_{s2} can be found from I_{int} for a known ratio of a_{r1} to a_{r2}. By Step 3 of our polarization setup procedure, it is set up to be unity ($|a_{r1}|=|a_{r2}|$). Therefore, the retardation can be retrieved from the power ratio of the two terms of Eq. (8.3).

Based on the theory given above, the image signal processing for our PS-OCT can be performed with the acquired A-line data. The A-line reflectance profile, denoted by $A(z)$, is obtained by absolutizing the inverse Fourier transform of the spectral interferogram. The FF image and re-shifted FS image are taken by $A(z)$ and $A(z+\Delta z)$, respectively. Here, one must take the frequency dependence of Δz, *i.e.*, the differential dispersion into account. Numerical dispersion compensation can be applied to each image segment in a different mode. Hence, two A-line profiles of FF and FS images, A_{FF} and A_{FS}, are obtained, respectively, by

$$A_{FF}(z) = |F^{-1}\{J_{int}(k) \cdot D_{FF}(k)\}|, and \tag{8.5}$$

$$A_{FS}(z + \Delta z) = |F^{-1}\{J_{int}(k) \cdot D_{FS}(k)\}| \tag{8.6}$$

where $F\{\}$ and $F^{-1}\{\}$ denotes Fourier transform and inverse Fourier transform, respectively. Here, J_{int} is the spectral interferogram which comes from $F\{I_{int}\}$. D_{FF} and D_{FS} are dispersion-compensation functions for the FF and FS image segments, respectively [54, 179]. And k is the wavenumber. D_{FF} can be optimized for the best response of A_{FF} while D_{FS} can be for the best A_{FS}.

From the two A-line data given by Eq. (8.5) and Eq. (8.6), the PS-OCT image data can be retrieved. The normal A-line profile, A_{norm}, is obtained by the norm of the A-line reflectance vector as

$$A_{norm}(z) = \sqrt{A_{FF}^2(z) + A_{FS}^2(z)} \tag{8.7}$$

which makes up a polarization-independent OCT image. In the condition of $|a_{r1}|=|a_{r2}|$, one can assume $|A_{FF}|$ is proportional to $|a_{s1}|$ while $|A_{FS}|$ is proportional to $|a_{s2}|$. The sample-induced phase retardation is found with the normal profile by

$$\delta(z) = \ arcsin\left(\frac{A_{FS}(z)}{A_{norm}(z)}\right) = arccos\left(\frac{A_{FF}(z)}{A_{norm}(z)}\right) \tag{8.8}$$

from the FF and FS image data. Compared to the formula of Eq. (8.4), the calculation of Eq. (8.8) is more robust in avoiding divided-by-zero errors. By the property of the absolute amplitudes, the measured sample-induced retardation ranges from 0 to 90°. The spatial derivative of $\delta(z)$ will give the strength of the sample birefringence.

8.4 Results

8.4.1 Validation using ex vivo rabbit tendon and muscle

We tested the accuracy of retardation measurement for our PS-OCT system. A thin birefringent plate was used with one-way retardation of ~110°. We found an error of ~5° in the retardation measurements. Meanwhile, PS-OCT imaging capability of our system was tested with a tissue sample of rabbit tendon, *ex vivo*, with muscle attached to the side. **Figure 8.3 (a)** shows a raw OCT image. There, only the FF and FS image segments are shown for simplicity. The characteristic banding pattern was produced by the sample birefringence in each segment. This verified that the long PM fiber provided depth-encoded polarization channels in our PS-OCT system. To obtain reflectivity and retardation maps from the raw OCT image, two A-lines of $A_{FF}(z)$

and $A_{FS}(z+\Delta z)$ were prepared as given by Eq. (8.5) and Eq. (8.6). Each was compensated differently in dispersion by a numerical method. At each point of the image, A_{norm} and δ were calculated for reflectivity and retardation by using Eq. (8.7) and Eq. (8.8), respectively. Finally, **Figure 8.3(a)** and **Figure 8.3(b)** show the reflectivity map of the normal OCT image and the image of the sample-field retardation, respectively. The effect of the sample birefringence is clearly visualized in the pseudo-color map in **Figure 8.3(c)**. The tendon and muscle parts are easily distinguished by different levels of birefringence. Owing to the simplicity of our amplitude-based analysis, we have succeeded in real-time imaging of reflectivity and retardation [183].

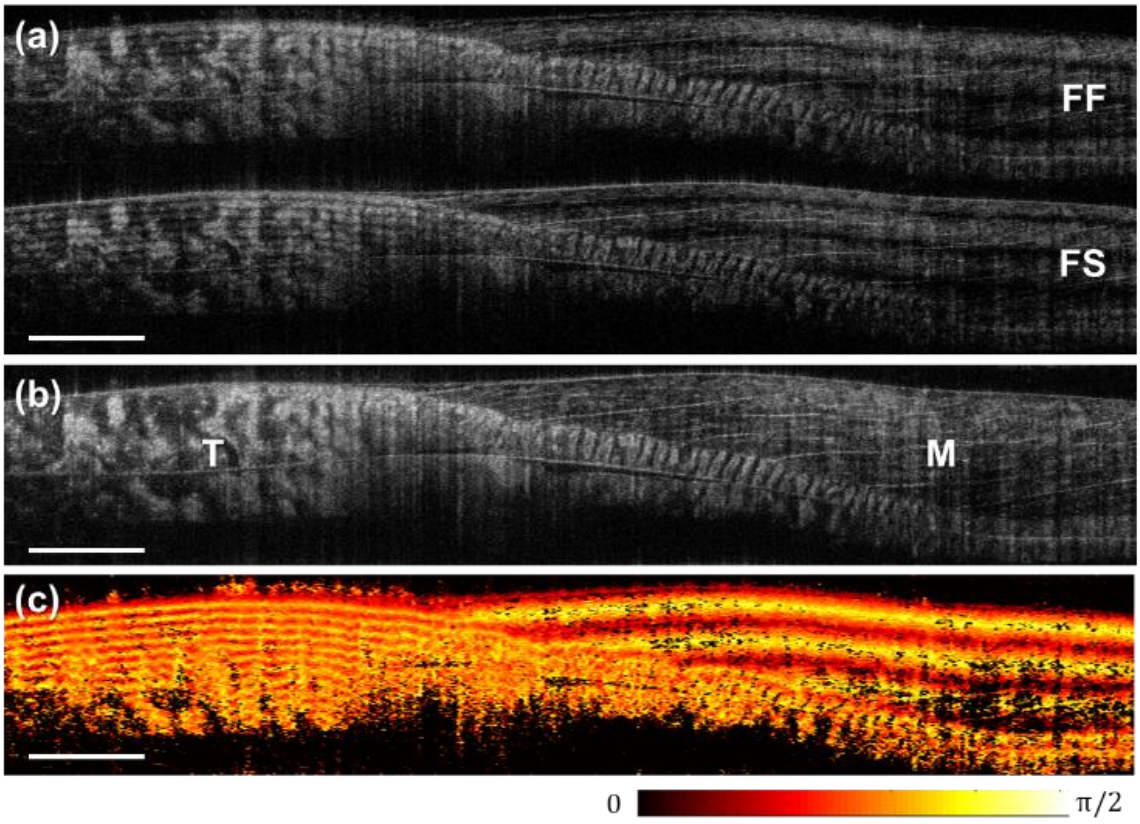

Figure 8.3 Images of rabbit tendon and muscle: The raw OCT image (a) contains FF and FS image segments separated by ~2.7 mm. The normal image of reflectivity (c) and the map of the sample-field retardation (d) were obtained by amplitude-based analysis given by Eq. (8.7) and Eq. (8.8), respectively. T: tendon, M: muscle. Scale bar: 2mm.

8.5 Discussion

In this study, we proposed and demonstrated a very simple configuration of PS-OCT. Any Fourier-domain OCT (FD-OCT) system can be reconfigured by simply adding a long section of PM fiber or any type of a polarization-differentiating delay unit as long as it has a sufficiently long axial imaging range for depth-encoded detections. Our method seems very attractive and particularly useful for spectral-domain OCT (SD-OCT) systems which have technical difficulties in implementing polarization-channeled spectrometers in pairs. The minimum required axial imaging range of OCT for 2-mm PS-OCT imaging is roughly 6 mm for three image segments not to collide. An SD-OCT system with good spectral resolution can provide enough margins for multiplexed detection.

The polarization controllers were manually aligned in our polarization setup procedure. We have observed that the systematic polarization states are maintained for at least a few hours if all the fibers are kept in a stable environment. Even though our procedure can be easily performed, the manual operation needs improvements for convenient and reliable operation. One may notice that the sPC can be re-aligned any time even in the middle of imaging after Step 1 of our polarization setup procedure. As well, it can be automated with an electrically controlled PC which is managed at the lowest amplitudes of the SS image in a closed-loop operation mode. On the other hand, alignment of the rPC requires a special condition made by Step 2 and can hardly be performed in the middle of an imaging operation. This brings the need for further improvement and study to produce fully automated operations.

Unlike most SM fiber-based systems, our PS-OCT system keeps a fixed CP state at the sample incidence. Likewise, the axes of the polarization detections are also fixed by the PM fiber. This allows us to measure the absolute state of polarization for the sample field. We could take

advantage of the amplitude-based analysis which is simpler and more robust. To retrieve full polarization information including the orientation of birefringence, the signal phases of the two polarization channels must be obtained as well. Even with very long fiber delays, previous studies suggest that proper signal processing can extract the phase-involved information for PS-OCT [191]. However, it can be achieved with added complexity in signal processing and system calibration. It is worth noting that the phase errors can be produced by different numerical dispersion compensations or image shifting in our scheme, especially involving errors in *k*-domain signal sampling that relate to inaccurate timing synchronization in an SS-OCT system [179] or erroneous spectral calibration in an SD-OCT system [197].

8.6 Summary

In summary, we proposed a very simple PS-OCT construction scheme with a long PM fiber utilized for depth-encoded polarization-multiplexed signal detection. An ordinary SS-OCT system was easily upgraded by adding delay fibers and keeping a single balanced photodetector. A polarization setup procedure was developed to operate our system at desired polarization states. Phase retardation information was successfully obtained from a tissue sample. We believe that our method can be a practical alternative for applications which demand an economic way of constructing a PS-OCT system.

Chapter 9 – TRANSVAGINAL OPTICAL COHERENCE TOMOGRAPHY

9.1 Overview

Genitourinary syndrome of menopause (GSM) is a condition that arises from a physiological decline in estrogen levels and negatively affects more than half of postmenopausal women. Energy-based thermal deposition has been explored as a minimally invasive treatment for GSM. However, its mechanism of action and efficacy is controversial, in part, due to the lack of noninvasive imaging tool for vaginal tissue. Here, we report a clinical translation of transvaginal OCT to quantitatively monitor the changes in the vaginal epithelial thickness (VET) during fractional-pixel CO_2 laser treatment. We performed a clinical study on two post-menopausal patients (natural and surgical menopause) experiencing GSM symptoms. The effect of laser treatment was evaluated in terms of changes in the VET along the vaginal canal, as shown in the transvaginal OCT. A machine learning segmentation based on U-NET was applied to the OCT images to assess the thickness distribution of VET. We observed atrophy in VET and reduction of vaginal folding in the natural menopause patient. Following the laser treatment, we observed the >100 μm increase in the VET in the mid and distal portion of the vaginal wall in the patient with natural menopause. Unexpectedly, the patient with surgical menopause showed little changes in VET as well as the improvement in the GSM symptoms. These results demonstrate the potential utility of transvaginal OCT endoscope in evaluating the vaginal tissue integrity and tailor vaginal laser treatment on a per-person basis, with the potential to monitor other treatment procedures.

9.2 Introduction

Genitourinary Syndrome of Menopause (GSM) is a broad term that describes symptoms that arise from a physiologic decline in estrogen levels [198–200]. GSM affects up to 50% of women and negatively affects their quality of life with regard to general health and sexual function [199]. It is known that estrogen deficiency leads to reduced vascularization, lubrication, tissue elasticity, and thinning of the vulva, vagina, and urethra (**Fig. 9.1**). As a results, post-menopausal women suffer from a variety of symptoms—including vulvovaginal atrophy, dryness, burning, itching, urinary disorders, and more—that negatively impacts a woman's quality of life [201–203]. Although therapies for alleviating GSM symptoms exist, developments of new and safer GSM treatments have been in latency, in parts due to the lack of objective means for quantifying treatment outcomes.

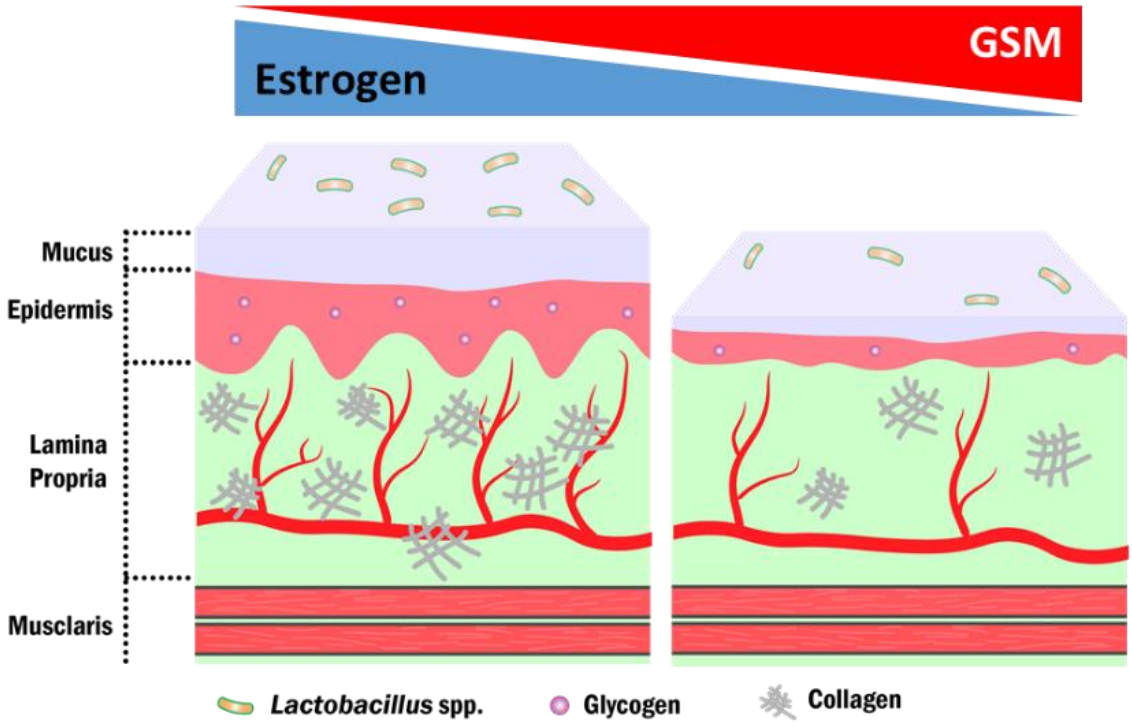

Figure 9.1 Structural and functional changes in GSM patients.

Due to the safety concerns and even the efficacy of long-term use of topical or systemic hormone therapy as the conventional treatment, an increasing number of women are now seeking more modern approaches. One contemporary method that is not yet FDA approved for treating GSM is the use of energy-based devices, such as a fractional laser. This tool stimulates vaginal tissue regeneration to improves the physiological condition of the tissue [204–206]. Nevertheless, standardized protocols do not exist for the use of such devices and studies on treatment efficacy are inconclusive, warranting further investigation [198]. Limited pathology evidence from human studies has demonstrated an increase in vaginal epithelial thickness (VET), vascularization in lamina propria, neocollagen, and elastin formation in the genitourinary tract due to the thermally induced healing process [204–206]. Although it can provide quantitative information, conventional histological data requires biopsy, which is rarely performed on vaginal tissue because of its invasive nature. Therefore, the capability to demonstrate clinically significant histology comparing treatment-related vaginal tissue changes is of high scientific and clinical value as it can provide histopathological information before and over the time course of therapy to monitor and optimize the treatment.

OCT is an interferometric technique that was initially developed to perform “optical biopsy” on the posterior eye and coronary artery and, for its minimal invasiveness, has been seen well-adapted as a biomedical imaging modality across many specialties in the past two decades [207]. Using non-ionizing near-infrared light, OCT can visualize depth-resolved information in three-dimension *in vivo* with a spatial resolution 2-3 order of magnitude higher than that of ultrasound imaging. Transvaginal ultrasound exists for evaluating gross anatomical structures but lacks the necessary resolution to quantitatively assess human VET and study the underlying tissue microstructures [208].

Utilizing the high resolution enabled by OCT, Vincent *et al.* have previously validated VET measurements after treated with nonoxynol-9, a spermicide that causes epithelial disruption and thinning, in sheep; they demonstrated the capability of OCT to visualize the epithelial-lamina propria interface and epithelial changes after the nonoxynol-9 treatment [209, 210]. Nevertheless, the catheter-based OCT imaging system employed by Vincent *et al.* was limiting in imaging speed and scan area, which make it impossible to visualize the entire volume of vaginal canal. Our group has recently developed an OCT imaging catheter with wide-field scanning for transvaginal tissue imaging in the human vaginal canal *in vivo* [211]. The small form factor of the imaging catheter (outer diameter = 1.2 mm), while providing the benefit of minimal discomfort, cannot allow for comprehensive assessment of the human vaginal structure due to its highly folding nature.

In this study, we describe an OCT-based approach to objectively and accurately quantify VET throughout the entire vaginal canal *in vivo*. We developed a handheld transvaginal OCT probe to capture the full volume of human vagina in high resolution, and this enabled us to study the effect of vaginal laser therapy based on VET measurements obtained before and after the laser treatment. To complement the large number of images obtained through volumetric imaging, we applied a deep learning technique to autonomously segment the vaginal epithelium for high-throughput VET measurement and vaginal reconstruction in 3D. The findings demonstrate the efficacy of the proposed transvaginal OCT as a quantitative method for monitoring vaginal epithelium health, providing a platform for future pharmacological and medical device developments aiming to improve the quality of life among postmenopausal women.

9.3 Methods

9.3.1 Study Design

All investigations were carried out in accordance with the University of California Irvine Institutional Review Board under protocol HS# 2017–3686. For this study, two postmenopausal women (one 70-year-old patient with natural menopause, one 45-year-old patient with bilateral oophorectomy) were recruited from the Division of Female Pelvic Medicine and Reconstructive Surgery at the University of California, Irvine. Both subjects were experiencing GSM symptoms and received pixelated fractional CO_2 laser micro-ablation treatment with FemiLift (Alma Lasers Inc., IL). Baseline OCT images were acquired before the laser treatment and post-treatment OCT images were acquired 4-6 weeks after one laser ablation.

During the OCT measurement, patients were positioned in dorsal lithotomy. Prior to the image acquisition, a small amount of water-based vaginal lubricants was applied to the probe outer surface. The transvaginal probe was inserted into the patient's vagina and navigated to the cervix to obtain a full vaginal length scan. Once the OCT catheter was in position, the centerpiece of the transvaginal probe was withdrawn to obtain a 360-degree image of the entire vaginal canal.

9.3.2 Transvaginal optical coherence endoscopy

The OCT imaging system is based on a 1.3 μm swept-source laser, which is similar to what we have described in our previously study using a different laser source [211]. For in vivo imaging of the full vaginal canal, we designed a handheld transvaginal endoscope based on the previous catheter-based endoscope. Since the vaginal canal is highly elastic and creates folding structures if the size of the endoscope is too small, we designed a clear oblong-shape outer protective cover with an outer diameter of 12 mm and a length of 150 mm (**Figure 9.2**). To acquire a concentric

scanning of the endoscope, we designed a centerpiece consists of a rotational bearing and a 3D printed support. The centerpiece can also slide across the oblong-shape cover so that full vaginal canal scanning can be obtained. In this study, the endoscope was rotated at 3,000 rpm driven by an external rotary junction (MJP-SAP-131, Princetel Inc., NJ). Volumetric OCT scanning of the entire vagina was obtained by withdrawing the probe at approximately 2 mm/s. The full scan of vaginal scan was completed within 40 seconds.

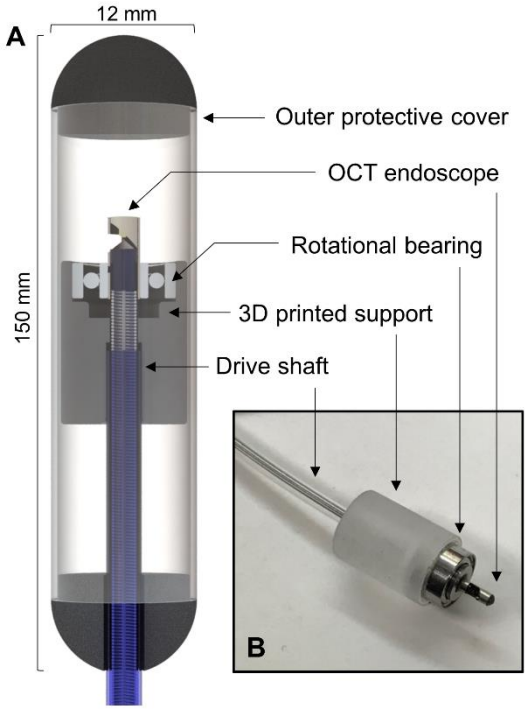

Figure 9.2 Handheld transvaginal OCT endoscope schematic. (**A**) 3D rendering of the transvaginal endoscope. (**B**) Centerpiece of the endoscope which provide helical scanning of the tissue. The rotation of the catheter-type endoscope is supported by a rotational bearing.

9.3.3 Automated epithelium thickness measurement

We extracted the VET from the OCT images using machine learning segmentation. In the vaginal OCT images, VET represents the dark layer between strongly reflecting the mucus layer and lamina propria. In this study, we applied a convolutional neural network (CNN) based on U-Net to locate and extract the VET. First, all the OCT images were converted to the polar coordinate

system and re-sized to 256 x 256-pixel images using interpolation. To train the U-NET model, 48 OCT images were selected from four 3D OCT data sets and the VET was manually labeled by an experienced OCT reader. Among all the labeled images, 12 images were used to evaluate the accuracy of the model and 36 images were used to train the model. Dice similarity coefficient below is used to evaluate the training accuracy. Dice coefficient can be calculated as $2|X \cap Y|/(|X| \cup |Y|)$, where X is prediction and Y is ground truth (manual label).

9.3.4 Statistical Analysis

Statistical analyses were performed using R (version 3.5.1). Arithmetic mean were compared using Wilcovon-Mann-Whitney test after the differences in the variances were tested. P values of less than 0.05 were considered statistically significant.

9.4 Results

9.4.1 Transvaginal OCT of human subjects

Folds naturally exist in human vagina and can create artifacts during OCT imaging. As the vaginal canal is highly elastic, imaging artifacts caused by vaginal folds can be reduced by proper sizing of the imaging probe. Here, we designed an imaging probe that can freely rotate and translate, concentrically, within an oblong-shaped protective cover, which has a 12-mm outer diameter and a 150-mm length. Driven by an external DC motor, the imaging probe was rotated at 50 revolutions per second, acquiring OCT images at a rate of 50 frames per second. Volumetric OCT of the entire vaginal canal was achieved by manually withdrawing the probe at approximately 5 mm/s.

Two postmenopausal women were recruited for the study: a 70-year-old with natural menopause and a 45-year-old with bilateral oophorectomy wearing an estrogen ring. Both subjects reported

experiencing GSM symptoms and received one-time pixelated fractional CO_2 laser treatment (FemiLift, Alma Lasers Inc., IL). Transvaginal OCT was performed to image the entire vaginal canal before and 4-6 weeks after the laser treatment. Both participants were imaged in a standard gynecologic examination room. The patients were positioned in dorsal lithotomy during OCT imaging. A small amount of water-based vaginal lubricant was applied to the surface of the protective cover of the imaging probe before the clinician maneuvered the transvaginal probe into the vagina. The distal tip of the imaging probe was navigated to the cervix for obtaining the full volume of the vaginal canal. Once positioned, an operator initiated the probe rotation and translation within the protective cover to acquire the data. Scanning of the entire vaginal canal was completed within ~40 seconds. The patients reported only minimal discomfort from the insertion of the protective cover and the motion caused by the rotating probe.

9.4.2 Vaginal OCT images

A total of 4 datasets were collected from the two patients. OCT images demonstrate a penetration depth of approximately 1.5 mm into the vaginal wall and can resolve the mucus, epithelium, lamina propria, and venous plexuses (**Fig. 9.3**). The epithelium layer had lower pixel intensity due to its less scattering optical property with respect to the mucus and lamina propria. The boarders between the mucus and the epithelium, as well as between the epithelium and the lamina propria were well-demarcated and easily differentiated visually by clinicians. As opposed to our previous study, the protective cover that slightly extends the vaginal wall allows for imaging of more surface area, and thus revealed the heterogeneity of vaginal epithelium including rete ridges. Generally, the distal region of the vagina had thicker epithelium and more vaginal folds.

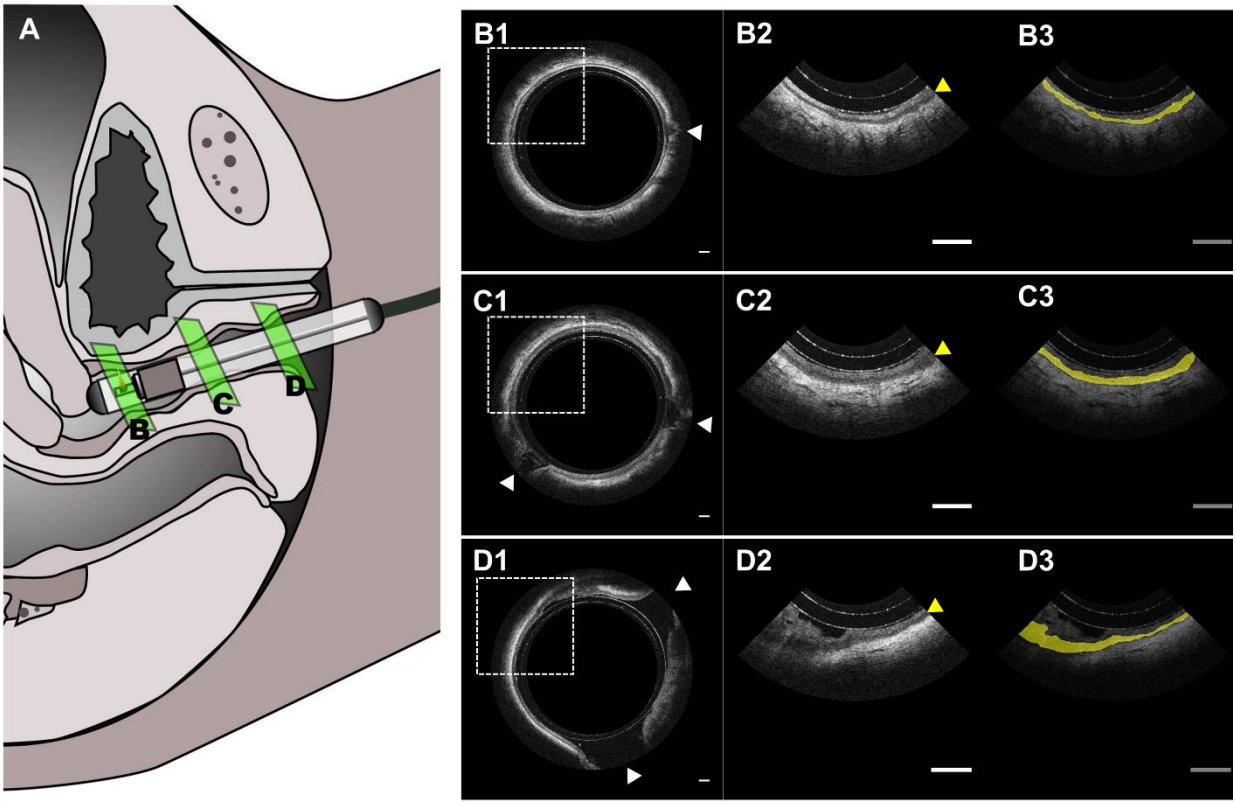

Figure 9.3 In vivo OCT imaging of a 70-year-old menopausal patient. (A) Schematic of in vivo human imaging and the placement of endoscope. (B) Transvaginal OCT endoscopy image of the proximal vagina near cervix with an expanded view (B2-D2) and the highlight of VEL (B3-D3). (C) OCT image acquire at proximal vagina. (D) OCT image acquired at distal vagina near the opening. The white arrows indicate vaginal folding and the yellow arrows indicate VEL.

9.4.3 Autonomous segmentation of VET

A deep learning algorithm based on U-Net architecture was developed and trained to autonomously perform tissue segmentation to identify VET [86]. The resulting Dice coefficient was 0.775. Volumetric renderings of VET based off the segmented data were generated, and the 3D vaginal canal reconstruction of the natural menopause patient is presented in **Figure 9.4**. The reconstructions of VET from the four datasets demonstrated location dependency of the features and structures within the vaginal canal. As shown in **Figure 9.4**, the vaginal wall appeared to be a more level topography with thinner overall VET in the proximal region. The mid-section of the canal showed the transition from the proximal region to the distal region, where abundant vaginal

folds exist and VET was visibly thicker. In the distal opening, parts of the labia minora can be identified.

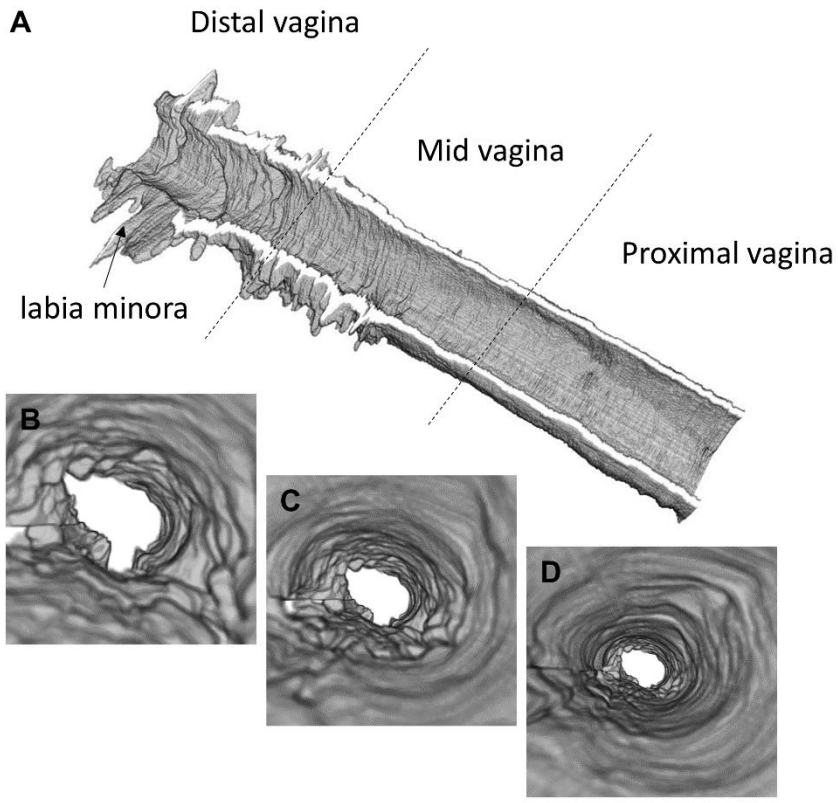

Figure 9.4 Three-dimensional reconstruction of vaginal epithelium. (A) 3D rendering of the entire vaginal canal showing the VEL thickness and surface topology of a menopausal patient. (B-D) flythrough views of VEL feature at distal (B), mid (C), and proximal (D) vagina.

9.4.3 OCT for assessing laser treatment efficacy

We visualized the VET distribution before and 30 days after the laser treatment for the two menopause patients (**Figure 9.5 A&B**). The mean VET of the natural menopause patient showed significant increase, from 130±26 μm to 181±54 μm after the laser treatment ($p < 0.05$), which was more than one standard deviation of the baseline VET. However, the mean VET of the surgical menopause patient does not change significantly (from 296±36 μm to 293±36 μm, $p=0.246$). Second, we plotted the VET along the vaginal canal (**Figure 9.5C&D**). For the natural menopause

patient, we found the mid- to distal-vagina had the most significant changes in the VET. For the surgical menopause patient, there were little noticeable changes in the mean VET.

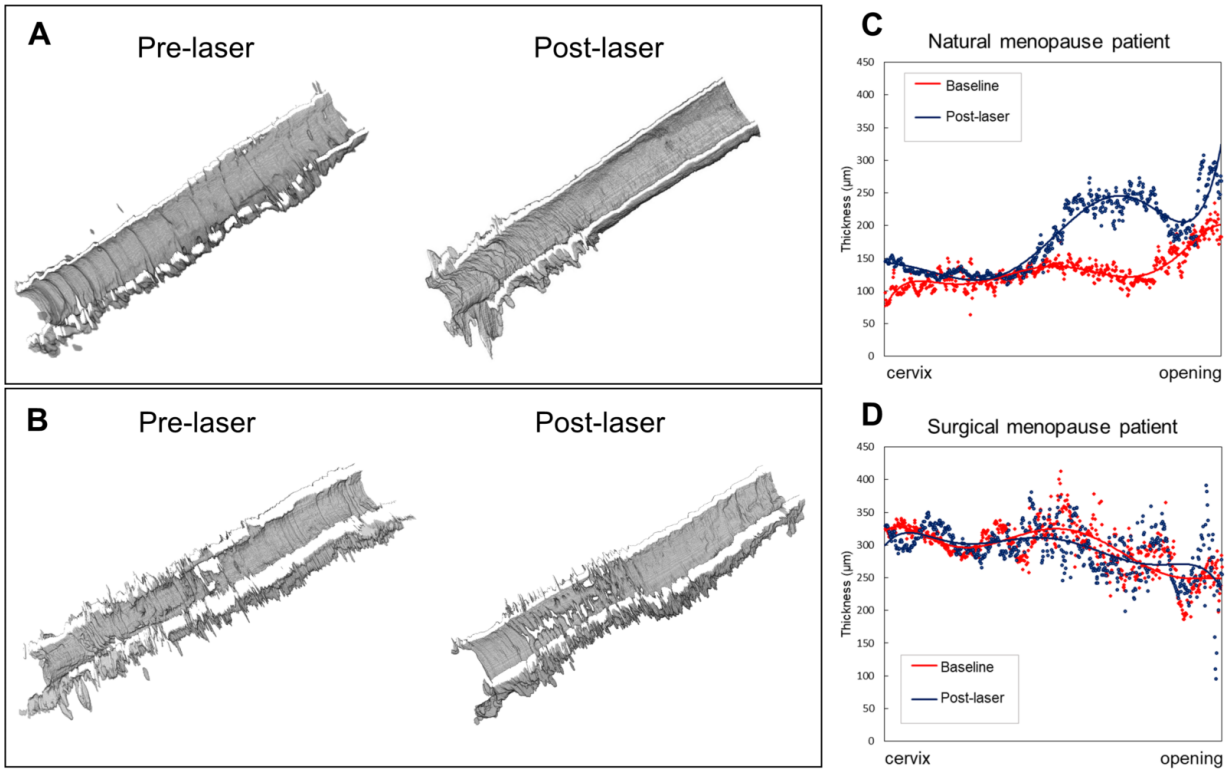

Figure 9.5 Morphological comparison of menopausal patients before and after laser. (A) Reconstruction of 70-year-old patient's VET with natural menopause. (B) Reconstruction of 40-year-old patient's VET with surgical menopause. (C and D) VET measured at different anatomical locations along the vaginal canal. The vertical axis indicates the thickness in um and the horizontal axis indicates the anatomical location.

9.5 Discussion

In this study, we investigated the use of transvaginal OCT and the accompanying computer vision technique as a minimally invasive method to evaluate tissue-level response to the CO_2 laser ablation therapy in human subjects. The OCT probe design enables 3D capturing of the entire vaginal canal, allowing for visualizing the longitudinal changes of vaginal microanatomy that provide insights into vaginal health. Since volumetric scanning yields hundreds of images per scan, we developed a deep learning algorithm based on the U-NET architecture and demonstrated its

utility for high-throughput analysis. As such, VET measurements can be speedily obtained during the patient's visit, and such quantitative patient-specific information may personalize the treatments for GSM symptoms as it can identify the regions within the vagina that require further or less intervention.

The capability of visualizing depth-resolve tissue microanatomy in the vagina, in vivo, allows for direct measures of morphological and pathophysiologic response to therapy. In the case of assessing laser therapy as presented in this study, our approach helps identify the regions that the laser ablation may be effective. This provides valuable feedbacks for optimizing energy-based devices for relieving GSM symptoms by fine-tuning parameters such as duration, dosage, and frequency based on locations. With the ability to quantify vaginal tissue health, the utility of transvaginal OCT can be further extended to evaluating the efficacies of other types of interventions, such as topical estrogen, systemic hormone replacement therapy, or non-medicated topical moisturizers. At present, clinicians primarily collect feedback through patient-reported outcome measures. Gauging the response to therapy with quantifiable OCT measurements will provide an objective approach to screen patients that can benefit from the laser treatment, evaluate the treatment performance, and aid the development of new devices and pharmaceuticals.

Two postmenopausal patients undergoing CO_2 laser treatment were evaluated using OCT in this study, and both reported little to no discomfort during the imaging. In our previous study, we showed that VET differs among premenopausal, perimenopausal, and postmenopausal women, with the postmenopausal category having the thinnest VET. In this study we demonstrated the association between VET and estrogen such that the younger post-menopausal woman wearing an estrogen ring had a thicker VET than the estrogen deficient older woman. This confirms that VET decreases with age and/or reduced estrogen level. The average VET of the 70-year-old patient

increased 1 month after the laser therapy, supporting the previous clinical findings that laser ablation promoting epithelium proliferation in the vagina [212, 213]. Conversely, the 45-year-old surgical menopause patient had minimal change in VET, suggesting that estrogen status, age and perhaps the mechanism of menopause (i.e., natural vs. surgical) impact response to laser microablation.

Of further interest was the variation in VET along the vaginal length in the 70-year-old patient. Specifically, the proximal vagina was noted to have a thicker VET with a clear transition point compared to the mid and distal vagina. After laser ablation, the mid and distal vagina demonstrated a greater change in VET. These findings suggest that OCT imaging may be able to resolve microstructure variations that support the dual-embryologic origin of the vagina. Specifically, the leading theory on uterovaginal development suggests that the proximal 1/3 of the vagina arises from the paramesonephric ducts while the distal 2/3 of the vagina derives from the urogenital sinus [214, 215]. Thus, the differentiation visualized on OCT supports this concept.

The present observation demonstrated the VET can be recovered to some extent as a result of therapy. In addition, several features of vaginal tissue that we observed using transvaginal OCT in human has not been seen previously. Spatial distribution of VET provides insights into laser micro-ablation treatment strategies, as it suggests the changes in the tissue is highly heterogeneous. Further investigation of light-based imaging of the capillaries net in the lamina propria, and elasticity of the vaginal wall may offer a new concept of scientific data about age-related changes, lubrication, and control of urination.

Chapter 10 – Summary and Conclusion

10.1 Summary of Work

This thesis explores digital quantification and functional imaging techniques for improving the clinical utility of endoscopic OCT in airway imaging. OCT provides reflectance imaging of tissue cross-sections with micrometer resolution in near real-time using a nondestructive method. In addition, OCT can be readily incorporated into clinical endoscopy as the scanning portion can be made into a flexible fiber optic probe. However, there are number of limitations in OCT for accurately assessing early changes in tissue microarchitecture and function in airway inhalation injuries. The motivation of this thesis is to enhance diagnostic capability of endoscopic OCT in detecting subtle tissue alterations through automated quantitative analysis and functional OCT imaging techniques.

The investigations for this thesis included *ex vivo* tissue imaging, post-mortem animal models, *in vivo* animal models, and *in vivo* human studies. Extensive studies were conducted using toxic-inhaled animal models including methyl-isocyanate and smoke inhalation injuries. Compared to traditional OCT image analysis, automated tissue segmentation techniques provide a means to detect airway tissue damage with much higher accuracy and sensitivity in a shorter processing time. In addition to automated analysis, new functional OCT imaging techniques that do not only rely on tissue backscattering were explored in the second half of this thesis to obtain additional tissue contrast for monitoring the progression of airway injury. Finally, these studies inspired new ideas for application of endoscopic OCT in gynecology, including image-guided vaginal laser ablation therapy.

Previous airway studies have demonstrated the ability of endoscopic OCT to visualize airway shape and tissue substructure, but analysis of the images mostly relied on human interpretation. In some studies, correlation with histology were established [216]. However, early tissue changes in airway inhalation injuries are typically subtle and difficult to identify. Typically, manual segmentation of large volume data is needed to get more accurate information of early physiological changes [138] which is time-consuming and labor intensive and can reduce its usefulness as a real-time guidance tool in a clinical setting. To address this limitation, we developed and applied an automated tissue segmentation algorithm based on dynamic programming method.

First, we introduced a method to quantitatively assess MIC-induced airway injuries in a rat model. Current methods for understanding toxin-exposed airway injuries are limited by cost, labor time, or accuracy and only provide indirect or localized information of an obstructed airway structure. Therefore, there exists a need to develop a new imaging and quantitative analysis tool. One limitation for gathering information in a rodent model after toxic gas exposure using an endoscope is the probe size necessary for accessing the small, narrow, and partially obstructed trachea. Hence, we designed a 0.4-mm-diameter miniature endoscopic OCT probe for investigating the structural changes in rat trachea after MIC inhalation. We adopted a lens-free fiberoptic design and stepwise transitional core structure for a high-resolution ultra-thin endoscopic probe. An automated 3D visualization and segmentation algorithm based on dynamic programming was implemented so that anatomical changes, such as lumen volume and cross-section areas, could be quantified. We demonstrated narrowing near the upper trachea as a result of epithelial detachment and extravascular coagulation in the trachea of a post-mortem rat after exposure to MIC.

Endoscopic OCT combined with automated segmentation can also be applied to smoke inhalation injury. Using a porcine model, we assessed *in vivo* proximal airway volume after smoke inhalation injury using automated OCT segmentation and correlated the OCT volume measurement to lung function for rapid indication of acute respiratory distress syndrome (ARDS). ARDS is a severe form of acute lung injury with a mortality rate of up to 40%, which requires early management through sensitive imaging tools and robust analysis software. We found significant decrease in the OCT airway volume after smoke inhalation. The study also demonstrated that the decrease in the airway volume was more prominent in the animals that developed ARDS after injury. In addition, proximal airway volume was correlated with respiratory parameters, including peak inspiratory pressure ($r=0.48$, $p<0.001$), compliance ($r=0.55$, $p<0.001$), resistance ($r=0.35$, $p<0.01$), MT ($r=0.60$, $p<0.001$), and PiO2-to-FiO2 ratio ($r=0.34$, $p<0.01$). This demonstrates the capability of OCT to quantify both tissue changes and respiratory function changes after inhalation injuries which can be used to predict the clinical outcome at an early stage.

Along with the automated analysis technique, three functional OCT-based imaging techniques were also developed for airway application. First, we presented a method to obtain an accurate airway compliance measurement by correcting non-uniform distortion (NURD) in a micromotor imaging catheter. The method corrects the distortion in the image by first identifying the wire artifact and then segmenting the nonlinear surface profile of the plastic sheath through dynamic programming. Since the probe is positioned nonconcentric relative to the sheath, the surface profile of the sheath appears nonlinear in the polar coordinate image, which can be used to effectively correct the local distortion in the image. Since the proposed method does not require correlating the tissue signal, real-time correction of the NURD can be performed without relying on the tissue contrast. To demonstrate feasibility, we acquired dynamic OCT images of human

nasopharynx during the respiratory cycle. Regional compliance measurements showed a larger compliance value in the adenoid tissue as compared to the soft palate in the same cross-sectional plane.

A new imaging technique called spectrally encoded interferometric microscopy (SEIM) was developed and demonstrated for visualization of cilia motion in the airway. The SEIM technique is capable of detecting nanometer displacement at kilohertz frame rates by employing a rapidly wavelength-sweeping laser and a spectral disperser. In this study, we compared different SEIM processing algorithms based on Doppler shift and decorrelation for visualizing dynamic cilia movement. We found that the phase-resolved Doppler method after phase stabilization and bulk motion correction provides the highest sensitivity for cilia beating measurement compared to phase-resolved Doppler variance (PRDV) and intensity-based Doppler variance (IBDV) methods. The feasibility of the method was tested on a freshly excised rabbit trachea immersed in cell culture medium under a temperature-controlled environment. In addition to the cilia beating cycle, traveling waves caused by the coordinated cilia motion in an excised tissue were visualized for the first time. The results collectively demonstrated the potential clinical utility of this technique to monitor respiratory function and therapeutic responses.

Next, we presented a very simple and robust method of constructing a PS-OCT system that can be applied to airway imaging. PS-OCT is capable of visualizing and quantifying the material birefringence, which is the property of a material to alter the polarization state of the light. In the airway, smooth muscle and collagen-rich tissues are known to have high birefringence. Typically, PS-OCT requires complex setups with additional detectors and careful calibration of the polarization state of the incident beam, which requires significant modification of the OCT system and high building costs. In our case, an ordinary fiber-based swept-source OCT system was

reconfigured for PS-OCT by adding a long section of polarization-maintaining fiber in the sample arm. Two polarization modes with a large group-delay difference formed spatially distinguished polarization channels. The depth-encoded information on the polarization states could be retrieved by amplitude-based analysis. We found our method provides an economic scheme for PS-OCT

Finally, a new application of endoscopic OCT was explored in gynecology in this thesis. Despite the emerging market of energy-based devices to treat Genitourinary Syndrome of Menopause (GSM) in menopausal women, the exact effect of the laser on vaginal tissue remains poorly understood. We developed a point-of-care endoscopic imaging system based on OCT to obtain information on three-dimensional structural changes in vaginal epithelium during laser treatment. We evaluated two post-menopausal patients (natural and surgical menopause) experiencing GSM symptoms. While we observed more than a 100 μm increase in vaginal epithelium thickness in the natural menopause patient following laser treatment, the patient with surgical menopause showed no significant changes in vaginal epithelium thickness as well as GSM symptoms. These results demonstrated that the transvaginal OCT endoscope may provide clinicians and scientists with an important tool for screening the patients that will benefit from the laser, monitor the progression of laser therapy, and evaluate the tissue response from the laser treatment and further individualize treatment strategies.

10.2 Future Studies

This section briefly describes some possible future research directions for this research area. The main topics are summarized and discussed in detail below.

10.2.1 Integration of optical coherence tomography angiography (OCTA) to the transvaginal endoscope

In chapter 9, we described the development and evaluation of a novel transvaginal OCT endoscope for assessing vaginal health and monitoring the treatment progression. The image-based vaginal health index was based on the epithelium thickness as it correlates with the estrogen level. In post-menopausal women, it is known that estrogen deficiency also leads to reduced vascularization and decreased blood flow within the vaginal lamina propria [217]. Therefore, the clinical value of being able to non-invasively visualize and measure microvascular networks over time in diseased genitourinary tissue holds tremendous potential. In the future, an OCT angiography technique can be incorporated to the transvaginal imaging probe. OCTA and Doppler OCT are functional extensions of OCT, which allows for visualization of vascular networks and flow velocity within microvessels at different tissue depths [58, 59, 218, 219]. To successfully integrate OCTA technology into the vaginal endoscope, several aspects need to be taken into account. First, we will increase the lateral resolution of the intravaginal endoscope by using an optical relay system instead of fiber optics as illustrated in **Figure 10.1**. The new OCTA imaging probe will consist of a collimator, a high-speed 2-axis scanner, a series of relay lenses, and a 45° reflective mirror. High lateral resolution is required to resolve microvasculature with a small vessel diameter. Since the lateral resolution is proportional to the numerical aperture, we will use a half-inch lens in order to increase the entrance pupil diameter. In addition to the lateral resolution, speed and stability of scanning are other important considerations for creating a clean OCTA image since

they rely on the speckle fluctuation or phase shift from blood vessels. In addition, OCTA and Doppler OCT typically scan the same area repeatedly to improve the imaging contrast so the scanning speed needs to be fast enough to avoid bulk motion as well as prolonged image acquisition. To achieve high-speed and high-stability scanning, a high-speed 2-axis galvanometer scanner can be incorporated. With 400 kHz sweeping-rate laser, fast-axis scanner will have a 1-kHz scanning rate for acquiring a volume of 400x400 A-lines in less than 0.4 seconds. The OCT light enters the handheld probe with a beam diameter of 4 mm through a collimator, and the collimated beam scans using a 2-axis scanner. To effectively utilize the 2-axis scanning, we will employ the bidirectional scanning scheme rather than the conventional unidirectional scanning pattern to improve the acquisition speed [220]. Similar to the cilia imaging discussed in Chapter 7, OCTA and Doppler contrast can be constructed through different processing methods, including phase-resolved Doppler, phase-resolved Doppler variance, and intensity Doppler variance. The clinical value of being able to non-invasively visualize and measure microvascular networks over time in diseased genitourinary tissue holds tremendous potential.

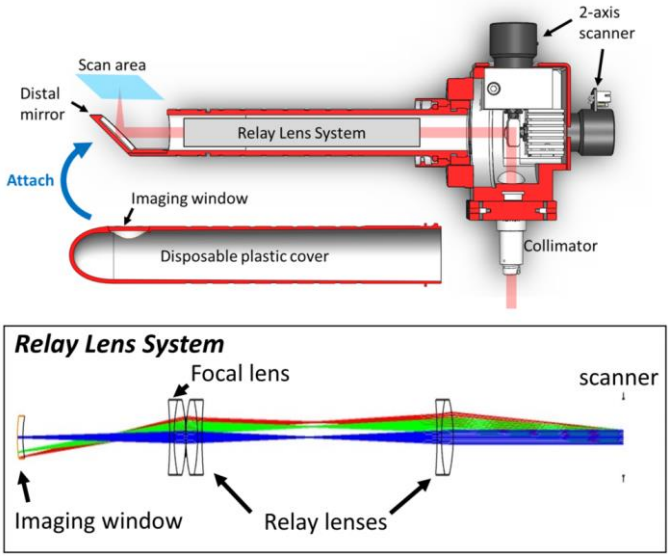

Figure 10.1 Schematic of OCT/OCTA endoscope and optical relay system.

10.2.2 Integration of optical coherence elastography (OCE) capability to the transvaginal endoscope

While OCT/OCTA can provide information on structural integrity and blood supply, OCE can evaluate tissue elasticity of collagenous tissue. OCE uses optical imaging to resolve tissue stiffness with high spatial resolution. In pelvic medicine, OCE will be a viable tool for obtaining the elasticity of genitourinary epithelium and lamina propria before and after laser treatment. To integrate OCE into the transvaginal endoscope, we propose two methods for elasticity quantification: transverse shear wave [221, 222] and compression-based [117, 222, 223] (**Figure 10.2**).

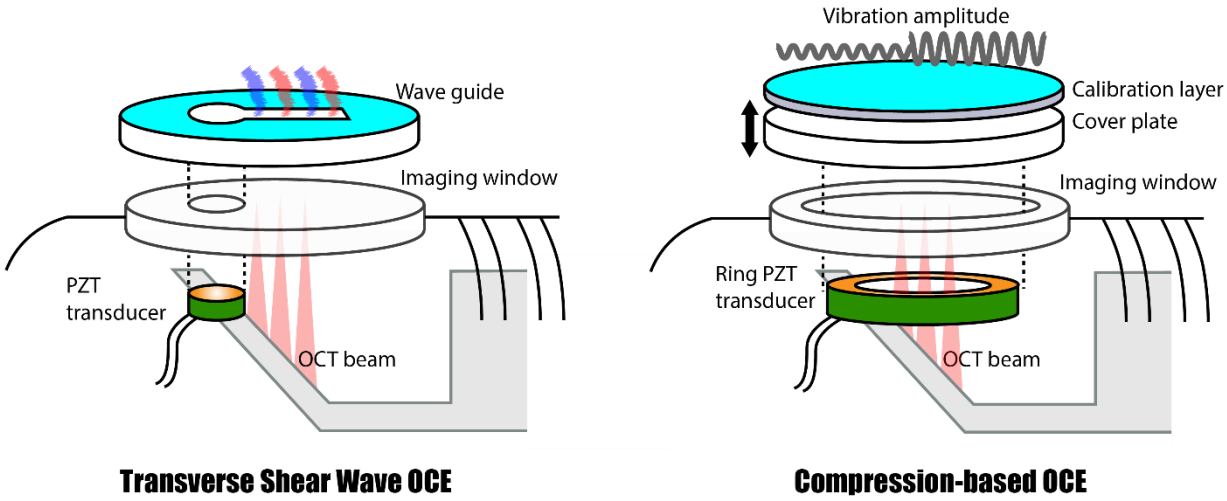

Figure 10.2 Schematic of PZT excitation and OCT detection. In the transverse shear wave OCE method, a small PZT actuator pushes the tissue. In the compression based OCE method, a ring PZT actuator is attached to a cover plate to induce tissue vibration.

Shear wave method: The shear wave-based approach is one of the most commonly used OCE methods since the shear wave propagation speed in tissue directly correlates to the Young's modulus, and imaging the tissue displacement induced by a shear wave can recover the quantitative elasticity. We previously demonstrated a shear wave method based on confocal excitation to quantify the mechanical properties of retinal layers *in vivo* [222, 223]. To generate a transverse

shear wave, an excitation source will be configured next to the scanning area. We will use a small piezo transducer (PZT) to generate a synchronized movement at a 10-μm travel distance. The distal face of the piezo transducer will be fixed to the imaging window so that its movement perturbs the tissue to generate shear waves. To remove the boundary effect from the imaging window that can restrict and dump the shear wave, we will add a guiding channel to steer the wave propagation.

Compression-based method: This method calculates tissue elastic properties by measuring the vibration amplitude induced by an actuator [117, 222, 223]. To generate a controlled vibration motion with a specific frequency, a ring piezo transducer will be attached to the imaging window in the outer plastic cover as illustrated in [**Figure 10.2 (b)]**. Through finite element modeling, we have demonstrated that the rapid bulk movement of the imaging window will generate a tissue vibration in the same direction as the applied force in which the vibration amplitude is correlated with the elasticity [224]. Therefore, we can apply piezo movement at 1 kHz with a travel range of ±10 μm to generate local tissue strain from the oscillation. To obtain a quantitative assessment of Young's modulus, we will use a calibration layer to measure local stress applied to the tissue. The calibration layer is made of transparent silicone with elasticity similar to the tissue, which will then be used to measure the force exerted by the PZR. To ensure complete contact with the tissue, we will apply a preload of 10-μm to the PZT.

Data acquisition: To produce 3D data, the piezo force will be exerted, and OCT data will be collected over multiple lines of sight. The wave propagation or vibration in tissue will be recorded using previously demonstrated M-mode methods. The Doppler OCT algorithm will be used to quantify the displacement, Δd, in the axis of excitation with high sensitivity, as described by the equation below [61, 63, 222, 223, 225]:

$$\Delta d = \frac{\Delta\varphi(z)}{4\pi n}\lambda \tag{10.1}$$

where $\varphi(z)$ is the Doppler phase shift at depth z between sequential scans calculated by Eq. (10.1) and n is the refractive index of the tissue. The shear wave propagation in 3D can be visualized over time with a single burst for every B-scan, and thus, the shear wave velocity $V_{x,z}$ can be measured for the 3D volume. The shear modulus, $\mu_{x,z}$, can be calculated from Eq. 10.2 [222, 226]:

$$\mu_{x,z} = \rho_{x,z} \cdot V_{x,z}^2 \tag{10.2}$$

10.2.3 Ultra-sensitive detection of airway epithelium damage based on cilia motion

In Chapter 7, we introduced a new imaging technique based on OCT to assess cilia beating motion. To demonstrate our methods, we investigated healthy cilia using different processing methods and acquisition parameters. In the future, we can evaluate the ciliary damage caused by foreign pathogens and toxic gases, including chlorine. Chlorine is a toxic chemical that has led to several mass poisonings caused by industrial accidents in the United States and globally, as well as being used as a chemical weapon in many recent conflicts. Since chlorine directly damages the lining of the upper airway, there is a possibility that cilia and mucociliary transport will be the first to get affected by the chemical exposure in the airway. If this hypothesis is proven to be true, we can use cilia to detect inhalation injury at an early stage and predict severity. Additionally, we can use cilia as indicators to find a region of intact tissue and selectively treat regions with more severe damage.

References

[1] D. Huang, J. Wang, C. P. Lin, C. A. Puliafito, and J. G. Fujimoto, "Micron-resolution ranging of cornea anterior chamber by optical reflectometry," *Lasers Surg. Med.*, vol. 11, no. 5, pp. 419–425, 1991, doi: 10.1002/lsm.1900110506.

[2] J. Fujimoto and E. Swanson, "The development, commercialization, and impact of optical coherence tomography," *Investigative Ophthalmology and Visual Science*, vol. 57, no. 9. Association for Research in Vision and Ophthalmology Inc., pp. OCT1–OCT13, 2016, doi: 10.1167/iovs.16-19963.

[3] P. Gill and R. V Martin, "Smoke inhalation injury," *BJA Educ.*, vol. 15, no. 3, pp. 143–148, Jun. 2015, doi: 10.1093/bjaceaccp/mku017.

[4] J. M. Albright, C. S. Davis, M. D. Bird, L. Ramirez, H. Kim, E. L. Burnham, R. L. Gamelli, and E. J. Kovacs, "The acute pulmonary inflammatory response to the graded severity of smoke inhalation injury.," *Crit. Care Med.*, vol. 40, no. 4, pp. 1113–21, Apr. 2012, doi: 10.1097/CCM.0b013e3182374a67.

[5] K. Gupta, M. Mehrotra, P. Kumar, A. R. Gogia, A. Prasad, and J. A. Fisher, "Smoke Inhalation Injury: Etiopathogenesis, Diagnosis, and Management.," *Indian J. Crit. Care Med.*, vol. 22, no. 3, pp. 180–188, Mar. 2018, doi: 10.4103/ijccm.IJCCM_460_17.

[6] D. J. Dries and F. W. Endorf, "Inhalation injury: epidemiology, pathology, treatment strategies.," *Scand. J. Trauma. Resusc. Emerg. Med.*, vol. 21, p. 31, Apr. 2013, doi: 10.1186/1757-7241-21-31.

[7] M. Gorguner and M. Akgun, "Acute Inhalation Injury," *Eurasian J. Med.*, vol. 42, no. 1, pp. 28–35, 2010, doi: 10.5152/eajm.2010.09.

[8] J. H. Sisson and D. J. Tuma, "Vapor phase exposure to acetaldehyde generated from ethanol inhibits bovine bronchial epithelial cell ciliary motility.," *Alcohol. Clin. Exp. Res.*, vol. 18, no. 5, pp. 1252–5, Oct. 1994, doi: 10.1111/J.1530-0277.1994.TB00114.X.

[9] I. Eckerman, *The Bhopal saga : causes and consequences of the world's largest industrial disaster*. Universities Press, 2005.

[10] G. A. Boorman, L. C. Uraih, B. N. Gupta, and J. R. Bucher, "Two-Hour Methyl Isocyanate Inhalation and 90-Day Recovery Study in B6C3F1 Mice," *Environ. Health Perspect.*, vol. 72, p. 63, Jun. 1987, doi: 10.2307/3430277.

[11] B. Nemery, D. Dinsdale, S. Sparrow, and D. E. Ray, "Effects of methyl isocyanate on the respiratory tract of rats," *Br. J. Ind. Med.*, vol. 42, pp. 799–805, 1985, doi: 10.1136/oem.42.12.799.

[12] Y. Miao, J. C. Jing, V. Desai, S. B. Mahon, M. Brenner, L. A. Veress, C. W. White, and Z. Chen, "Automated 3D segmentation of methyl isocyanate-exposed rat trachea using an ultra-thin, fully fiber optic optical coherence endoscopic probe," *Sci. Rep.*, vol. 8, no. 1, p. 8713, Dec. 2018, doi: 10.1038/s41598-018-26389-2.

[13] M. J. Hammer-Wilson, V. Nguyen, W.-G. Jung, Y. Ahn, Z. Chen, and P. Wilder-Smith, "Detection of vesicant-induced upper airway mucosa damage in the hamster cheek pouch model using optical coherence tomography.," *J. Biomed. Opt.*, vol. 15, no. 1, p. 016017, 2010, doi: 10.1117/1.3309455.

[14] K. A. Kreuter, S. B. Mahon, D. S. Mukai, J. Su, W.-G. Jung, N. Narula, S. Guo, N. Wakida, C. Raub, M. W. Berns, S. C. George, Z. Chen, and M. Brenner, "Detection and monitoring of early airway injury effects of half-mustard (2-chloroethylethylsulfide) exposure using high-resolution optical coherence tomography.," *J. Biomed. Opt.*, vol. 14, no. 4, p. 044037, 2009, doi: 10.1117/1.3210775.

[15] P. F. Walker, M. F. Buehner, L. A. Wood, N. L. Boyer, I. R. Driscoll, J. B. Lundy, L. C. Cancio, and K. K. Chung, "Diagnosis and management of inhalation injury: An updated review," *Crit. Care*, vol. 19, no. 1, pp. 1–12, 2015, doi: 10.1186/s13054-015-1077-4.

[16] J. H. Choi, L.-D. Chou, T. R. Roberts, B. M. Beely, D. S. Wendorff, M. D. Espinoza, K. Sieck, A. T. Dixon, D. Burmeister, B. S. Jordan, M. Brenner, Z. Chen, C. Necsoiu, L. C. Cancio, and A. I. Batchinsky, "Point-of-care endoscopic optical coherence tomography detects changes in mucosal thickness in ARDS due to smoke inhalation and burns," *Burns*, vol. 45, no. 3, pp. 589–597, Nov. 2018, doi: 10.1016/J.BURNS.2018.10.014.

[17] L. Chou, A. Batchinsky, S. Belenkiy, J. Jing, T. Ramalingam, M. Brenner, and Z. Chen, "In vivo detection of inhalation injury in large airway using three-dimensional long-range swept-source optical coherence tomography.," *J. Biomed. Opt.*, vol. 19, no. 3, p. 36018, Mar. 2014, doi: 10.1117/1.JBO.19.3.036018.

[18] M. Brenner, K. Kreuter, J. Ju, S. Mahon, L. Tseng, and D. Mukai, "In vivo optical coherence tomography detection of differences in regional large airway smoke inhalation induced injury in a rabbit model," *Control*, vol. 13, no. 3, pp. 1–15, 2009, doi: 10.1117/1.2939400.In.

[19] S.-W. Lee, A. E. Heidary, D. Yoon, D. Mukai, T. Ramalingam, S. Mahon, J. Yin, J. Jing, G. Liu, Z. Chen,

and M. Brenner, “Quantification of airway thickness changes in smoke-inhalation injury using in-vivo 3-D endoscopic frequency-domain optical coherence tomography.,” *Biomed. Opt. Express*, vol. 2, no. 2, pp. 243–54, 2011, doi: 10.1364/BOE.2.000243.

[20] M. Brenner, K. Kreuter, D. Mukai, T. Burney, S. Guo, J. Su, S. Mahon, A. Tran, L. Tseng, J. Ju, and Z. Chen, “Detection of acute smoke-induced airway injury in a New Zealand white rabbit model using optical coherence tomography,” *J. Biomed. Opt.*, vol. 12, no. 5, p. 051701, 2007, doi: 10.1117/1.2798637.

[21] J. Yin, G. Liu, J. Zhang, L. Yu, S. Mahon, D. Mukai, M. Brenner, and Z. Chen, “In vivo early detection of smoke-induced airway injury using three-dimensional swept-source optical coherence tomography.,” *J. Biomed. Opt.*, vol. 14, no. 6, p. 060503, 2009, doi: 10.1117/1.3268775.

[22] G. K. Sharma, G. S. Ahuja, M. Wiedmann, K. E. Osann, E. Su, A. E. Heidari, J. C. Jing, Y. Qu, F. Lazarow, A. Wang, L. Chou, C. C. Uy, V. Dhar, J. P. Cleary, N. Pham, K. Huoh, Z. Chen, and B. J.-F. Wong, “Long-Range Optical Coherence Tomography of the Neonatal Upper Airway for Early Diagnosis of Intubation-related Subglottic Injury.,” *Am. J. Respir. Crit. Care Med.*, vol. 192, no. 12, pp. 1504–13, Dec. 2015, doi: 10.1164/rccm.201501-0053OC.

[23] J. H. Walsh, M. S. Leigh, A. Paduch, K. J. Maddison, D. L. Philippe, J. J. Armstrong, D. D. Sampson, D. R. Hillman, and P. R. Eastwood, “Evaluation of pharyngeal shape and size using anatomical optical coherence tomography in individuals with and without obstructive sleep apnoea,” *J. Sleep Res.*, vol. 17, no. 2, pp. 230–238, Jun. 2008, doi: 10.1111/j.1365-2869.2008.00647.x.

[24] M. S. Leigh, J. J. Armstrong, A. Paduch, J. H. Walsh, D. R. Hillman, P. R. Eastwood, and D. D. Sampson, “Anatomical Optical Coherence Tomography for Long-Term, Portable, Quantitative Endoscopy,” *IEEE Trans. Biomed. Eng.*, vol. 55, no. 4, pp. 1438–1446, Apr. 2008, doi: 10.1109/TBME.2007.913409.

[25] J. C. Jing, L. Chou, E. Su, B. J. F. Wong, and Z. Chen, “Anatomically correct visualization of the human upper airway using a high-speed long range optical coherence tomography system with an integrated positioning sensor,” *Sci. Rep.*, vol. 6, no. December, p. 39443, 2016, doi: 10.1038/srep39443.

[26] J. Jing, J. Zhang, A. C. Loy, B. J. F. Wong, and Z. Chen, “High-speed upper-airway imaging using full-range optical coherence tomography,” *J. Biomed. Opt.*, vol. 17, no. 11, p. 110507, 2012, doi: 10.1117/1.JBO.17.11.110507.

[27] G. J. Tearney, M. E. Brezinski, B. E. Bouma, S. A. Boppart, C. Pitris, J. F. Southern, and J. G. Fujimoto, “In vivo endoscopic optical biopsy with optical coherence tomography.,” *Science*, vol. 276, no. 5321, pp. 2037–9, Jun. 1997, doi: 10.1126/SCIENCE.276.5321.2037.

[28] L. Chou, A. Batchinsky, S. Belenkiy, J. Jing, T. Ramalingam, M. Brenner, and Z. Chen, “*In vivo* detection of inhalation injury in large airway using three-dimensional long-range swept-source optical coherence tomography,” *J. Biomed. Opt.*, vol. 19, no. 3, p. 036018, 2014, doi: 10.1117/1.JBO.19.3.036018.

[29] C. Robertson, S.-W. Lee, Y.-C. Ahn, S. Mahon, Z. Chen, M. Brenner, and S. C. George, “Investigating in vivo airway wall mechanics during tidal breathing with optical coherence tomography,” *J. Biomed. Opt.*, vol. 16, no. 10, p. 106011, Oct. 2011, doi: 10.1117/1.3642006.

[30] R. Bu, S. Balakrishnan, N. Iftimia, H. Price, C. Zdanski, and A. L. Oldenburg, “Airway compliance measured by anatomic optical coherence tomography.,” *Biomed. Opt. Express*, vol. 8, no. 4, pp. 2195–2209, Apr. 2017, doi: 10.1364/BOE.8.002195.

[31] S. Balakrishnan, R. Bu, N. Iftimia, H. Price, C. Zdanski, and A. L. Oldenburg, “Combined anatomical optical coherence tomography and intraluminal pressure reveal viscoelasticity of the in vivo airway,” *J. Biomed. Opt.*, vol. 23, no. 10, p. 1, Oct. 2018, doi: 10.1117/1.JBO.23.10.100501.

[32] R. A. McLaughlin, J. P. Williamson, M. J. Phillips, J. J. Armstrong, S. Becker, D. R. Hillman, P. R. Eastwood, and D. D. Sampson, “Applying anatomical optical coherence tomography to quantitative 3D imaging of the lower airway,” *Opt. Express*, vol. 16, no. 22, p. 17521, Oct. 2008, doi: 10.1364/OE.16.017521.

[33] J. Zhang, W. Jung, J. S. Nelson, and Z. Chen, “Full range polarization-sensitive Fourier domain optical coherence tomography,” *Opt. Express*, vol. 12, no. 24, p. 6033, Nov. 2004, doi: 10.1364/OPEX.12.006033.

[34] T. Klein, W. Wieser, L. Reznicek, A. Neubauer, A. Kampik, and R. Huber, “Multi-MHz retinal OCT,” *Biomed. Opt. Express*, vol. 4, no. 10, p. 1890, Oct. 2013, doi: 10.1364/BOE.4.001890.

[35] D. Cui, K. K. Chu, B. Yin, T. N. Ford, C. Hyun, H. M. Leung, J. A. Gardecki, G. M. Solomon, S. E. Birket, L. Liu, S. M. Rowe, and G. J. Tearney, “Flexible, high-resolution micro-optical coherence tomography endobronchial probe toward in vivo imaging of cilia,” *Opt. Lett.*, vol. 42, no. 4, p. 867, Feb. 2017, doi: 10.1364/OL.42.000867.

[36] J. S. Iyer, S. A. Batts, K. K. Chu, M. I. Sahin, H. M. Leung, G. J. Tearney, and K. M. Stankovic, “Micro-optical coherence tomography of the mammalian cochlea,” *Sci. Rep.*, vol. 6, no. April, p. 33288, 2016, doi:

10.1038/srep33288.
[37] Y. Zhao, Z. Chen, C. Saxer, S. Xiang, J. F. de Boer, and J. S. Nelson, “Phase-resolved optical coherence tomography and optical Doppler tomography for imaging blood flow in human skin with fast scanning speed and high velocity sensitivity,” *Opt. Lett.*, vol. 25, no. 2, p. 114, Jan. 2000, doi: 10.1364/OL.25.000114.
[38] Z. Chen, T. E. Milner, D. Dave, and J. Stuart Nelson, “Optical Doppler tomographic imaging of fluid flow velocity in highly scattering media,” 1997.
[39] Zhongping Chen, Yonghua Zhao, S. M. Srinivas, J. S. Nelson, N. Prakash, and R. D. Frostig, “Optical Doppler tomography,” *IEEE J. Sel. Top. Quantum Electron.*, vol. 5, no. 4, pp. 1134–1142, 1999, doi: 10.1109/2944.796340.
[40] D. Huang, E. A. Swanson, C. P. Lin, J. S. Schuman, W. G. Stinson, W. Chang, M. R. Hee, T. Flotte, K. Gregory, C. A. Puliafito, and J. G. Fujimoto, “Optical coherence tomography,” *Science (80-.).*, vol. 254, no. 5035, pp. 1178–1181, 1991, doi: 10.1126/science.1957169.
[41] R. C. Youngquist, S. Carr, and D. E. N. Davies, “Optical coherence-domain reflectometry: a new optical evaluation technique,” *Opt. Lett.*, vol. 12, no. 3, p. 158, Mar. 1987, doi: 10.1364/ol.12.000158.
[42] J. Ballif, R. Gianotti, P. Chavanne, R. Wälti, and R. P. Salathé, “Rapid and scalable scans at 21 m/s in optical low-coherence reflectometry,” *Opt. Lett.*, vol. 22, no. 11, p. 757, Jun. 1997, doi: 10.1364/ol.22.000757.
[43] C. B. Su, “Achieving variation of the optical path length by a few millimeters at millisecond rates for imaging of turbid media and optical interferometry: a new technique,” *Opt. Lett.*, vol. 22, no. 10, p. 665, May 1997, doi: 10.1364/ol.22.000665.
[44] K. F. Kwong, D. Yankelevich, K. C. Chu, J. P. Heritage, and A. Dienes, “400-Hz mechanical scanning optical delay line,” *Opt. Lett.*, vol. 18, no. 7, p. 558, Apr. 1993, doi: 10.1364/ol.18.000558.
[45] G. J. Tearney, B. E. Bouma, and J. G. Fujimoto, “High-speed phase- and group-delay scanning with a grating-based phase control delay line,” *Opt. Lett.*, vol. 22, no. 23, p. 1811, Dec. 1997, doi: 10.1364/ol.22.001811.
[46] A. F. Fercher, C. K. Hitzenberger, G. Kamp, and S. Y. El-Zaiat, “Measurement of intraocular distances by backscattering spectral interferometry,” *Opt. Commun.*, vol. 117, no. 1–2, pp. 43–48, May 1995, doi: 10.1016/0030-4018(95)00119-S.
[47] A. F. Fercher, “Optical coherence tomography,” *J. Biomed. Opt.*, vol. 1, no. 2, p. 157, 1996, doi: 10.1117/12.231361.
[48] M. Choma, M. Sarunic, C. Yang, and J. Izatt, “Sensitivity advantage of swept source and Fourier domain optical coherence tomography,” *Opt. Express*, vol. 11, no. 18, p. 2183, Sep. 2003, doi: 10.1364/oe.11.002183.
[49] R. Leitgeb, C. Hitzenberger, and A. Fercher, “Performance of fourier domain vs time domain optical coherence tomography,” *Opt. Express*, vol. 11, no. 8, p. 889, Apr. 2003, doi: 10.1364/oe.11.000889.
[50] J. F. de Boer, B. Cense, B. H. Park, M. C. Pierce, G. J. Tearney, and B. E. Bouma, “Improved signal-to-noise ratio in spectral-domain compared with time-domain optical coherence tomography,” *Opt. Lett.*, vol. 28, no. 21, p. 2067, Nov. 2003, doi: 10.1364/ol.28.002067.
[51] M. Wojtkowski, R. Leitgeb, A. Kowalczyk, T. Bajraszewski, and A. F. Fercher, “In vivo human retinal imaging by Fourier domain optical coherence tomography,” *J. Biomed. Opt.*, vol. 7, no. 3, p. 457, 2002, doi: 10.1117/1.1482379.
[52] J. Xi, L. Huo, J. Li, and X. Li, “Generic real-time uniform K-space sampling method for high-speed swept-source optical coherence tomography.,” *Opt. Express*, vol. 18, no. 9, pp. 9511–7, 2010, doi: 10.1364/OE.18.009511.
[53] C. K. Hitzenberger, A. Baumgartner, W. Drexler, and A. F. Fercher, “Dispersion Effects in Partial Coherence Interferometry: Implications for Intraocular Ranging,” *J. Biomed. Opt.*, vol. 4, no. 1, p. 144, 1999, doi: 10.1117/1.429900.
[54] A. Fercher, C. Hitzenberger, M. Sticker, R. Zawadzki, B. Karamata, and T. Lasser, “Numerical dispersion compensation for Partial Coherence Interferometry and Optical Coherence Tomography,” *Opt. Express*, vol. 9, no. 12, p. 610, Dec. 2001, doi: 10.1364/OE.9.000610.
[55] J. Zhang, J. S. Nelson, and Z. Chen, “Removal of a mirror image and enhancement of the signal-to-noise ratio in Fourier-domain optical coherence tomography using an electro-optic phase modulator.,” *Opt. Lett.*, vol. 30, no. 2, pp. 147–149, 2005, doi: 10.1364/OL.30.000147.
[56] Y. Zhao, Z. Chen, C. Saxer, S. Xiang, J. F. de Boer, and J. S. Nelson, “Phase-resolved optical coherence tomography and optical Doppler tomography for imaging blood flow in human skin with fast scanning

speed and high velocity sensitivity," *Opt. Lett.*, vol. 25, no. 2, p. 114, Jan. 2000, doi: 10.1364/ol.25.000114.
[57] Z. Chen and J. Zhang, "Doppler Optical Coherence Tomography," Springer, Berlin, Heidelberg, 2008, pp. 621–651.
[58] Z. Chen, T. E. Milner, S. Srinivas, X. Wang, A. Malekafzali, M. J. C. van Gemert, and J. S. Nelson, "Noninvasive imaging of in vivo blood flow velocity using optical Doppler tomography," *Opt. Lett.*, vol. 22, no. 14, p. 1119, Jul. 1997, doi: 10.1364/OL.22.001119.
[59] J. A. Izatt, M. D. Kulkarni, S. Yazdanfar, J. K. Barton, and A. J. Welch, "In vivo bidirectional color Doppler flow imaging of picoliter blood volumes using optical coherence tomography.," *Opt. Lett.*, vol. 22, no. 18, pp. 1439–41, Sep. 1997.
[60] V. X. D. Yang, M. L. Gordon, A. Mok, Y. Zhao, Z. Chen, R. S. C. Cobbold, B. C. Wilson, I. A. Vitkin, and P. Program, "Improved phase-resolved optical Doppler tomography using the Kasai velocity estimator and histogram segmentation," 2002.
[61] Y. Zhao, Z. Chen, C. Saxer, Q. Shen, S. Xiang, J. F. de Boer, and J. S. Nelson, "Doppler standard deviation imaging for clinical monitoring of in vivo human skin blood flow," *Opt. Lett.*, vol. 25, no. 18, p. 1358, Sep. 2000, doi: 10.1364/OL.25.001358.
[62] H. Ren, K. M. Brecke, Z. Ding, Y. Zhao, J. S. Nelson, and Z. Chen, "Imaging and quantifying transverse flow velocity with the Doppler bandwidth in a phase-resolved functional optical coherence tomography," *Opt. Lett.*, vol. 27, no. 6, p. 409, Mar. 2002, doi: 10.1364/ol.27.000409.
[63] G. Liu, L. Chou, W. Jia, W. Qi, B. Choi, and Z. Chen, "Intensity-based modified Doppler variance algorithm: application to phase instable and phase stable optical coherence tomography systems.," *Opt. Express*, vol. 19, no. 12, pp. 11429–40, Jun. 2011.
[64] L. Qi, K. Zheng, X. Li, Q. Feng, Z. Chen, and W. Chen, "Automatic three-dimensional segmentation of endoscopic airway OCT images," *Biomed. Opt. Express*, vol. 10, no. 2, p. 642, Feb. 2019, doi: 10.1364/BOE.10.000642.
[65] L. Qi, S. Huang, A. E. Heidari, C. Dai, J. Zhu, X. Zhang, and Z. Chen, "Automatic airway wall segmentation and thickness measurement for long-range optical coherence tomography images," *Opt. Express*, vol. 23, no. 26, pp. 33992–34006, 2015, doi: 10.1364/OE.23.033992.
[66] M. Heydarian, S. Choy, A. Wheatley, D. McCormack, H. O. Coxson, S. Lam, and G. Parraga, "Automated segmentation of lung airway wall area measurements from bronchoscopic optical coherence tomography imaging," vol. 7965, p. 79651M, Mar. 2011, doi: 10.1117/12.878194.
[67] A. M. D. Lee, M. Kirby, K. Ohtani, T. Candido, R. Shalansky, C. MacAulay, J. English, R. Finley, S. Lam, H. O. Coxson, and P. Lane, "Validation of Airway Wall Measurements by Optical Coherence Tomography in Porcine Airways," *PLoS One*, vol. 9, no. 6, p. e100145, Jun. 2014, doi: 10.1371/journal.pone.0100145.
[68] D. C. Adams, H. Pahlevaninezhad, M. V. Szabari, J. L. Cho, D. L. Hamilos, M. Kesimer, R. C. Boucher, A. D. Luster, B. D. Medoff, and M. J. Suter, "Automated segmentation and quantification of airway mucus with endobronchial optical coherence tomography," *Biomed. Opt. Express*, vol. 8, no. 10, p. 4729, 2017, doi: 10.1364/BOE.8.004729.
[69] P. Puvanathasan and K. Bizheva, "Speckle noise reduction algorithm for optical coherence tomography based on interval type II fuzzy set," *Opt. Express*, vol. 15, no. 24, p. 15747, Nov. 2007, doi: 10.1364/oe.15.015747.
[70] M. Kirby, A. M. D. Lee, T. Candido, C. MacAulay, P. Lane, S. Lam, and H. O. Coxson, "Automated segmentation of porcine airway wall layers using optical coherence tomography: comparison with manual segmentation and histology," Mar. 2014, vol. 8927, p. 89271D, doi: 10.1117/12.2040866.
[71] D. A. C. A. Dams, H. A. P. Ahlevaninezhad, M. A. V. S. Zabari, J. O. L. C. Ho, D. A. L. H. Amilos, M. E. K. Esimer, R. Ichard, C. B. Oucher, A. N. D. L. Uster, B. E. D. M. Edoff, and M. E. J. S. Uter, "Automated segmentation and quantification of airway mucus with endobronchial optical coherence tomography," vol. 8, no. 10, pp. 4729–4741, 2017.
[72] L. Qi, K. Zheng, X. Li, Q. Feng, Z. Chen, and A. W. Chen, "Automatic three-dimensional segmentation of endoscopic airway OCT images," vol. 10, no. 2, pp. 642–656, 2019, doi: 10.1364/BOE.10.000642.
[73] M. D. Abràmoff, P. T. Lavin, M. Birch, N. Shah, and J. C. Folk, "Pivotal trial of an autonomous AI-based diagnostic system for detection of diabetic retinopathy in primary care offices," *npj Digit. Med.*, vol. 1, no. 1, Dec. 2018, doi: 10.1038/s41746-018-0040-6.
[74] J. De Fauw *et al.*, "Clinically applicable deep learning for diagnosis and referral in retinal disease," *Nat. Med.*, vol. 24, no. 9, pp. 1342–1350, Sep. 2018, doi: 10.1038/s41591-018-0107-6.
[75] F. Li, H. Chen, Z. Liu, X. Zhang, and Z. Wu, "Fully automated detection of retinal disorders by image-based deep learning," *Graefe's Arch. Clin. Exp. Ophthalmol.*, vol. 257, no. 3, pp. 495–505, Mar. 2019, doi:

10.1007/s00417-018-04224-8.
[76] T. Schlegl, S. M. Waldstein, H. Bogunovic, F. Endstraßer, A. Sadeghipour, A. M. Philip, D. Podkowinski, B. S. Gerendas, G. Langs, and U. Schmidt-Erfurth, "Fully Automated Detection and Quantification of Macular Fluid in OCT Using Deep Learning," *Ophthalmology*, vol. 125, no. 4, pp. 549–558, Apr. 2018, doi: 10.1016/j.ophtha.2017.10.031.
[77] S. K. Devalla, P. K. Renukanand, B. K. Sreedhar, G. Subramanian, L. Zhang, S. Perera, J.-M. Mari, K. S. Chin, T. A. Tun, N. G. Strouthidis, T. Aung, A. H. Thiéry, and M. J. A. Girard, "DRUNET: a dilated-residual U-Net deep learning network to segment optic nerve head tissues in optical coherence tomography images," *Biomed. Opt. Express*, vol. 9, no. 7, p. 3244, Jul. 2018, doi: 10.1364/boe.9.003244.
[78] H. Fu, M. Baskaran, Y. Xu, S. Lin, D. W. K. Wong, J. Liu, T. A. Tun, M. Mahesh, S. A. Perera, and T. Aung, "A Deep Learning System for Automated Angle-Closure Detection in Anterior Segment Optical Coherence Tomography Images," *Am. J. Ophthalmol.*, vol. 203, pp. 37–45, Jul. 2019, doi: 10.1016/j.ajo.2019.02.028.
[79] S. J. Chiu, X. T. Li, P. Nicholas, C. A. Toth, J. A. Izatt, and S. Farsiu, "Automatic segmentation of seven retinal layers in SDOCT images congruent with expert manual segmentation," *Opt. Express*, vol. 18, no. 18, p. 19413, Aug. 2010, doi: 10.1364/oe.18.019413.
[80] S. Huang, Z. Piao, J. Zhu, F. Lu, and Z. Chen, "*In vivo* microvascular network imaging of the human retina combined with an automatic three-dimensional segmentation method," *J. Biomed. Opt.*, vol. 20, no. 7, p. 076003, Jul. 2015, doi: 10.1117/1.JBO.20.7.076003.
[81] J. Tian, P. Marziliano, M. Baskaran, T. A. Tun, and T. Aung, "Automatic segmentation of the choroid in enhanced depth imaging optical coherence tomography images," *Biomed. Opt. Express*, vol. 4, no. 3, p. 397, Mar. 2013, doi: 10.1364/boe.4.000397.
[82] S. J. Chiu, C. A. Toth, C. Bowes Rickman, J. A. Izatt, and S. Farsiu, "Automatic segmentation of closed-contour features in ophthalmic images using graph theory and dynamic programming," *Biomed. Opt. Express*, vol. 3, no. 5, p. 1127, May 2012, doi: 10.1364/boe.3.001127.
[83] F. LaRocca, S. J. Chiu, R. P. McNabb, A. N. Kuo, J. A. Izatt, and S. Farsiu, "Robust automatic segmentation of corneal layer boundaries in SDOCT images using graph theory and dynamic programming," *Biomed. Opt. Express*, vol. 2, no. 6, p. 1524, Jun. 2011, doi: 10.1364/boe.2.001524.
[84] J. Jing, J. Zhang, A. C. Loy, B. J. F. Wong, and Z. Chen, "High-speed upper-airway imaging using full-range optical coherence tomography.," *J. Biomed. Opt.*, vol. 17, no. 11, p. 110507, Nov. 2012, doi: 10.1117/1.JBO.17.11.110507.
[85] D. C. Cires¸ancires¸an, A. Giusti, L. M. Gambardella, and J. ¨ Urgen Schmidhuber, "Deep Neural Networks Segment Neuronal Membranes in Electron Microscopy Images."
[86] O. Ronneberger, P. Fischer, and T. Brox, "U-net: Convolutional networks for biomedical image segmentation," in *Lecture Notes in Computer Science (including subseries Lecture Notes in Artificial Intelligence and Lecture Notes in Bioinformatics)*, 2015, vol. 9351, pp. 234–241, doi: 10.1007/978-3-319-24574-4_28.
[87] I. Rizwan I Haque and J. Neubert, "Deep learning approaches to biomedical image segmentation," *Informatics in Medicine Unlocked*, vol. 18. Elsevier Ltd, p. 100297, Jan. 01, 2020, doi: 10.1016/j.imu.2020.100297.
[88] A. Fedorov, R. Beichel, J. Kalpathy-Cramer, J. Finet, J.-C. Fillion-Robin, S. Pujol, C. Bauer, D. Jennings, F. Fennessy, M. Sonka, J. Buatti, S. Aylward, J. V Miller, S. Pieper, and R. Kikinis, "3D Slicer as an image computing platform for the Quantitative Imaging Network.," *Magn. Reson. Imaging*, vol. 30, no. 9, pp. 1323–41, Nov. 2012, doi: 10.1016/j.mri.2012.05.001.
[89] R. Kikinis, S. D. Pieper, and K. G. Vosburgh, "3D Slicer: A Platform for Subject-Specific Image Analysis, Visualization, and Clinical Support," in *Intraoperative Imaging and Image-Guided Therapy*, New York, NY: Springer New York, 2014, pp. 277–289.
[90] D. A. Jett and D. T. Yeung, "The CounterACT Research Network Basic Mechanisms and Practical Applications," *Proc Am Thorac Soc.*, vol. 4, pp. 254–6, 2010, doi: 10.1513/pats.201001-003SM.
[91] V. R. Dhara and R. Dhara, "The Union Carbide Disaster in Bhopal: A Review of Health Effects," *Arch. Environ. Heal. An Int. J.*, vol. 57, no. 5, pp. 391–404, Sep. 2002, doi: 10.1080/00039890209601427.
[92] B. F. Bessac, M. Sivula, C. A. von Hehn, A. I. Caceres, J. Escalera, and S.-E. Jordt, "Transient receptor potential ankyrin 1 antagonists block the noxious effects of toxic industrial isocyanates and tear gases.," *FASEB J.*, vol. 23, no. 4, pp. 1102–14, Apr. 2009, doi: 10.1096/fj.08-117812.
[93] S. G. Entelis and O. V Nesterov, "Kinetics and mechanism of the reactions of isocyanates with compounds containing 'active' hydrogen," *Russ. Chem. Rev.*, vol. 35, no. 12, pp. 917–930, Dec. 1966, doi:

10.1070/RC1966v035n12ABEH001555.
[94] M. R. Fedde, D. E. Dodd, C. M. Troup, and E. H. Fowler, “Biological effects of short-term, high-concentration exposure to methyl isocyanate. III. Influence on gas exchange in the guinea pig lung.,” *Environ. Health Perspect.*, vol. 72, pp. 29–33, Jun. 1987.
[95] Y. ALARIE, “Arterial blood gas measurements in guinea pigs and inspired CO2 concentrations for ventilatory performance challenges,” *Fundam. Appl. Toxicol.*, vol. 11, no. 2, pp. 268–276, Aug. 1988, doi: 10.1016/0272-0590(88)90151-0.
[96] Y.-C. Kim, R. M. Lebel, Z. Wu, S. L. D. Ward, M. C. K. Khoo, and K. S. Nayak, “Real-time 3D magnetic resonance imaging of the pharyngeal airway in sleep apnea,” *Magn. Reson. Med.*, vol. 71, no. 4, pp. 1501–1510, Apr. 2014, doi: 10.1002/mrm.24808.
[97] N. A. Alsufyani, M. A. Q. Al-Saleh, and P. W. Major, “CBCT assessment of upper airway changes and treatment outcomes of obstructive sleep apnoea: a systematic review,” *Sleep Breath.*, vol. 17, no. 3, pp. 911–923, Sep. 2013, doi: 10.1007/s11325-012-0799-7.
[98] W. Liao, T. Chen, C. Wang, W. Zhang, Z. Peng, X. Zhang, S. Ai, D. Fu, T. Zhou, and P. Xue, “Endoscopic optical coherence tomography with a focus-adjustable probe.,” *Opt. Lett.*, vol. 42, no. 20, pp. 4040–4043, Oct. 2017.
[99] F. Benboujja, J. A. Garcia, K. Beaudette, M. Strupler, C. J. Hartnick, and C. Boudoux, “Intraoperative imaging of pediatric vocal fold lesions using optical coherence tomography,” *J. Biomed. Opt.*, vol. 21, no. 1, p. 016007, 2016, doi: 10.1117/1.JBO.21.1.016007.
[100] P. B. Noble, A. R. West, R. A. McLaughlin, J. J. Armstrong, S. Becker, P. K. McFawn, J. P. Williamson, P. R. Eastwood, D. R. Hillman, D. D. Sampson, and H. W. Mitchell, “Airway narrowing assessed by anatomical optical coherence tomography in vitro: dynamic airway wall morphology and function,” *J. Appl. Physiol.*, vol. 108, no. 2, pp. 401–411, Feb. 2010, doi: 10.1152/japplphysiol.00511.2009.
[101] J. P. Williamson, J. J. Armstrong, R. A. McLaughlin, P. B. Noble, A. R. West, S. Becker, A. Curatolo, W. J. Noffsinger, H. W. Mitchell, M. J. Phillips, D. D. Sampson, D. R. Hillman, and P. R. Eastwood, “Measuring airway dimensions during bronchoscopy using anatomical optical coherence tomography,” *Eur. Respir. J.*, vol. 35, no. 1, 2009.
[102] A. Monteiro and R. L. Smith, “Bronchial tree Architecture in Mammals of Diverse Body Mass,” *Int. J. Morphol.*, vol. 32, no. 1, pp. 312–316, Mar. 2014, doi: 10.4067/S0717-95022014000100050.
[103] J. Lee, Y. Chae, Y.-C. Ahn, and S. Moon, “Ultra-thin and flexible endoscopy probe for optical coherence tomography based on stepwise transitional core fiber,” *Biomed. Opt. Express*, vol. 6, no. 5, p. 1782, 2015, doi: 10.1364/BOE.6.001782.
[104] S. Moon, Z. Piao, C.-S. Kim, and Z. Chen, “Lens-free endoscopy probe for optical coherence tomography,” *Opt. Lett.*, vol. 38, no. 12, p. 2014, Jun. 2013, doi: 10.1364/OL.38.002014.
[105] L. Qi, S. Huang, A. E. Heidari, C. Dai, J. Zhu, and Z. Chen, “Automatic airway wall segmentation and thickness measurement for long-range optical coherence tomography images,” *Opt. Express*, vol. 23, no. 26, pp. 147–149, 2015, doi: 10.1364/OE.23.033992.
[106] J. I. Z. Hang, W. U. Y. Uan, W. E. L. Iang, S. Y. U. Hanyong, Y. A. L. Iang, Z. X. U. Hiyong, Y. U. W. Ei, and X. L. I. Ingde, “Automatic and robust segmentation of endoscopic OCT images and optical staining,” *Biomed. Opt. Express*, vol. 8, no. 5, pp. 679–687, 2017.
[107] L. A. Veress, D. R. Anderson, T. B. Hendry-Hofer, P. R. Houin, J. S. Rioux, R. B. Garlick, J. E. Loader, D. C. Paradiso, R. W. Smith, R. C. Rancourt, W. W. Holmes, and C. W. White, “Airway tissue plasminogen activator prevents acute mortality due to lethal sulfur mustard inhalation.,” *Toxicol. Sci.*, vol. 143, no. 1, pp. 178–84, Jan. 2015, doi: 10.1093/toxsci/kfu225.
[108] L. A. Veress, T. B. Hendry-Hofer, J. E. Loader, J. S. Rioux, R. B. Garlick, and C. W. White, “Tissue plasminogen activator prevents mortality from sulfur mustard analog-induced airway obstruction,” *Am. J. Respir. Cell Mol. Biol.*, vol. 48, no. 4, pp. 439–447, 2013, doi: 10.1165/rcmb.2012-0177OC.
[109] W. S. Beckett, “Persistent respiratory effects in survivors of the Bhopal disaster.,” *Thorax*, vol. 53 Suppl 2, no. suppl 2, pp. S43-6, Aug. 1998, doi: 10.1136/THX.53.2008.S43.
[110] M. A. Stevens, S. Fitzgerald, M. G. Ménache, D. L. Costa, and J. R. Bucher, “Functional evidence of persistent airway obstruction in rats following a two-hour inhalation exposure to methyl isocyanate.,” *Environ. Health Perspect.*, vol. 72, pp. 89–94, Jun. 1987.
[111] X. Yan, J. J. Polo Carbayo, E. R. Weibel, and C. C. W. Hsia, “Variation of lung volume after fixation when measured by immersion or Cavalieri method,” *Am. J. Physiol. - Lung Cell. Mol. Physiol.*, vol. 284, no. 1, 2003.
[112] S. Lee, M. W. Lee, H. S. Cho, J. W. Song, H. S. Nam, D. J. Oh, K. Park, W.-Y. Oh, H. Yoo, and J. W. Kim,

"Fully integrated high-speed intravascular optical coherence tomography/near-infrared fluorescence structural/molecular imaging in vivo using a clinically available near-infrared fluorescence-emitting indocyanine green to detect inflamed lipid-rich atherom," *Circ. Cardiovasc. Interv.*, vol. 7, no. 4, 2014.

[113] Y. Li, J. Jing, Y. Qu, Y. Miao, B. Zhang, T. Ma, M. Yu, Q. Zhou, and Z. Chen, "Fully integrated optical coherence tomography, ultrasound, and indocyanine green-based fluorescence tri-modality system for intravascular imaging.," *Biomed. Opt. Express*, vol. 8, no. 2, pp. 1036–1044, Feb. 2017, doi: 10.1364/BOE.8.001036.

[114] W. Yuan, R. Brown, W. Mitzner, L. Yarmus, and X. Li, "Super-achromatic monolithic microprobe for ultrahigh-resolution endoscopic optical coherence tomography at 800 nm," *Nat. Commun.*, vol. 8, no. 1, p. 1531, Dec. 2017, doi: 10.1038/s41467-017-01494-4.

[115] Y. Li, J. Jing, E. Heidari, J. Zhu, Y. Qu, and Z. Chen, "Intravascular Optical Coherence Tomography for Characterization of Atherosclerosis with a 1.7 Micron Swept-Source Laser," *Sci. Rep.*, vol. 7, no. 1, p. 14525, Dec. 2017, doi: 10.1038/s41598-017-15326-4.

[116] J. Zhu, L. Qi, Y. Miao, T. Ma, C. Dai, Y. Qu, Y. He, Y. Gao, Q. Zhou, and Z. Chen, "3D mapping of elastic modulus using shear wave optical micro-elastography," *Sci. Rep.*, vol. 6, no. 1, p. 35499, 2016, doi: 10.1038/srep35499.

[117] Y. Qu, T. Ma, Y. He, J. Zhu, C. Dai, M. Yu, S. Huang, F. Lu, K. K. Shung, Q. Zhou, and Z. Chen, "Acoustic Radiation Force Optical Coherence Elastography of Corneal Tissue," *IEEE J. Sel. Top. Quantum Electron.*, vol. 22, no. c, pp. 1–1, 2016, doi: 10.1109/JSTQE.2016.2524618.

[118] Y. Miao, J. H. Choi, L.-D. Chou, V. Desai, T. R. Roberts, B. M. Beely, D. S. Wendorff, M. Espinoza, K. Sieck, L. C. Cancio, M. Brenner, A. I. Batchinsky, and Z. Chen, "Automatic Proximal Airway Volume Segmentation Using Optical Coherence Tomography for Assessment of Inhalation Injury," *J. Trauma Acute Care Surg.*, p. 1, Apr. 2019, doi: 10.1097/TA.0000000000002277.

[119] M. M. Taylor, "ARDS diagnosis and management: implications for the critical care nurse.," *Dimens. Crit. Care Nurs.*, vol. 24, no. 5, pp. 197–207.

[120] ARDS Definition Task Force, V. M. Ranieri, G. D. Rubenfeld, B. T. Thompson, N. D. Ferguson, E. Caldwell, E. Fan, L. Camporota, and A. S. Slutsky, "Acute Respiratory Distress Syndrome: the Berlin Definition," *JAMA*, vol. 307, no. 23, pp. 2526–33, Jun. 2012, doi: 10.1001/jama.2012.5669.

[121] V. Fanelli, A. Vlachou, S. Ghannadian, U. Simonetti, A. S. Slutsky, and H. Zhang, "Acute respiratory distress syndrome: new definition, current and future therapeutic options.," *J. Thorac. Dis.*, vol. 5, no. 3, pp. 326–34, Jun. 2013, doi: 10.3978/j.issn.2072-1439.2013.04.05.

[122] L. Silva, L. Garcia, B. Oliveira, M. Tanita, J. Festti, L. Cardoso, L. Lavado, and C. Grion, "Acute respiratory distress syndrome in burn patients: incidence and risk factor analysis.," *Ann. Burns Fire Disasters*, vol. 29, no. 3, pp. 178–182, Sep. 2016.

[123] S. M. Belenkiy, A. R. Buel, J. W. Cannon, C. R. Sine, J. K. Aden, J. L. Henderson, N. T. Liu, J. B. Lundy, E. M. Renz, A. I. Batchinsky, L. C. Cancio, and K. K. Chung, "Acute respiratory distress syndrome in wartime military burns," *J. Trauma Acute Care Surg.*, vol. 76, no. 3, pp. 821–827, Mar. 2014, doi: 10.1097/TA.0b013e3182aa2d21.

[124] M. S. Clemens, I. J. Stewart, J. A. Sosnov, J. T. Howard, S. M. Belenkiy, C. R. Sine, J. L. Henderson, A. R. Buel, A. I. Batchinsky, L. C. Cancio, and K. K. Chung, "Reciprocal Risk of Acute Kidney Injury and Acute Respiratory Distress Syndrome in Critically Ill Burn Patients.," *Crit. Care Med.*, vol. 44, no. 10, pp. e915-22, Oct. 2016, doi: 10.1097/CCM.0000000000001812.

[125] S. Belenkiy, K. M. Ivey, A. I. Batchinsky, T. Langer, C. Necsoiu, W. Baker, J. Salinas, and L. C. Cancio, "Noninvasive Carbon Dioxide Monitoring in a Porcine Model of Acute Lung Injury Due to Smoke Inhalation and Burns," *Shock*, vol. 39, no. 6, pp. 495–500, Jun. 2013, doi: 10.1097/SHK.0b013e318292c331.

[126] A. I. Batchinsky, S. E. Burkett, T. B. Zanders, K. K. Chung, D. D. Regn, B. S. Jordan, C. Necsoiu, R. Nguyen, M. A. Hanson, M. J. Morris, and L. C. Cancio, "Comparison of airway pressure release ventilation to conventional mechanical ventilation in the early management of smoke inhalation injury in swine," *Crit. Care Med.*, vol. 39, no. 10, pp. 2314–2321, Oct. 2011, doi: 10.1097/CCM.0b013e318225b5b3.

[127] C. R. Sine, S. M. Belenkiy, A. R. Buel, J. A. Waters, J. B. Lundy, J. L. Henderson, I. J. Stewart, J. K. Aden, N. T. Liu, A. Batchinsky, J. W. Cannon, L. C. Cancio, and K. K. Chung, "Acute Respiratory Distress Syndrome in Burn Patients: A Comparison of the Berlin and American-European Definitions," *J. Burn Care Res.*, vol. 37, no. 5, pp. e461–e469, Sep. 2016, doi: 10.1097/BCR.0000000000000348.

[128] R. Cartotto, Z. Li, S. Hanna, S. Spano, D. Wood, K. Chung, and F. Camacho, "The Acute Respiratory Distress Syndrome (ARDS) in mechanically ventilated burn patients: An analysis of risk factors, clinical

features, and outcomes using the Berlin ARDS definition," *Burns*, vol. 42, no. 7, pp. 1423–1432, Nov. 2016, doi: 10.1016/J.BURNS.2016.01.031.
[129] T. Bice, C. E. Cox, and S. S. Carson, "Cost and health care utilization in ARDS--different from other critical illness?," *Semin. Respir. Crit. Care Med.*, vol. 34, no. 4, pp. 529–36, Aug. 2013, doi: 10.1055/s-0033-1351125.
[130] R. Zhang, Z. Wang, P. Tejera, A. J. Frank, Y. Wei, L. Su, Z. Zhu, Y. Guo, F. Chen, E. K. Bajwa, B. T. Thompson, and D. C. Christiani, "Late-onset moderate to severe acute respiratory distress syndrome is associated with shorter survival and higher mortality: a two-stage association study.," *Intensive Care Med.*, vol. 43, no. 3, pp. 399–407, Mar. 2017, doi: 10.1007/s00134-016-4638-3.
[131] K. N. Kangelaris, L. B. Ware, C. Y. Wang, D. R. Janz, H. Zhuo, M. A. Matthay, and C. S. Calfee, "Timing of Intubation and Clinical Outcomes in Adults With Acute Respiratory Distress Syndrome.," *Crit. Care Med.*, vol. 44, no. 1, pp. 120–9, Jan. 2016, doi: 10.1097/CCM.0000000000001359.
[132] Y. Nakano, S. Muro, H. Sakai, T. Hirai, K. Chin, M. Tsukino, K. NISHIMURA, H. ITOH, P. D. PARÉ, J. C. HOGG, and M. MISHIMA, "Computed Tomographic Measurements of Airway Dimensions and Emphysema in Smokers," *Am. J. Respir. Crit. Care Med.*, vol. 162, no. 3, pp. 1102–1108, Sep. 2000, doi: 10.1164/ajrccm.162.3.9907120.
[133] P. Berger, V. Perot, P. Desbarats, J. M. Tunon-de-Lara, R. Marthan, and F. Laurent, "Airway Wall Thickness in Cigarette Smokers: Quantitative Thin-Section CT Assessment," *Radiology*, vol. 235, no. 3, pp. 1055–1064, Jun. 2005, doi: 10.1148/radiol.2353040121.
[134] M. Hasegawa, Y. Nasuhara, Y. Onodera, H. Makita, K. Nagai, S. Fuke, Y. Ito, T. Betsuyaku, and M. Nishimura, "Airflow Limitation and Airway Dimensions in Chronic Obstructive Pulmonary Disease," *Am. J. Respir. Crit. Care Med.*, vol. 173, no. 12, pp. 1309–1315, Jun. 2006, doi: 10.1164/rccm.200601-037OC.
[135] T. Ohara, T. Hirai, S. Sato, A. Sato, M. Nishiaki, S. Muro, and M. MISHIMA, "Comparison of airway dimensions in different anatomic locations on chest CT in patients with COPD," *Respirology*, vol. 11, no. 5, pp. 579–585, Sep. 2006, doi: 10.1111/j.1440-1843.2006.00899.x.
[136] E. Lin and A. Alessio, "What are the basic concepts of temporal, contrast, and spatial resolution in cardiac CT?," *J. Cardiovasc. Comput. Tomogr.*, vol. 3, no. 6, pp. 403–8, 2009, doi: 10.1016/j.jcct.2009.07.003.
[137] M. Brenner, K. Kreuter, J. Ju, S. Mahon, L. Tseng, and D. Mukai, "In vivo optical coherence tomography detection of differences in regional large airway smoke inhalation induced injury in a rabbit model," *J Biomed Opt*, vol. 13, no. 3, pp. 1–15, 2009, doi: 10.1117/1.2939400.In.
[138] J. Choi, C. Li-Dek, R. Teryn, B. Brendan, W. Daniel, E. Mark, S. Kyle, D. Alexander, J. Bryan, B. Matthew, C. Zhongping, N. Corna, C. Leopoldo, and B. Andriy, "Point-of-care endoscopic optical coherence tomography detects changes in mucosal thickness in ARDS due to smoke inhalation and burns," *Burns*, vol. 45, no. 3, pp. 589–597, 2018.
[139] Z. Wang, B. Potsaid, L. Chen, C. Doerr, H.-C. Lee, T. Nielson, V. Jayaraman, A. E. Cable, E. Swanson, and J. G. Fujimoto, "Cubic meter volume optical coherence tomography," *Optica*, vol. 3, no. 12, p. 1496, Dec. 2016, doi: 10.1364/OPTICA.3.001496.
[140] J. J. Armstrong, M. S. Leigh, I. D. Walton, A. V. Zvyagin, S. A. Alexandrov, S. Schwer, D. D. Sampson, D. R. Hillman, and P. R. Eastwood, "In vivo size and shape measurement of the human upper airway using endoscopic long-range optical coherence tomography," *Opt. Express*, vol. 11, no. 15, p. 1817, Jul. 2003, doi: 10.1364/OE.11.001817.
[141] K. Linden, V. Scaravilli, S. F. X. Kreyer, S. M. Belenkiy, I. J. Stewart, K. K. Chung, L. C. Cancio, and A. I. Batchinsky, "Evaluation of the Cytosorb™ Hemoadsorptive Column in a PIG Model of Severe Smoke and Burn Injury," *Shock*, vol. 44, no. 5, pp. 487–495, Nov. 2015, doi: 10.1097/SHK.0000000000000439.
[142] J. Yin, G. Liu, J. Zhang, L. Yu, S. Mahon, D. Mukai, M. Brenner, and Z. Chen, "In vivo early detection of smoke-induced airway injury using three-dimensional swept-source optical coherence tomography," *J. Biomed. Opt.*, vol. 14, no. 6, p. 060503, 2009, doi: 10.1117/1.3268775.
[143] R Core Team, "R: A language and environment for statistical computing. R Foundation for Statistical Computing." Vienna, Austria, 2018.
[144] R. J. Boots, J. M. Dulhunty, J. Paratz, and J. Lipman, "Respiratory Complications in Burns," *Clin. Pulm. Med.*, vol. 16, no. 3, pp. 132–138, May 2009, doi: 10.1097/CPM.0b013e3181a39032.
[145] A. Sarvazyan, T. J. Hall, M. W. Urban, M. Fatemi, S. R. Aglyamov, and B. S. Garra, "An overview of elasticity imaging - an emerging branch of medical imaging.," *Curr. Med. Imaging Rev.*, vol. 7, no. 4, pp. 255–282, Nov. 2011.
[146] K. P. Strohl, J. P. Butler, and A. Malhotra, "Mechanical properties of the upper airway," *Compr. Physiol.*, vol. 2, no. 3, pp. 1853–1872, Jul. 2012, doi: 10.1002/cphy.c110053.

[147] K. A. Domany, E. Dana, R. Tauman, G. Gut, M. Greenfeld, B. El Yakir, and Y. Sivan, "Adenoidectomy for obstructive sleep apnea in children," *J. Clin. Sleep Med.*, vol. 12, no. 9, pp. 1285–1291, 2016, doi: 10.5664/jcsm.6134.

[148] D. G. Ingram and N. R. Friedman, "Toward adenotonsillectomy in children a review for the general pediatrician," *JAMA Pediatrics*, vol. 169, no. 12. American Medical Association, pp. 1155–1161, Dec. 01, 2015, doi: 10.1001/jamapediatrics.2015.2016.

[149] S. L. Davidson, R. Amin, R. Arens, Z. Chen, S. Davis, E. Gutmark, R. Superfine, B. Wong, C. Zdanski, and M. C. K. Khoo, "Pediatric Sleep-Related Breathing Disorders: Advances in imaging and computational modeling HHS Public Access," *IEEE Pulse*, vol. 5, no. 5, pp. 33–39, 2014, doi: 10.1109/MPUL.2014.2339293.

[150] F. Lazarow, G. S. Ahuja, G. Sharma, A. Wang, E. Su, Z. Chen, and B. J. F. Wong, "First Use of Long-Range Optical Coherence Tomography to Image Airway Structure in Awake Children," *Otolaryngol. Neck Surg.*, vol. 151, no. 1_suppl, pp. P133–P133, Sep. 2014, doi: 10.1177/0194599814541627a325.

[151] J. Yin, G. Liu, J. Zhang, L. Yu, S. Mahon, D. Mukai, M. Brenner, and Z. Chen, "In vivo early detection of smoke-induced airway injury using three-dimensional swept-source optical coherence tomography," doi: 10.1117/1.3268775.

[152] R. Bu, S. Balakrishnan, N. Iftimia, H. Price, C. Zdanski, and A. L. Oldenburg, "Airway compliance measured by anatomic optical coherence tomography.," *Biomed. Opt. Express*, vol. 8, no. 4, pp. 2195–2209, Apr. 2017, doi: 10.1364/BOE.8.002195.

[153] R. Bu, S. Balakrishnan, H. Price, C. Zdanski, S. Mitran, and A. L. Oldenburg, "Localized compliance measurement of the airway wall using anatomic optical coherence elastography," *Opt. Express*, vol. 27, no. 12, p. 16751, 2019, doi: 10.1364/oe.27.016751.

[154] J. P. Williamson, R. A. McLaughlin, W. J. Noffsinger, A. L. James, V. A. Baker, A. Curatolo, J. J. Armstrong, A. Regli, K. L. Shepherd, G. B. Marks, D. D. Sampson, D. R. Hillman, and P. R. Eastwood, "Elastic properties of the central airways in obstructive lung diseases measured using anatomical optical coherence tomography," *Am. J. Respir. Crit. Care Med.*, vol. 183, no. 5, pp. 612–619, 2011, doi: 10.1164/rccm.201002-0178OC.

[155] G. J. Ughi, "Automatic three-dimensional registration of intravascular optical coherence tomography images," *J. Biomed. Opt.*, vol. 17, no. 2, p. 026005, Mar. 2012, doi: 10.1117/1.jbo.17.2.026005.

[156] O. O. Ahsen, H.-C. Lee, M. G. Giacomelli, Z. Wang, K. Liang, T.-H. Tsai, B. Potsaid, H. Mashimo, and J. G. Fujimoto, "Correction of rotational distortion for catheter-based en face OCT and OCT angiography," *Opt. Lett.*, vol. 39, no. 20, p. 5973, Oct. 2014, doi: 10.1364/ol.39.005973.

[157] E. Abouei, A. M. D. Lee, H. Pahlevaninezhad, G. Hohert, M. Cua, P. Lane, S. Lam, and C. MacAulay, "Correction of motion artifacts in endoscopic optical coherence tomography and autofluorescence images based on azimuthal en face image registration.," *J. Biomed. Opt.*, vol. 23, no. 1, pp. 1–13, 2018, doi: 10.1117/1.JBO.23.1.016004.

[158] G. van Soest, J. G. Bosch, and A. F. W. van der Steen, "Azimuthal registration of image sequences affected by nonuniform rotation distortion," *IEEE Trans. Inf. Technol. Biomed.*, vol. 12, no. 3, pp. 348–355, 2008, doi: 10.1109/TITB.2007.908000.

[159] N. Uribe-Patarroyo and B. E. Bouma, "Rotational distortion correction in endoscopic optical coherence tomography based on speckle decorrelation," *Opt. Lett.*, vol. 40, no. 23, p. 5518, Dec. 2015, doi: 10.1364/ol.40.005518.

[160] C. Sun, F. Nolte, K. H. Y. Cheng, B. Vuong, K. K. C. Lee, B. A. Standish, B. Courtney, T. R. Marotta, A. Mariampillai, and V. X. D. Yang, "In vivo feasibility of endovascular Doppler optical coherence tomography," *Biomed. Opt. Express*, vol. 3, no. 10, p. 2600, Oct. 2012, doi: 10.1364/boe.3.002600.

[161] M. A. Sleigh, "Ciliary function in transport of mucus.," *Eur. J. Respir. Dis. Suppl.*, vol. 128 (Pt 1), pp. 287–92, Jan. 1983.

[162] X. M. Bustamante-Marin and L. E. Ostrowski, "Cilia and mucociliary clearance," *Cold Spring Harb. Perspect. Biol.*, vol. 9, no. 4, Apr. 2017, doi: 10.1101/cshperspect.a028241.

[163] D. Huang, E. A. Swanson, C. P. Lin, J. S. Schuman, W. G. Stinson, W. Chang, M. R. Hee, T. Flotte, K. Gregory, C. A. Puliafito, and al. et, "Optical coherence tomography.," *Science*, vol. 254, no. 5035, pp. 1178–81, Nov. 1991, doi: 10.1126/SCIENCE.1957169.

[164] H. M. Leung, S. E. Birket, C. Hyun, T. N. Ford, D. Cui, G. M. Solomon, R.-J. Shei, A. T. Adewale, A. R. Lenzie, C. M. Fernandez-Petty, H. Zheng, J. H. Palermo, D.-Y. Cho, B. A. Woodworth, L. M. Yonker, B. P. Hurley, S. M. Rowe, and G. J. Tearney, "Intranasal micro-optical coherence tomography imaging for cystic fibrosis studies," 2019.

[165] K. K. Chu, C. Unglert, T. N. Ford, D. Cui, R. W. Carruth, K. Singh, L. Liu, S. E. Birket, G. M. Solomon, S. M. Rowe, and G. J. Tearney, "In vivo imaging of airway cilia and mucus clearance with micro-optical coherence tomography," *Biomed. Opt. Express*, vol. 7, no. 7, p. 2494, 2016, doi: 10.1364/BOE.7.002494.
[166] A. D. Workman and N. A. Cohen, "The effect of drugs and other compounds on the ciliary beat frequency of human respiratory epithelium," *Am. J. Rhinol. Allergy*, vol. 28, no. 6, pp. 454–464, Nov. 2014, doi: 10.2500/ajra.2014.28.4092.
[167] D. A. Gil, J. T. Sharick, S. Mancha, U. A. Gamm, and M. A. Choma, "Redox imaging and optical coherence tomography of the respiratory ciliated epithelium," *J. Biomed. Opt.*, vol. 24, no. 01, p. 1, 2019, doi: 10.1117/1.jbo.24.1.010501.
[168] Y. He, Y. Qu, J. C. Jing, and Z. Chen, "Characterization of oviduct ciliary beat frequency using real time phase resolved Doppler spectrally encoded interferometric microscopy," *Biomed. Opt. Express*, vol. 10, no. 11, p. 5650, Nov. 2019, doi: 10.1364/boe.10.005650.
[169] J. C. Jing, J. J. Chen, L. Chou, B. J. F. Wong, and Z. Chen, "Visualization and Detection of Ciliary Beating Pattern and Frequency in the Upper Airway using Phase Resolved Doppler Optical Coherence Tomography," *Sci. Rep.*, vol. 7, no. 1, p. 8522, Dec. 2017, doi: 10.1038/s41598-017-08968-x.
[170] Y. He, J. C. Jing, Y. Qu, B. J. Wong, and Z. Chen, "Spatial Mapping of Tracheal Ciliary Beat Frequency Using Real Time Phase-Resolved Doppler Spectrally Encoded Interferometric Microscopy," *ACS Photonics*, vol. 7, no. 1, pp. 128–134, Jan. 2020, doi: 10.1021/acsphotonics.9b01235.
[171] B. K. Huang, U. A. Gamm, V. Bhandari, M. K. Khokha, and M. A. Choma, "Three-dimensional, three-vector-component velocimetry of cilia-driven fluid flow using correlation-based approaches in optical coherence tomography," *Biomed. Opt. Express*, vol. 6, no. 9, p. 3515, Sep. 2015, doi: 10.1364/boe.6.003515.
[172] S. Jonas, D. Bhattacharya, M. K. Khokha, and M. A. Choma, "Microfluidic characterization of cilia-driven fluid flow using optical coherence tomography-based particle tracking velocimetry," *Biomed. Opt. Express*, vol. 2, no. 7, p. 2022, Jul. 2011, doi: 10.1364/boe.2.002022.
[173] A. L. Oldenburg, R. K. Chhetri, D. B. Hill, and B. Button, "Monitoring airway mucus flow and ciliary activity with optical coherence tomography," *Biomed. Opt. Express*, vol. 3, no. 9, p. 1978, Sep. 2012, doi: 10.1364/BOE.3.001978.
[174] S. Wang, J. C. Burton, R. R. Behringer, and I. V. Larina, "In vivo micro-scale tomography of ciliary behavior in the mammalian oviduct," *Sci. Rep.*, vol. 5, Aug. 2015, doi: 10.1038/srep13216.
[175] L. Liu, K. K. Chu, G. H. Houser, B. J. Diephuis, and Y. Li, "Method for Quantitative Study of Airway Functional Microanatomy Using Micro-Optical Coherence Tomography," *PLoS One*, vol. 8, no. 1, p. 54473, 2013, doi: 10.1371/journal.pone.0054473.
[176] L. Liu, K. K. Chu, G. H. Houser, B. J. Diephuis, Y. Li, E. J. Wilsterman, S. Shastry, G. Dierksen, S. E. Birket, M. Mazur, S. Byan-Parker, W. E. Grizzle, E. J. Sorscher, S. M. Rowe, and G. J. Tearney, "Method for Quantitative Study of Airway Functional Microanatomy Using Micro-Optical Coherence Tomography," *PLoS One*, vol. 8, no. 1, p. e54473, Jan. 2013, doi: 10.1371/journal.pone.0054473.
[177] G. J. Tearney, R. H. Webb, and B. E. Bouma, "Spectrally encoded confocal microscopy.," *Opt. Lett.*, vol. 23, no. 15, pp. 1152–4, Aug. 1998.
[178] G. Liu, A. J. Lin, B. J. Tromberg, and Z. Chen, "A comparison of Doppler optical coherence tomography methods," *Biomed. Opt. Express*, vol. 3, no. 10, p. 2669, Oct. 2012, doi: 10.1364/BOE.3.002669.
[179] S. Moon and Z. Chen, "Phase-stability optimization of swept-source optical coherence tomography.," *Biomed. Opt. Express*, vol. 9, no. 11, p. 5280, Nov. 2018, doi: 10.1364/BOE.9.005280.
[180] L. Feriani, M. Juenet, C. J. Fowler, N. Bruot, M. Chioccioli, S. M. Holland, C. E. Bryant, and P. Cicuta, "Assessing the Collective Dynamics of Motile Cilia in Cultures of Human Airway Cells by Multiscale DDM," *Biophys. J.*, vol. 113, no. 1, pp. 109–119, 2017, doi: 10.1016/j.bpj.2017.05.028.
[181] Y. Li, S. Moon, J. J. Chen, Z. Zhu, and Z. Chen, "Ultrahigh-sensitive optical coherence elastography," *Light Sci. Appl.*, vol. 9, no. 1, p. 58, Dec. 2020, doi: 10.1038/s41377-020-0297-9.
[182] H. M. Leung, S. E. Birket, C. Hyun, T. N. Ford, D. Cui, G. M. Solomon, R. J. Shei, A. T. Adewale, A. R. Lenzie, C. M. Fernandez-Petty, H. Zheng, J. H. Palermo, D. Y. Cho, B. A. Woodworth, L. M. Yonker, B. P. Hurley, S. M. Rowe, and G. J. Tearney, "Intranasal micro-optical coherence tomography imaging for cystic fibrosis studies," *Sci. Transl. Med.*, vol. 11, no. 504, Aug. 2019, doi: 10.1126/scitranslmed.aav3505.
[183] S. Moon, Y. Miao, and Z. Chen, "Fiber-based polarization-sensitive optical coherence tomography of a minimalistic system configuration," *Opt. Lett.*, vol. 44, no. 12, p. 3150, Jun. 2019, doi: 10.1364/ol.44.003150.
[184] J. F. de Boer, S. M. Srinivas, A. Malekafzali, Z. Chen, and J. Stuart Nelson, "Imaging thermally damaged

tissue by polarization sensitive optical coherence tomography," *Opt. Express*, vol. 3, no. 6, p. 212, 1998.
[185] J. F. de Boer, S. M. Srinivas, B. H. Park, T. H. Pham, Zhongping Chen, T. E. Milner, and J. S. Nelson, "Polarization effects in optical coherence tomography of various biological tissues," *IEEE J. Sel. Top. Quantum Electron.*, vol. 5, no. 4, p. 1200, 1999, doi: 10.1109/2944.796347.
[186] J. F. de Boer, T. E. Milner, M. J. van Gemert, and J. S. Nelson, "Two-dimensional birefringence imaging in biological tissue by polarization-sensitive optical coherence tomography.," *Opt. Lett.*, vol. 22, no. 12, p. 934, Jun. 1997.
[187] J. F. de Boer, C. K. Hitzenberger, and Y. Yasuno, "Polarization sensitive optical coherence tomography – a review [Invited]," *Biomed. Opt. Express*, vol. 8, no. 3, p. 1838, Mar. 2017, doi: 10.1364/BOE.8.001838.
[188] M. R. Hee, E. A. Swanson, J. G. Fujimoto, and D. Huang, "Polarization-sensitive low-coherence reflectometer for birefringence characterization and ranging," *J. Opt. Soc. Am. B*, vol. 9, no. 6, p. 903, Jun. 1992, doi: 10.1364/JOSAB.9.000903.
[189] S. Guo, J. Zhang, L. Wang, J. S. Nelson, and Z. Chen, "Depth-resolved birefringence and differential optical axis orientation measurements with fiber-based polarization-sensitive optical coherence tomography," *Opt. Lett.*, vol. 29, no. 17, p. 2025, Sep. 2004, doi: 10.1364/ol.29.002025.
[190] C. E. Saxer, J. F. De Boer, B. H. Park, Y. Zhao, Z. Chen, and J. S. Nelson, "High-speed fiber-based polarization-sensitive optical coherence tomography of in vivo human skin," *Opt. Lett.*, vol. 25, no. 18, p. 1355, 2000.
[191] B. Baumann, W. Choi, B. Potsaid, D. Huang, J. S. Duker, and J. G. Fujimoto, "Swept source/Fourier domain polarization sensitive optical coherence tomography with a passive polarization delay unit.," *Opt. Express*, vol. 20, no. 9, p. 10218, Apr. 2012, doi: 10.1364/OE.20.010229.
[192] M. J. Ju, Y.-J. Hong, S. Makita, Y. Lim, K. Kurokawa, L. Duan, M. Miura, S. Tang, and Y. Yasuno, "Advanced multi-contrast Jones matrix optical coherence tomography for Doppler and polarization sensitive imaging," *Opt. Express*, vol. 21, no. 16, p. 19412, Aug. 2013, doi: 10.1364/OE.21.019412.
[193] B. Baumann, E. Götzinger, M. Pircher, and C. K. Hitzenberger, "Single camera based spectral domain polarization sensitive optical coherence tomography," *Opt. Express*, vol. 15, no. 3, p. 1054, Feb. 2007, doi: 10.1364/OE.15.001054.
[194] B. Cense, M. Mujat, T. C. Chen, B. H. Park, and J. F. de Boer, "Polarization-sensitive spectral-domain optical coherence tomography using a single line scan camera," *Opt. Express*, vol. 15, no. 5, p. 2421, Mar. 2007, doi: 10.1364/oe.15.002421.
[195] H. Wang, M. K. Al-Qaisi, and T. Akkin, "Polarization-maintaining fiber based polarization-sensitive optical coherence tomography in spectral domain," *Opt. Lett.*, vol. 35, no. 2, p. 154, Jan. 2010, doi: 10.1364/OL.35.000154.
[196] S. Rivet, M. J. Marques, A. Bradu, and A. Podoleanu, "Passive optical module for polarization-sensitive optical coherence tomography systems," *Opt. Express*, vol. 25, no. 13, p. 14533, 2017, doi: 10.1364/OE.25.014533.
[197] S. Moon, Y. Qu, and Z. Chen, "Characterization of spectral-domain OCT with autocorrelation interference response for axial resolution performance," *Opt. Express*, vol. 26, no. 6, p. 7253, Mar. 2018, doi: 10.1364/OE.26.007253.
[198] Y. Tadir, A. Gaspar, A. Lev-Sagie, M. Alexiades, R. Alinsod, A. Bader, A. Calligaro, J. A. Elias, M. Gambaciani, J. E. Gaviria, C. B. Iglesia, K. Selih-Martinec, P. L. Mwesigwa, U. B. Ogrinc, S. Salvatore, P. Scollo, N. Zerbinati, and J. S. Nelson, "Light and energy based therapeutics for genitourinary syndrome of menopause: Consensus and controversies," *Lasers Surg. Med.*, vol. 49, no. 2, pp. 137–159, 2017, doi: 10.1002/lsm.22637.
[199] N. Santoro and J. Komi, "Prevalence and Impact of Vaginal Symptoms among Postmenopausal Women," *J. Sex. Med.*, vol. 6, no. 8, pp. 2133–2142, Aug. 2009, doi: 10.1111/j.1743-6109.2009.01335.x.
[200] H.-K. Kim, S.-Y. Kang, Y.-J. Chung, J.-H. Kim, and M.-R. Kim, "The Recent Review of the Genitourinary Syndrome of Menopause.," *J. menopausal Med.*, vol. 21, no. 2, pp. 65–71, Aug. 2015, doi: 10.6118/jmm.2015.21.2.65.
[201] M. B. Mac Bride, D. J. Rhodes, and L. T. Shuster, "Vulvovaginal atrophy," *Mayo Clinic Proceedings*, vol. 85, no. 1. Elsevier Ltd, pp. 87–94, 2010, doi: 10.4065/mcp.2009.0413.
[202] D. J. Portman *et al.*, "Genitourinary Syndrome of Menopause: New Terminology for Vulvovaginal Atrophy from the International Society for the Study of Women's Sexual Health and the North American Menopause Society," *Menopause*, vol. 21, no. 10, pp. 1063–1068, 2014, doi: 10.1097/gme.0000000000000329.
[203] R. E. Nappi and S. Palacios, "Impact of vulvovaginal atrophy on sexual health and quality of life at postmenopause," *Climacteric*, vol. 17, no. 1. pp. 3–9, Feb. 2014, doi: 10.3109/13697137.2013.871696.

[204] E. R. Sokol and M. M. Karram, “Use of a novel fractional CO2 laser for the treatment of genitourinary syndrome of menopause,” *Menopause*, vol. 24, no. 7, pp. 810–814, Jul. 2017, doi: 10.1097/GME.0000000000000839.
[205] M. S. Lee, “Treatment of vaginal relaxation syndrome with an erbium: YAG laser using 90° and 360° scanning scopes: A pilot study & short-term results,” in *Laser Therapy*, 2014, vol. 23, no. 2, pp. 129–138, doi: 10.5978/islsm.14-OR-11.
[206] P. A., C. A., F. F., T. C., C. C. G., S. A., S. S., C. C. G., A. Perino, A. Calligaro, F. Forlani, C. Tiberio, G. Cucinella, A. Svelato, S. Saitta, and G. Calagna, “Vulvo-vaginal atrophy: A new treatment modality using thermo-ablative fractional CO2 laser,” *Maturitas*, vol. 80, no. 3, pp. 296–301, 2015, doi: 10.1016/j.maturitas.2014.12.006 LK - http://rd8hp6du2b.search.serialssolutions.com?sid=EMBASE&issn=18734111&id=doi:10.1016%2Fj.maturitas.2014.12.006&atitle=Vulvo-vaginal+atrophy%3A+A+new+treatment+modality+using+thermo-ablative+fractional+CO2+laser&stitle=Maturitas&title=Maturitas&volume=80&issue=3&spage=296&epage=301&aulast=Perino&aufirst=Antonino&auinit=A.&aufull=Perino+A.&coden=MATUD&isbn=&pages=296-301&date=2015&auinit1=A&auinitm=.
[207] D. Huang, E. A. Swanson, C. P. Lin, J. S. Schuman, W. G. Stinson, W. Chang, M. R. Hee, T. Flotte, K. Gregory, C. A. Puliafito, and J. G. Fujimoto, “Optical coherence tomography,” *Science (80-.).*, vol. 254, no. 5035, pp. 1178–1181, 1991, doi: 10.1126/science.1957169.
[208] A. Balica, D. Wald-Spielman, K. Schertz, S. Egan, and G. Bachmann, “Assessing the thickness of the vaginal wall and vaginal mucosa in pre-menopausal versus post-menopausal women by transabdominal ultrasound: A feasibility study,” *Maturitas*, vol. 102, pp. 69–72, Aug. 2017, doi: 10.1016/J.MATURITAS.2017.02.017.
[209] K. L. Vincent, G. Vargas, J. Wei, N. Bourne, and M. Motamedi, “Monitoring vaginal epithelial thickness changes noninvasively in sheep using optical coherence tomography,” *Am. J. Obstet. Gynecol.*, vol. 208, no. 4, pp. 282.e1-282.e7, Apr. 2013, doi: 10.1016/j.ajog.2013.01.025.
[210] K. L. Vincent, L. R. Stanberry, T. R. Moench, C. R. Breitkopf, M. L. Loza, J. Wei, J. Grady, J. Paull, M. Motamedi, and S. L. Rosenthal, “Optical Coherence Tomography Compared With Colposcopy for Assessment of Vaginal Epithelial Damage,” *Obstet. Gynecol.*, vol. 118, no. 6, pp. 1354–1361, Dec. 2011, doi: 10.1097/AOG.0b013e318238f563.
[211] Y. Li, N. T. Sudol, Y. Miao, J. C. Jing, J. Zhu, F. Lane, and Z. Chen, “1.7 Micron Optical Coherence Tomography for Vaginal Tissue Characterization in vivo,” *Lasers Surg. Med.*, vol. 51, no. 2, pp. 120–126, Feb. 2019, doi: 10.1002/lsm.23003.
[212] G. A. Lapii, A. Y. Yakovleva, A. I. Neimark, and E. L. Lushnikova, “Study of Proliferative Activity of Vaginal Epithelium in Women with Stress Urinary Incontinence Treated by Er:YAG Laser,” *Bull. Exp. Biol. Med.*, vol. 163, no. 2, pp. 280–283, Jun. 2017, doi: 10.1007/s10517-017-3784-0.
[213] S. Salvatore, R. E. Nappi, N. Zerbinati, A. Calligaro, S. Ferrero, M. Origoni, M. Candiani, and U. Leone Roberti Maggiore, “A 12-week treatment with fractional CO_2 laser for vulvovaginal atrophy: a pilot study,” *Climacteric*, vol. 17, no. 4, pp. 363–369, Aug. 2014, doi: 10.3109/13697137.2014.899347.
[214] T. W. Sadler, *Langman’s Medical Embryology*, IX. Baltimore:Lippincott Williams&Wilkins, 2000.
[215] G. R. Cunha, “The dual origin of vaginal epithelium,” *Am. J. Anat.*, vol. 143, no. 3, pp. 387–392, Jul. 1975, doi: 10.1002/aja.1001430309.
[216] J. N. S. D’Hooghe, A. W. M. Goorsenberg, D. M. De Bruin, J. J. T. H. Roelofs, J. T. Annema, and P. I. Bonta, “Optical coherence tomography for identification and quantification of human airway wall layers,” *PLoS One*, vol. 12, no. 10, Oct. 2017, doi: 10.1371/journal.pone.0184145.
[217] I. Goldstein and J. L. Alexander, “Practical Aspects in the Management of Vaginal Atrophy and Sexual Dysfunction in Perimenopausal and Postmenopausal Women,” *J. Sex. Med.*, vol. 2, pp. 154–165, Sep. 2005, doi: 10.1111/j.1743-6109.2005.00131.x.
[218] Z. Chen, Y. Zhao, J. F. de Boer, and J. S. Nelson, “High speed high resolution phase resolved OCT/ODT,” in *Technical Digest. Summaries of papers presented at the Conference on Lasers and Electro-Optics. Postconference Edition. CLEO ’99. Conference on Lasers and Electro-Optics (IEEE Cat. No.99CH37013)*, p. 253, doi: 10.1109/CLEO.1999.834150.
[219] Y. Zhao, K. M. Brecke, H. Ren, Z. Ding, J. S. Nelson, and Z. Chen, “Three-dimensional reconstruction of in vivo blood vessels in human skin using phase-resolved optical Doppler tomography,” *IEEE J. Sel. Top. Quantum Electron.*, vol. 7, no. 6, pp. 931–935, 2001, doi: 10.1109/2944.983296.
[220] M. J. Ju, M. Heisler, A. Athwal, M. V Sarunic, and Y. Jian, “Effective bidirectional scanning pattern for optical coherence tomography angiography.,” *Biomed. Opt. Express*, vol. 9, no. 5, pp. 2336–2350, May

2018, doi: 10.1364/BOE.9.002336.
[221] J. Zhu, Y. Qu, T. Ma, R. Li, Y. Du, S. Huang, K. Kirk Shung, Q. Zhou, and Z. Chen, “Imaging and characterizing shear wave and shear modulus under orthogonal acoustic radiation force excitation using OCT Doppler variance method,” *Opt. Lett.*, vol. 40, no. 9, p. 2099, May 2015, doi: 10.1364/OL.40.002099.
[222] Y. He, Y. Qu, J. Zhu, Y. Zhang, A. Saidi, T. Ma, Q. Zhou, and Z. Chen, “Confocal Shear Wave Acoustic Radiation Force Optical Coherence Elastography for Imaging and Quantification of the In Vivo Posterior Eye,” *IEEE J. Sel. Top. Quantum Electron.*, vol. 25, no. 1, pp. 1–7, Jan. 2019, doi: 10.1109/JSTQE.2018.2834435.
[223] Y. Qu, Y. He, A. Saidi, Y. Xin, Y. Zhou, J. Zhu, T. Ma, R. H. Silverman, D. S. Minckler, Q. Zhou, and Z. Chen, “In Vivo Elasticity Mapping of Posterior Ocular Layers Using Acoustic Radiation Force Optical Coherence Elastography,” *Investig. Opthalmology Vis. Sci.*, vol. 59, no. 1, p. 455, Jan. 2018, doi: 10.1167/iovs.17-22971.
[224] J. Zhu, Y. Miao, L. Qi, Y. Qu, Y. He, Q. Yang, and Z. Chen, “Longitudinal shear wave imaging for elasticity mapping using optical coherence elastography,” *Appl. Phys. Lett.*, vol. 110, no. 20, p. 201101, May 2017, doi: 10.1063/1.4983292.
[225] J. Zhu, Y. Qu, T. Ma, R. Li, Y. Du, and S. Huang, “Imaging and characterizing shear wave and shear modulus under orthogonal acoustic radiation force excitation using OCT Doppler variance method,” vol. 40, no. 9, pp. 2099–2102, 2015.
[226] A. Nahas, M. Tanter, T.-M. Nguyen, J.-M. Chassot, M. Fink, and A. Claude Boccara, “From supersonic shear wave imaging to full-field optical coherence shear wave elastography,” *J. Biomed. Opt.*, vol. 18, no. 12, p. 121514, Dec. 2013, doi: 10.1117/1.JBO.18.12.121514.